Imaging Pressure, Cells and Light Fields

Citation	Orth, Antony G. 2014. Imaging Pressure, Cells and Light Fields. Doctoral dissertation, Harvard University.
Accessed	April 17, 2018 5:02:59 PM EDT
Citable Link	http://nrs.harvard.edu/urn-3:HUL.InstRepos:12274584
Terms of Use	This article was downloaded from Harvard University's DASH repository, and is made available under the terms and conditions applicable to Other Posted Material, as set forth at http://nrs.harvard.edu/urn-3:HUL.InstRepos:dash.current.terms-of-use#LAA

Imaging Pressure, Cells and Light Fields

A dissertation presented
by

Antony G. Orth

to
The School of Engineering and Applied Sciences
in partial fulfillment of the requirements
for the degree of
Doctor of Philosophy
in the subject of

Applied Physics

Harvard University
Cambridge, Massachusetts
April 2014

Dissertation Advisor: Kenneth B. Crozier Author: Antony G. Orth

Imaging Pressure, Cells and Light Fields

Abstract

Imaging systems often make use of macroscopic lenses to manipulate light. Modern microfabrication techniques, however, have opened up a pathway to the development of novel arrayed imaging systems. In such systems, centimeter-scale areas can contain thousands to millions of micro-scale optical elements, presenting exciting opportunities for new imaging applications. We show two such applications in this thesis: pressure sensing in microfluidics and high throughput fluorescence microscopy for high content screening. Conversely, we show that arrayed elements are not always needed for three dimensional light field imaging.

This thesis is primarily concerned with three research topics. We demonstrate the monitoring of pressure, spatially resolved over two dimensions, using optical elements fully integrated with a microfluidic chip. Next, we develop a novel microscope that employs a microlens array to boost pixel throughput so that it exceeds the capabilities of the commercial automated fluorescence microscopes that are state-of-the-art at the time of writing. Finally, we investigate whether it is possible to reproduce the key capabilities of an arrayed imaging system known as a light field imager using conventional cameras and microscopes that have a single aperture and no microlens array. To this end, we developed a novel imaging technique that we call “light field moment imaging”. We show that light field moment imaging is capable of producing perspective views of a three dimensional scene by analysis of two images obtained at slightly different focus positions with a conventional camera or microscope.

Acknowledgements

My years as a graduate student in the School of Engineering and Applied Sciences (SEAS) at Harvard have been extremely rewarding. I have learned about many subjects that I had not even been aware of prior to embarking on my PhD studies. Moreover, SEAS is permeated with an incredibly positive culture that no doubt contributes to the success of all its research members, from undergraduates to faculty members.

First I would like to thank my advisor, Prof. Crozier, for his mentorship since I arrived at Harvard. Prof. Crozier's wealth of knowledge in photonics has been an invaluable resource for myself and for all group members. His lab management style exemplifies the positive culture of SEAS, making it easy for students and researchers to focus on work with the understanding that challenges will be met with enthusiasm and not criticism. As an incoming graduate student it is a daunting task to find an advisor who's research group will resonate both personally and academically. After over 5 years in Prof. Crozier's group I can confidently say that I chose the correct path during my time at Harvard.

I would like to thank my dissertation committee members, Prof. Jeff Lichtman and Prof. Todd Zickler for being enthusiastic supporters of my work in Prof. Crozier's group. Their input and advice throughout my time here has been indispensible. I feel truly privileged to have been able to interact and learn from a pair of true leaders in their respective fields. The time they have both taken to discuss my research results and suggest new avenues is deeply appreciated.

I've had countless interactions with Crozier group members that have contributed immensely to my graduate education. I'm grateful for all of the knowledge I've picked up from every group member since 2009. In particular, I am thankful for the guidance I received from Dr. Ethan

Schonbrun during my first couple of years in the group. Not only did his research provide the basis for much of the work in this dissertation, but he also taught me the basics of experimenting with and building optical systems. This is an oft-overlooked hands-on skill that cannot be learned from a book. One needs a patient mentor, and I was lucky to have one in the group.

I would also like to thank the Office of Technology Development for giving me important exposure to the process of translating academic achievements into industry. In addition, the SEAS Student Affairs Office does an incredible job of *helping* students navigate red tape (an impressively small amount at that). At other institutions, a student affairs office might actually make a student's life more difficult; this is yet another example of how SEAS's culture is really aimed at creating a positive student experience.

Finally I'd like to thank my family for all their support throughout my years "out east". Most importantly I'm thankful to my dad (Robert Orth, PhD.) who always listens to my latest research results with enthusiasm. More often than not he will also provide fantastic advice on how to tackle research problems, over the phone, without knowing the field. I think I know more optics than him now but I have a lot of math to learn to fully catch up with him. Lastly, a big thank you to (Dr.) Elspeth McGregor for always being supportive in all conceivable ways, especially for talking to me every day even though she was many, many time zones away.

Contents

1 Introduction

The overarching theme of the work in this thesis is optical imaging. Three main projects are presented in chronological order, each in their own chapter. The first project concerns the development of a micro-optical pressure sensor for in-vitro microfluidic models of oil well rock [1], [2]. Such sensors enable the imaging of pressure in microfluidic chips that emulate the microstructure of an oil well. During this project, exposure to microlens fabrication methods and high throughput fluorescence detection research in the Crozier group [3] sparked a high throughput fluorescence imaging project [4]–[6]. This line of work introduces a novel imaging architecture for high content screening in which a microlens array replaces the microscope objective used in automated microscopes. As we discuss in this thesis, this approach enables the imaging of large areas of fluorescent samples at throughputs that are significantly higher than those of the commercial widefield microscopes that are state-of-the-art at the time of writing. During the development of the microlens array microscope, we realized that it shared some interesting properties with light field cameras. Specifically, one could process the microscope data in such a way that the sample could be viewed from different viewpoints, yielding an impression of the depth of the sample. This newfound awareness of the light field literature precipitated a third research topic that we termed “light field moment imaging” [7], [8]. Systems known as light field cameras capture three-dimensional information, meaning that the perspective can be shifted, even after the image has been collected. These systems are more complicated, however, than conventional camera. We demonstrated that the perspective shifting properties of light field cameras can be achieved with traditional digital cameras.

Before delving into the details of each project, an introductory chapter is included to provide background on the novel research herein. Fluorescence microscopy, high content screening, light field imaging and microlens arrays are the major topics addressed in the introduction.

Each project chapter contains in depth information about each research thrust, a majority of which has been published in peer reviewed journals and conference proceedings [1], [2], [4]–[9]. At the end of each chapter, conclusions are drawn and future research directions are suggested.

1.1 Fluorescence Microscopy

The human eye cannot resolve microscopic structures; we require the aid of a microscope to do so. The general goal of a microscope is to magnify small structures so that they are visible (either directly or indirectly) to the human eye. A magnified image can either be relayed directly to the eye, or stored via some type of archiving process – such as photographic film or digital image storage. Many modern microscopes capture data with a digital image sensor, allowing the image to be recalled, studied and manipulated with ease after its acquisition.

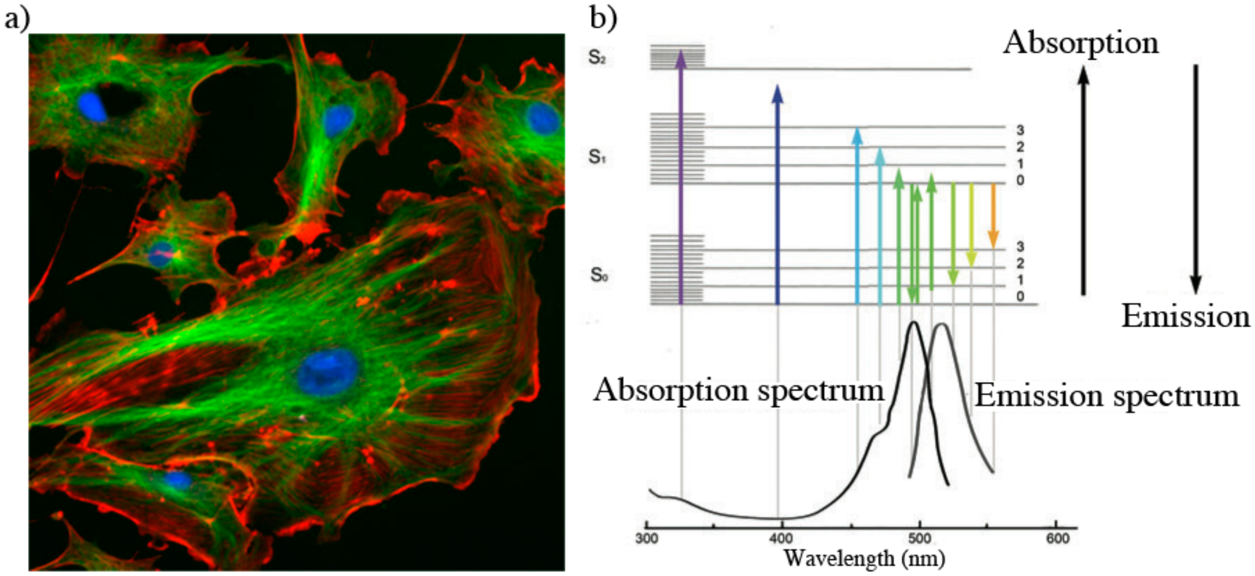

Figure 1-1 a) Fluorescence micrograph of fluorescently stained endothelial cells, reproduced from [10]. Blue: 4',6-diamidino-2-phenylindole (DAPI, indicates the nuclei); Green: fluorescein isothiocyanate (FITC, labels microtubules); Red: Tetramethylrhodamine (TRITC, labels actin). b) Jablonski diagram for FITC. The up (down) arrows correspond to photon absorption (emission). The arrow color and x-position indicate the wavelength of the emitted photon. S_0, S_1, S_2 are electron singlet states in ascending energy. The “0”, “1”, “2” and “3” labels on the right denote the vibrational levels of the molecule. The horizontal lines between vibrational levels are rotational energy levels. Diagram adapted with permission from Macmillan Publishers Ltd [11].

Microscopes come in a variety of forms, each best suited for a specific task. In this work we are concerned with fluorescence microscopy, which is typically used for quantitative biological experiments. Fluorescence microscopy is quantitative in the sense that the signal at each point in the image is proportional to the number of light-producing molecules (fluorophores or fluorescent proteins) at the corresponding location on the sample. Fluorophores can be bound to certain proteins or biomolecules with high specificity, so that the fluorescent light emission correlates precisely to the amount of a given protein or biomolecule of interest. A typical fluorescence micrograph is shown in Figure 1-1a, where three fluorescent stains each highlight different structures of endothelial cells. This is extremely useful in drug discovery applications where the quantification of the response of a cell to a candidate drug compound is of interest.

A fluorescent microscope broadly consists of an excitation light source, spectral filters and magnifying optics. While the magnifying optics are much the same as those of other types of microscopes, the excitation light source and spectral filters are unique to fluorescence microscopy. The excitation light source supplies photons, some of which are absorbed by the fluorophores [11]. This process is shown schematically in a Jablonski diagram in Figure 1-1b. The absorption of photon energy causes an electron to jump to a higher energy level. After a finite period of time, the excited electron relaxes back to its original state. During this process, however, the electron is subject to non-radiative transitions that diminish its energy, but by an amount that is small compared to its initial energy jump. The electron may also transition into a long lived triplet state where it can interact with its environment and possibly assist in a chemical reaction that prevents further fluorescence (photobleaching) [11]. When the electron does make its spontaneous optical transition back to the ground state, the energy released is in the form of a photon with energy that is smaller than that of the original excitation photon. Moreover, the electron might not relax directly to its original state, but instead to a slightly more energetic vibrational energy state. The relaxation process happens on a time scale of nanoseconds (for triplet state relaxation this can be on the order of microseconds). The difference in wavelength between the excitation and emitted photons is called the Stokes shift. The magnitude of the Stokes shift can vary, leading to a spread in the wavelength of the emitted photons. The bandwidth of the fluorescent photons is typically on the order of tens of nm. Because the excitation and emission photons are spectrally separated due to the Stokes shift, they can be separated by various spectral filters (see Figure 1-2). For example, a long pass filter can be placed in front of a detector to reject excitation lower wavelength excitation photons. The microscope is configured to only detect fluorescent photons, leading to remarkable contrast between signal and background.

In this thesis, we develop a novel fluorescence microscope that can be regarded in a qualitative fashion as being somewhere in between the two main types of fluorescence microscopes: widefield and confocal fluorescence microscopes. In this sub-section we present a brief overview of these two fluorescent imaging modalities.

1.1.1 Widefield Fluorescence Microscopy

A widefield fluorescence microscope is a system that images a continuous field-of-view (FOV) onto a two-dimensional detector. The most typical approach is termed an epifluorescent configuration and is shown in Figure 1-2. Excitation photons are collected from the source using condensing optics and are directed into the microscope objective. The excitation source may be broadband (Xenon arc lamp), narrowband (light emitting diode (LED)) or monochromatic (laser). If the excitation source has an appreciable bandwidth, an excitation filter may be used to ensure efficient separation from longer wavelength fluorescence. The fluorescence emitted by the sample, in response to the excitation photons, is collected by the microscope objective. Microscope lenses are often termed “infinity conjugate” objectives, meaning that they are designed to be used with the sample located at their front focal plane. The image created by the microscope objective is therefore created at infinity. A tube lens is inserted behind the microscope objective in order to create an image at the image sensor. The tube lens will typically have a focal length of 200 mm and be placed one focal length from the image sensor.

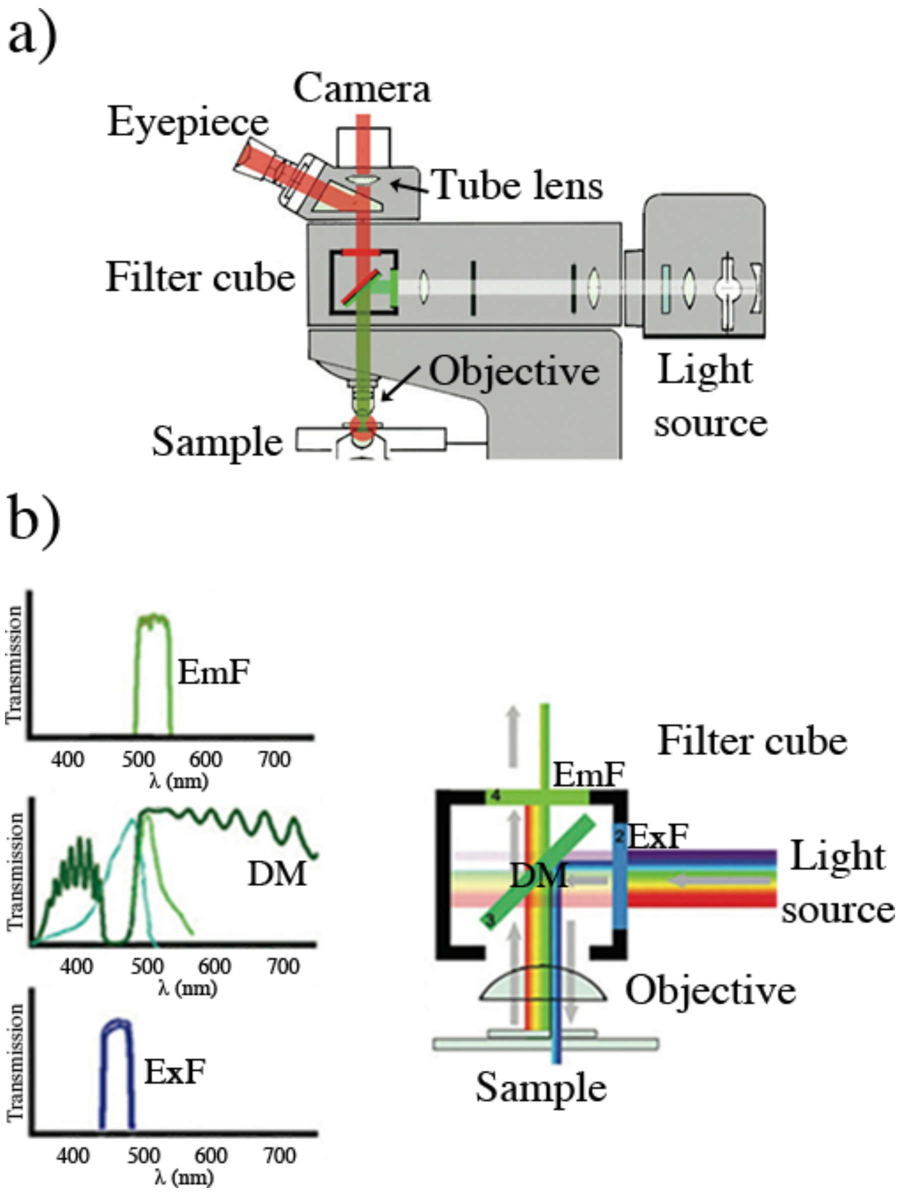

Figure 1-2 a) Light path in an epifluorescent widefield fluorescence microscope. b) Detailed view of beamsplitter cube, containing emission filter (EmF), dichroic mirror (DM) and excitation filter (ExF). The transmission spectra of these elements are shown in the insets. The dichroic mirror transmission spectrum is overlaid on top of the excitation (blue) and emission (light green) spectra for green fluorescent protein (GFP). Figure adapted with permission from Macmillan Publishers Ltd [11].

The excitation and detection light paths overlap in an epifluorescent configuration for the section from the dichroic mirror to the objective lens. A long pass dichroic mirror reflects excitation photons into the microscope objective. Because the fluorescently emitted photons have longer wavelengths than the excitation photons, the two are separated at the dichroic mirror. Scattered excitation photons are reflected back to the source, while the fluorescently emitted photons pass through the dichroic towards the tube lens and image sensor. Often, an additional filter (long pass or band pass) is placed in front of the image sensor in order to reject any excitation photons that have nonetheless passed through the dichroic. The image sensor captures photons over a finite integration time. The integration time that is needed depends on the rate at which emitted photons are recorded, which in turn is proportional to the excitation intensity. Typical integration times for widefield microscopy are $\approx 1-500$ ms.

One may choose to image a sample containing different types of fluorophores. Ideally, the emission spectra (and/or excitation spectra) of these fluorophores are spectrally isolated from one another. Each type of fluorophore can therefore be imaged independently either by appropriate choice of emission filter or excitation wavelength. If judicious use of emission bandpass filters or excitation wavelength is insufficient for the task of isolating the fluorescent signals, spectral unmixing algorithms can be used.

One inherent limitation to widefield microscopes is their inability to reject out-of-focus light. Fluorescent photons originating from the focal plane will focused to a sharp image at the image sensor. However, photons originating from other planes will also arrive at the image sensor, albeit as a blurred background signal. Special optical sectioning techniques are needed to reject out of focus light. The most common optical sectioning method is confocal microscopy.

1.1.2 Confocal Fluorescence Microscopy

A confocal microscope can produce images where the signal is chiefly from the focal plane. Confocal microscopes achieve this through use of a scanning beam configuration, rather than the widefield geometry discussed in the previous section.

Instead of illuminating an entire field-of-view (FOV) at once, a confocal microscope images a source located at optical infinity down to a focal spot at the sample plane. The fluorophores located within the focal spot are excited and emit fluorescence, which is collected by the microscope as depicted in Figure 1-3a. As in the widefield microscope, the objective and tube lens create an image of the sample. In a confocal microscope, however, a pinhole (rather than an image sensor) is placed at the image plane [12]. An image of the sample is indeed created at the pinhole plane, however, only the portion of the sample excited by the focal spot is emitting photons. The result is an image of the focal spot, the brightness of which is modulated by the fluorophore density within the focal spot. A single element detector such as an avalanche photodiode or photomultiplier tube is placed behind the pinhole, collecting all of the photons that have passed through the pinhole.

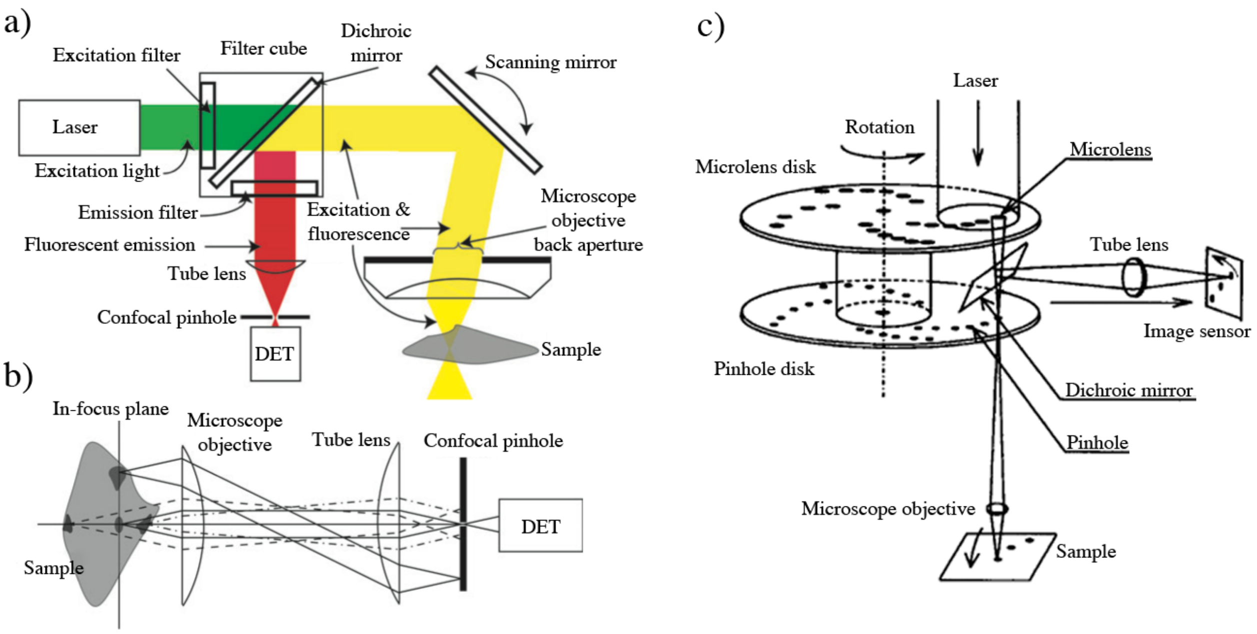

Figure 1-3 a) Laser scanning confocal microscope. A scanning mirror deflects the laser beam at a small angle with respect to the optical axis, resulting in a shift of the focal spot on the sample. Fluorescent emission is collected onto a single element detector (DET) such as a photomultiplier tube or an avalanche photodiode. b) Light originating from above or below the in-focus plane (dashed lines) is mostly blocked by the confocal pinhole. Fluorescence originating from the excitation spot of the in-focus plane is focused through the pinhole and reaches the detector (DET). c) Schematic of a Yokogawa spinning disk confocal microscope. An array of focal spots is created by the combination of a microlens disk and pinhole disk, and is imaged onto the sample with a microscope objective. The spots are scanned by spinning the disk. The fluorescence is imaged back through the pinhole disk and onto an image sensor. A full image is created each time that a spiral arm of the disk creates passes over the FOV. (a) & (b) are adapted with permission from Macmillan Publishers Ltd [13], (c) is reproduced from [12] with permission from Springer Science and Business Media.

The confocal microscope achieves optical sectioning through the use of point excitation and point detection. Point excitation refers to the fact that the excitation light is focused to a spot at the front focal plane of the microscope objective. Point detection refers to the use of an aperture at the image plane to reject photons originating from planes above or below the front focal plane. Only the fluorescent signal originating within a thin region above and below the focal plane is collected by the detector. In addition to optical sectioning, the in-plane resolution of a confocal microscope improves upon that of the widefield microscope due to the presence of the pinhole [14].

A confocal microscope creates a two-dimensional image by scanning the excitation spot over the sample. This can be realized in a number of ways, for example by moving the sample or by changing the angle at which the excitation beam enters the microscope objective aperture. The latter is the common method and is typically implemented by a pair of galvanometer mirrors. These scanning mirrors are often placed in between the dichroic mirror and the microscope objective so that the collected fluorescence can be "de-scanned". This means even though the focal spot is raster scanned over the sample, the image of the fluorescence from the focal spot is always centered on the pinhole aperture. A spinning disk confocal microscope system uses a different method for scanning the excitation spot. It patterns illumination into a grid of focal spots using paired microlens and pinhole arrays; the focal spots are scanned over the sample by rotating the disks on which these arrays are formed [13], [15]. Each sweep of the focal spot array illuminates the entirety of the microscope FOV that is imaged by a camera. This technique is capable of imaging speeds that exceed video rate.

In contrast to widefield microscopy, single point confocal microscopy employs a point detector. Thus, only a single point (or pixel) of the two-dimensional FOV is observed at a given moment in time. To acquire a $N = 10^6$ pixel image requires 10^6 exposures, one at each scan point. If one wishes to record this image within 1 s, the integration time per pixel cannot exceed 1 μs. The excitation intensity at the focal spot must be increased one million-fold over the widefield case if the acquisition time of the complete image is to be maintained. At these elevated excitation intensity levels, one must be careful to avoid saturation effects [12].

During an excitation/emission cycle, a fluorophore spends a small but finite amount of time in an excited state before relaxing down to its ground state and emitting a photon. When in the excited state, the fluorophore cannot accept another photon for its usual fluorescent cycle. At low excitation intensities, fluorophores spend the vast majority of the time in the ground state waiting to be excited into a fluorescent emission cycle. As the excitation photon flux is increased, fluorophores spend a larger proportion of their time in an excited state where they are unavailable for another single photon excitation/emission event. The excitation photons see a smaller population of fluorophores available for excitation as this proportion of occupied fluorophores grows. As a result, the relationship between fluorophore density and fluorescent emission becomes nonlinear, making quantitative interpretation of fluorescent images difficult. Because of this nonlinearity, this regime, called saturation, is to be avoided in fluorescence microscopy (unless of course the goal is multi-photon fluorescence). Fluorophore saturation imposes a fundamental limit to the rate at which fluorescence can be extracted from a sample. In general, fluorophore saturation is not an issue in widefield fluorescence microscopy because the excitation intensity is low and the integration time is relatively long. Spinning disk confocal microscopes are also essentially immune to saturation effects because the excitation dose is spread out over many excitation spots [15]. For this reason, along with the faster scanning mechanism, spinning disk confocal microscopes are able to operate at much higher speeds than their single beam counterparts.

1.2 High Content Screening (HCS)

One crucial part of modern drug development involves the quantification of the response of a population of cells to a candidate compound using an *in vitro* assay. A drug company will screen compounds to test their interaction with cells, e.g. cancer cells [16]–[18]. For example, a cell culture could be exposed to the compound at a variety of concentrations, while recording the resultant cell morphologies or production rates of a given protein. Various types of assays are listed in Figure 1-4a, and a translocation assay is shown schematically in Figure 1-4b-g. The effectiveness of the compound can be evaluated based on whether the desired cellular response is observed. A screen that returns a multitude of parameters extracted from images of cellular response is called a "high content screen". HCS comprises many disciplines, as listed in Figure 1-5a; a large knowledge base is needed for proper assay design, implementation and interpretation.

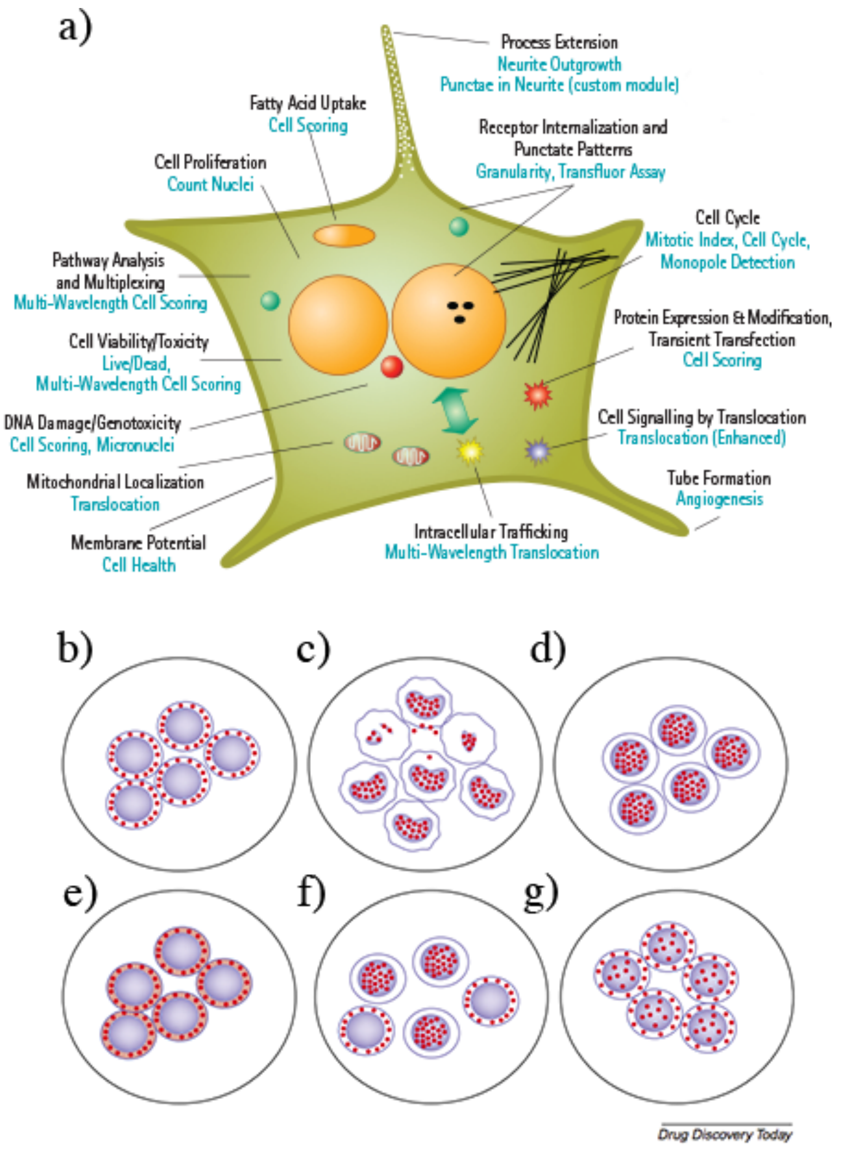

Drug Discovery Today

Figure 1-4 a) High content screening assay types, adapted from [19]. b)-g) Possible outcomes of a translocation assay, adapted from [20], with permission from Elsevier. b) Initial state – protein located in cytoplasm. c) Translocation of protein into nucleus with toxicity as indicated by cell morphology. d) Complete translocation. e) No translocation. f) Translocation in a subset of cells. g) Partial translocation in entire cell population.

High content screens are done on a massive scale. It is not uncommon to test upwards of tens of thousands of compounds, and each compound might be tested at a range of concentrations [16].

To maximize efficiency, tens to thousands of cellular response experiments are performed simultaneously in compartmentalized substrates called microwell plates (96-well plates are shown in Figure 1-5b). Each compartment (well) hosts a single experiment where a cell culture is exposed to a compound at a particular concentration. The bottom of each well is a thin optically clear substrate, made of either plastic or glass. Microplates come in standardized formats, typically with 96 or 384 wells. The standardization of well plate dimensions facilitates robotic handling so that screens can be run semi-autonomously on a 24/7 basis if needed [21].

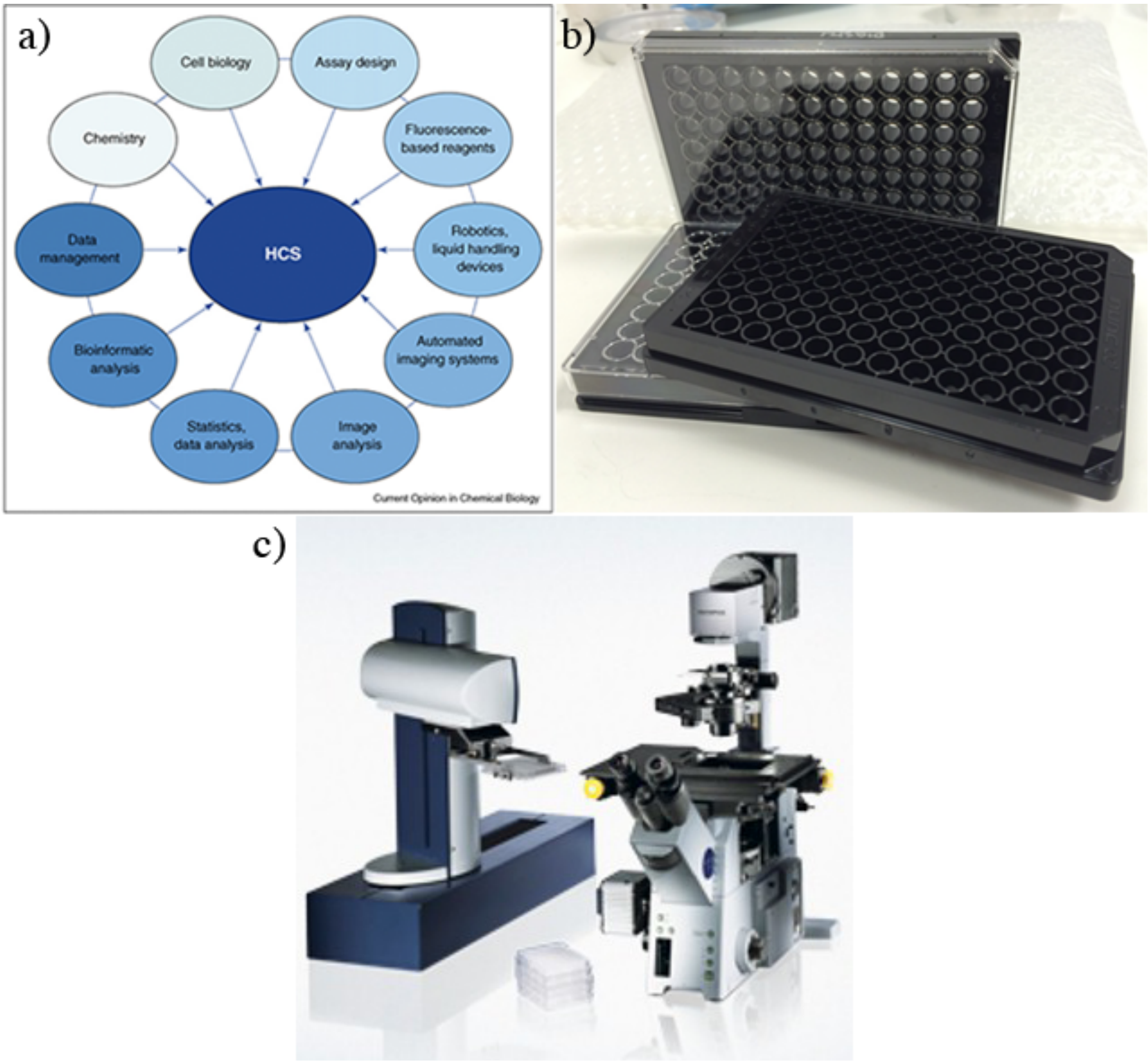

Figure 1-5 a) The various disciplines involved in high content screening. Section 3 is concerned with "Automated imaging systems." Adapted from [22], with permission from Elsevier. b) 96-well microplates. c) Olympus Scan^R automated microscope for HCS (right). The microscope is coupled with a robotic microplate loader (left). Adapted from [23].

During a high content screen, microwell plates are loaded sequentially into an automated microscope that images the cell cultures in each well. A typical widefield epifluorescent automated microscope, the Olympus Scan^R, is shown in Figure 1-5c alongside a robotic plate loader. The vast majority of high content screens employ fluorescent microscopy because of its ability to highlight specific cellular structures or proteins. For example, 4',6-diamidino-2-phenylindole (DAPI) and Hoechst 33342/34580 are nucleic acid stains that are used to highlight the cell nucleus. Similarly, microtubules and actin filaments can be stained with fluorescein isothiocyanate (FITC) and phalloidin derivatives to show the morphology of the cell cytoskeleton. Fluorescence micrographs of each cell culture are recorded and stored in a computer and subsequently subjected to image processing. A wide array of parameters are extracted via supervised image analysis [24], [25]. Examples include cell and nucleus area, perimeter, ellipticity and texture, nucleic fragmentation, and protein fluorophore localization and colocalization.

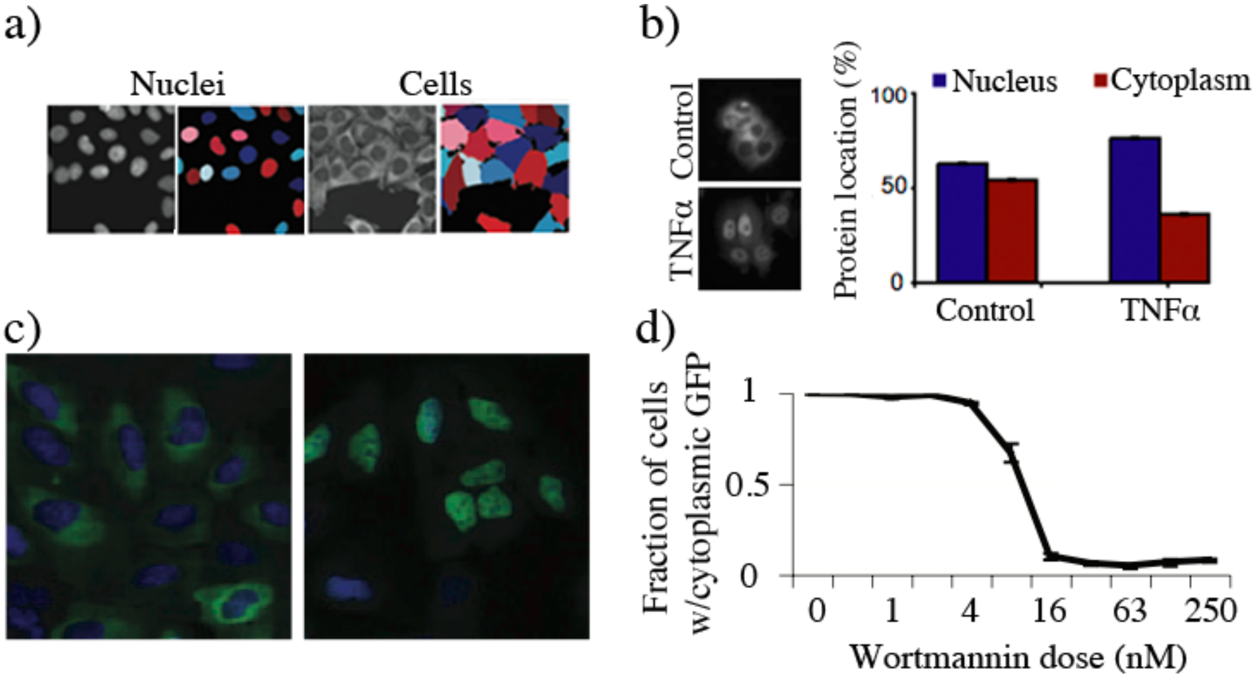

Figure 1-6 a) Example of identification of nuclei and cells from fluorescence microscopy images by CellProfiler cell image analysis software [24]. b) Protein location with introduction of tumor necrosis factor alpha (TNFα). c) Translocation assay images. Nuclei are shown in blue and GFP in green. Doses are 0 nM Wortmannin (left) and 150 nM Wortmannin (right). d) Dose response curve for assay in (c). Figure adapted from [24].

In this thesis, we are interesting in improving the speed with which automated microscopes acquire image data. In the following subsections we discuss the optomechanical features of current automated microscopes, and identify what limits their throughput.

1.2.1 Automated Microscopy

Typical high content screening laboratories can produce upwards of tens of gigabytes of data per day [16]. This image data in turn needs to be processed by software in order to produce meaningful and interpretable results. Such large-scale image analysis is a challenge unto itself and has spawned a whole field of semi-automated image processing [24]. Image analysis time can be made more manageable by increasing processing power or development of more efficient and robust image processing routines. In addition to the processing of images, their acquisition can take an extraordinary amount of time.

Consider the imaging of a single 96-well microplate, with well dimensions of 7.3×7.3 mm [26]. Such a microplate has a total sample area of $96 \times 7.3 \text{ mm} \times 7.3 \text{ mm} = 51.15 \text{ cm}^2$. A typical imaging resolution for a high content screen is $1\ \mu m$, therefore the microscope images must have a sampling rate of at least $0.5\ \mu m/\text{pixel}$ according to the Nyquist criterion. At this sampling rate, the entire 51.15 cm^2 area of the microplate will be represented by a total of at least 20.46 gigapixels. At the time of writing, however, scientific camera image sensors have pixel counts on the order of 1 to 5 megapixels [27], [28]. As a result, anywhere from 4,092 to 20,460 separate images must be acquired and stitched together to fully sample the entire microplate. Even if the image sensor were much larger, optical scaling considerations would quickly limit the diffraction-limited FOV to approximately 10 megapixels with standard microscope objectives [29], [30]. This occurs because optical aberrations scale with the size of the imaging system whereas the diffraction limit depends only on the wavelength. One cannot simply increase the size of a microscope objective to achieve a larger FOV because at some point the resultant aberrations will lead to an unacceptable degradation in the resolution. Rather than continually increasing as the microscope objective is increased in size, the number of points it can resolve (called the space-bandwidth product) will saturate in the absence of a more complicated lens design [31].

Today's automated microscopes used for high content screening record $10^3 - 10^4$ sub-mm scale FOVs sequentially and then stitch them together to form a final image. In between each successive FOV acquisition, a variety of mechanical movements are performed. The sample is translated by a motorized stage by a distance equal to the size of the microscope FOV. The focal plane of the microscope is then adjusted by moving the objective along the optical axis. The feedback for this autofocusing routine can be either hardware- or software-based. Hardware based focusing systems monitor the height of the sample by observing the position of an infrared laser beam reflected from the sample substrate surface [16]. Software systems acquire several images and choose the in-focus plane using an image sharpness metric [32], [33]. Finally, fluorescence filters may also be adjusted concurrently in order to image different fluorescent tags within the specimen.

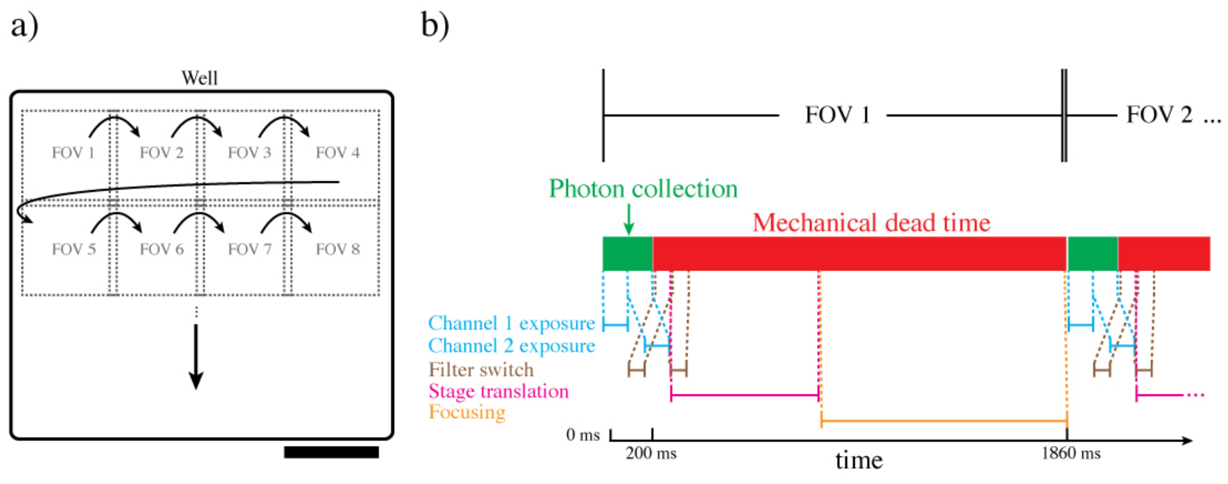

Figure 1-7 a) Multiple FOVs (width 1 mm) are needed to cover the area of an entire well (width 4mm). FOVs are image sequentially and stitched together in software. Scale bar is 1 mm. b) Comparison of time spent collecting photons vs. mechanical movements in an automated microscope. Integration time per channel: 100 ms; filter change: 60 ms; stage translation & settling: 600 ms; focusing: 1000 ms. Photon collection duty cycle is approximately 10%.

The mechanical movements of the microscope and their associated temporal overhead are shown schematically in Figure 1-7. We assume that the scanning stage has an acceleration of

$2000\ \mathrm{mm/s^2}$ and a settling time of 0.6 s, as per the specifications of a typical high speed stage [34]. With a widefield FOV of 1×1 mm, the combination of stage movement and settling time takes 0.63 sec/position. After the stage has settled, autofocusing can be performed. The Olympus Scan^R is quoted as having a 1-2 sec/position focusing time for hardware-based autofocus and 2-5 sec/position for software-based autofocus [23]. Typically at least two fluorescent channels will be imaged per position. Depending on the logistics of the experiment and the design of the microscope, a filter change may be required one or more times per position. The Olympus Scan^R specifications estimate that a time of 58 ms is needed to switch between filters. Any residual chromatic aberration due to the objective lens can result in additional time needed for autofocusing. The combination of these factors means that the time needed for each image FOV ranges from 0.63 to over 6 seconds. This does not include the photon collection time itself, which can only start after all of the mechanical movements are completed. As is evident from Figure 1-7b, the percentage of time that the microscope spends actually collecting photons is low, on the order of 10% [16].

The typical imaging speeds of high throughput fluorescence microscopes are not widely reported. Useful information can sometimes be found in HCS review literature. Here, we summarize our findings of the performance of the commercial systems that are state-of-the-art at the time of writing. For example, a run time comparison of a representative HCS assay on a Thermo Scientific Array Scan II, V^{Ti} and GE IN Cell 3000 yields imaging rates of 1.9-3.25 s per FOV [16]. Imaging throughput can also be deduced from manufacturer specifications. For instance, the Olympus Scan^R imaging platform attains an imaging rate no faster than 1 position/second [23]. If coupled with a 4 megapixel (Mpx) camera, this amounts to a pixel throughput of 4 Mpx/s, before stitching overhead is taken into account. Another estimate can be obtained using information from the specifications sheet of the Molecular Devices ImageXpress Micro XL [35]. This document states a 384-well microplate imaging time of 14 minutes, with single $0.7\times0.7\ \mathrm{mm}$ FOV being imaged per well. Each FOV image is acquired with a $20\times$ microscope objective, and comprises 4.66 Mpx. Two fluorescent channels are acquired for each FOV. This amounts to 2.19 seconds per FOV. The total pixel throughput of this system can be estimated as $384\ \mathrm{wells}\times 2\ \mathrm{channels}\times\ 4.66\ \mathrm{Mpx}/14\ \mathrm{minutes} = 4.26\ \mathrm{Mpx/s}$ per fluorescent channel. This is approximately equal to the throughput estimated for the Olympus Scan^{R} system.

1.2.2 Pixel throughput limits

A major motivating factor for this work is that the 4-5 Mpx throughputs of current automated microscopes do not approach the throughput limits of the cameras used in these systems. Cameras with pixel throughputs exceeding 100s of Mpx/s are readily available as both scientific and consumer grade products. Why, then, are automated microscopes not achieving these throughputs?

One may first suspect that fluorophore saturation effects may be to blame for the low throughputs of automated microscopes. Consider some typical working parameters of a confocal microscope, operated in a regime that is below saturation. The total excitation power in a focal spot is on the order of $10\ \mathrm{to}\ 100\ \mu\mathrm{W}$ with pixel dwell times ranging from roughly $1\ \mathrm{to}\ 10\ \mu\mathrm{s}$ [12]. Thus, a total dose of $0.01\ \mathrm{to}\ 1$ nJ per pixel is typical in a confocal imaging experiment. Suppose we wish now to instead use a widefield configuration, but with the same excitation dose for each pixel. For a 4 Mpx image sensor, this would require total dose of somewhere between 0.04 to 4 mJ. We now consider whether the imaging throughput will be limited by delivery of this energy to the sample due to restrictions on laser power and/or by fluorophore saturation effects. To this end, it is instructive to now consider what laser power would be required for this energy to be delivered to the sample in a time period equal to mechanical settling time of the stage (at least 0.6 s). To obtain an upper limit on the laser power needed, we take the dose as 4 mJ. Delivery of such a dose to the sample in 0.6 s requires ~6.7 mW of excitation power at the sample, spread out over the entire FOV. A tenfold reduction in exposure time (down to 60 ms) takes ~67 mW of excitation power. A further decrease in exposure time by an order of magnitude (down to 6 ms) necessitates an excitation power of 670 mW. Such a power level is feasible with the multi-watt laser sources that are currently available. Note that this dose is delivered to the sample ~1000 more slowly than in the confocal case so there is no threat of fluorophore saturation in widefield microscopy. In other words, an exposure time (of 6 ms) that is ~100 times smaller than the mechanical settling time of the stage (0.6 s) is feasible from a laser power and fluorophore saturation standpoint. This leads to the conclusion that photon collection time is not the source of the throughput limits that current state-of-the-art fluorescence microscopes face. This conclusion is supported by the run time study in [16], Table 2.2. In that work, the time needed to scan an entire plate was 15 min 35 s, of which the total exposure time was at most 118 s. Photon collection therefore comprised only ~12% of the time needed to acquire an image of the entire plate.

The mechanics of the microscope stage movement appear to be limiting the pixel throughput of high content imagers. How can the mechanical architecture of the automated microscope be altered to alleviate this bottleneck? This is the major question addressed in Section 3 of this thesis.

1.2.3 Alternative microscope architectures

Consider a widefield microscope that continuously scans the sample underneath the objective lens. Let us assume that the sample is perfectly flat and parallel to the focal plane of the microscope objective so that no focus adjustments are needed during imaging. Suppose the microscope camera is continuously capturing frames at a rate of 200 Hz. Between each frame the sample must move by a distance equal to the lateral size of the microscope FOV - typically between 500 μm to 1 mm - in order to capture the subsequent image tile. This presents a significant motion blur problem. The typical resolution of an automated microscopy scan might be on the order of 1 μm, but the amount of sample motion described above would blur the point spread function (PSF) in the scan direction up to 1 mm. One can combat this motion blur by reducing the exposure time or by using a "time delay integration" (TDI) camera. TDI cameras electronically scan electrons across the image sensor at the same speed as the sample image to eliminate motion blur and increase signal. TDI-based systems have been investigated as high throughput slide imaging systems but have not attained widespread use, likely due to the complexity of the system - up to 9 cameras are involved in order to continuously update the sample height. The reader is referred to [36] for more details.

The common route for eliminating motion blur in a dynamic system is to strobe the illumination such that the sample moves a distance equivalent to the resolution limit during a single frame. For a 1 mm wide FOV and a resolution limit of 1 μm, this means a thousand-fold reduction in exposure time and an accompanying thousand-fold increase in excitation laser power. With this pulsed illumination scheme, we must deliver 4 mJ of power to the sample plane within 5 μs, necessitating an excitation power of 800 W. The excitation power per pixel is no larger than in the confocal case so we do not expect to be saturating fluorophores. Unfortunately, however, delivering 800 W of continuous wave laser power to the sample is completely unreasonable.

Note that in the pulsed illumination scheme above, the excitation duty cycle increases with shrinking FOV. Let us shrink the FOV to half the size of the PSF and increase the illumination duty cycle to unity. This is precisely the arrangement of a laser scanning microscope that operates at the Nyquist sampling rate. Here, the "FOV" (ie. the pixel size) is smaller than the intrinsic blur of the PSF (i.e. its finite width). As the sample moves by one "FOV" laterally within a single camera frame, the motion blur over half of the extent of the PSF is negligible compared to the finite width of the PSF. Unfortunately we have come full circle and returned to a scanning microscope with limited pixel throughput.

In Section 3 of this work we develop a microscope on microlens arrays. It is somewhat reminiscent of a spinning disk confocal microscope (but with key differences). An array of focal spots illuminates the sample that is in turn raster-scanned by using a piezoelectric stage. As discussed above, the fluorescence at each focal spot can be monitored continuously without the onset of motion blur. In other words, the integration time duty cycle can be nearly 100%. Operating a camera at several hundreds of frames per second (fps), while imaging $10^3 - 10^5$ focal spots simultaneously, ensures a high pixel throughput.

1.3 Microlens Arrays

A collection of lenses arranged in a grid is called a lens array. The extent of the array is typically mm-scale or larger, and the element size can range from a few optical wavelengths to mm- or even cm-scale. Common examples include diffusing covers for fluorescent lighting (mm-scale elements) and light collection aids in digital camera sensors (μm-scale elements) [37], [38]. Large-scale arrays can be made with injection molding for industrial scale production [39], while arrays with smaller elements for applications requiring tight tolerance and high quality may require photolithography and/or reactive ion etching [40], [41]. Typical lens array materials are polymers and glass for visible wavelengths, whereas more exotic materials such as Si are used for applications in the infrared [42], [43].

Lens arrays with element sizes <$1000\ \mu m$ are termed microlens arrays. Microlens arrays are used for a broad variety of purposes that fall into roughly three categories: light shaping, light collection, and imaging. A sampling of light shaping applications include flat beam generators for laser micromachining [44], optical displays [45]–[47], and efficient street lighting [48]. Consumer digital cameras employ microlens arrays to increase the effective pixel fill factor in order to boost light collection efficiency [38], [49], [50]. Microlens arrays have also been used to trap light in thin film photovoltaic cells [51]. Spinning disk confocal and multifocal multiphoton microscopes exploit microlens arrays to increase imaging speed and efficiency [52], [53]. Ultra-thin imaging systems can be created with microlens arrays [54], [55]. Light field cameras (also known as integral or plenoptic imagers), and wavefront sensors are able to extract directional and phase information by using a microlens array in tandem with imaging optics [56]–[62]. At the time of writing, the Crozier lab recently used microlenses integrated with microfluidic devices for high throughput flow cytometry applications [3], [63]. These last works are the starting point and inspiration for a majority of the work in this thesis.

Microlenses fall into two main categories: static and tunable. Static microlenses are fabricated with fixed optical properties that cannot be altered after production [39], [42], [64]. Tunable microlenses, however, can be subjected to a stimulus that alters one or more optical parameters, usually focal length [65]–[68]. In the next sub-subsection, we will describe fabrication techniques for static microlenses. This is followed by a discussion of an application of tunable microlenses to microfluidics in the following subsection.

1.3.1 Microlens Fabrication Techniques

The microlens array fabrication process consists largely of two steps: master fabrication and replication. Although the replication step is not essential, it can be far more economical to fabricate a master out of a material that is easy to shape (such as photoresist) and then produce a copy from a material, e.g. an optical grade polymer or glass, that has superior optical properties but for which direct fabrication is more difficult.

1.3.1.1 Master Fabrication

The most common method for making a microlens array master is thermal reflow molding [42], [64], [69], [70]. In this technique, photolithography is used to fabricate an array of low aspect ratio posts of photoresist with a low melting point. The post array is heated to a temperature that exceeds the glass transition temperature of the resist. This turns the posts into smooth droplets that then solidify upon cooling. Because of its convex surface, each droplet focuses light just like a lens. The shape of the droplet is roughly spherical, being influenced by the surface energies between the resist and the substrate. Critically, surface tension results in an extremely smooth convex surface, essentially eliminating any surface scattering that would degrade optical performance. This technique for fabricating the array master is used extensively in this thesis and is described in more detail in Section 3.1.1. A microlens array fabricated from a master template is shown in Figure 1-8a. The master template is shown as Figure 1-8b.

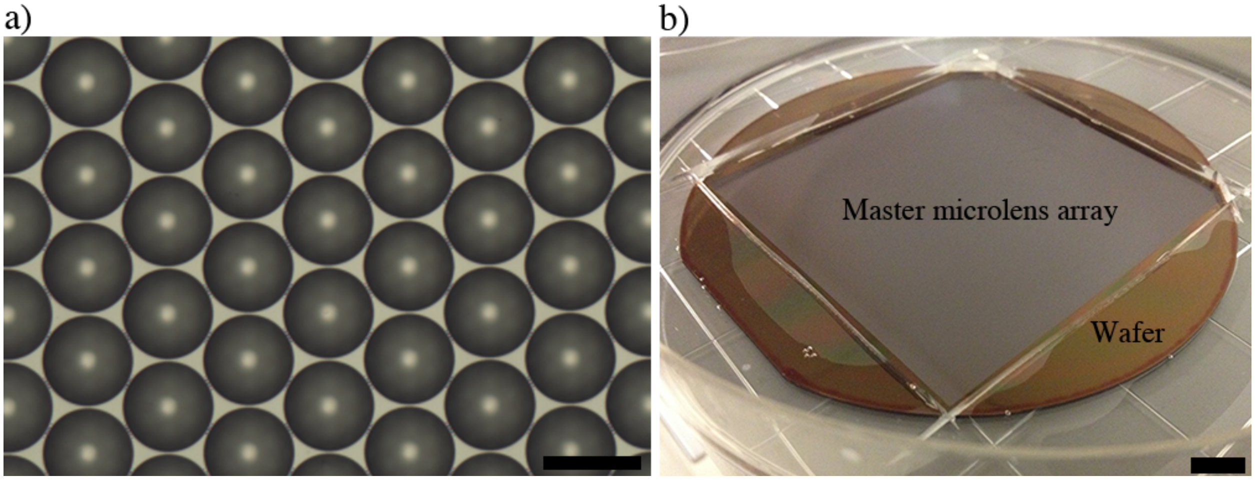

Figure 1-8 a) Brightfield reflection micrograph of a microlens array replica fabricated in Norland Optical Adhesive 61. Scale bar is $125\ \mu m$. b) A master microlens array, fabricated in photoresist on a silicon wafer. The master microlens array provides the shape template for the microlens array. A negative copy (stamp) of this master microlens array has been fabricated by curing poly(dimethylsiloxane) (PDMS) on top of the wafer. The PDMS directly on top of the microlens array master has been removed in this photograph. Scale bar is 1 cm. Both of these samples were fabricated for the work presented in Section 3.

More exotic master fabrication techniques can be used to precisely control the microlens shape. Femtosecond lasers can be used to write a desired 3D microlens volume in resist using two-photo polymerization [71], [72]. Alternatively, femtosecond lasers can be used to selectively ablate or photoetch a starting material into a accurately shaped lens [73], [74]. These techniques lend a remarkable amount of freedom to the design process but are unfortunately high-cost and slow. Fabrication of a cm-scale array, in a direct writing fashion, can be prohibitively slow because a three dimensional space of voxels in the microlens array needs to be addressed by the laser as opposed to only a two dimensional space in standard photolithography. Grayscale photolithography presents a compromise between reflow molding and full 3D control of the microlens shape [75]–[78]. With a positive photoresist, a larger (smaller) ultraviolet (UV) dose results in a shorter (taller) feature. Therefore, by controlling the UV exposure as a function of position, the profile after development can comprise a microlens shape. In the absence of thermal reflow, such microlenses can have significant surface roughness. On the other hand, thermal reflow tends to reshape the resist away from the intended profile towards a more energetically favorable state, mitigating the advantage to be gained by shaping the microlens.

1.3.1.2 Replica Fabrication

Master microlens arrays can be expensive and time consuming to fabricate. Additionally, photoresists display strong absorption at UV and short visible wavelengths, making them poor materials for lenses. For these reasons, rather than being used directly, replication processes are used to transfer the microlens array shape to other materials with favorable optical properties. Such processes can be low cost and capable of high volumes.

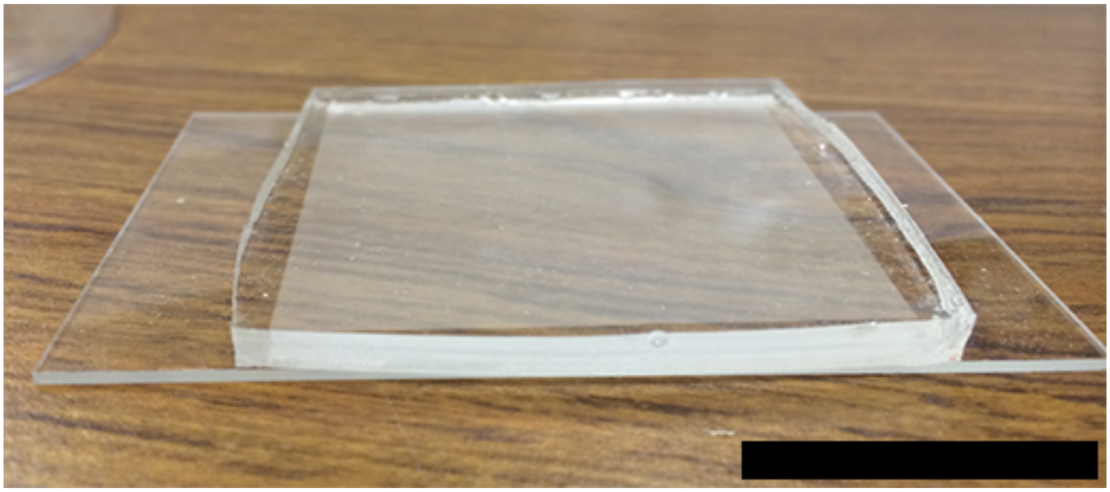

Figure 1-9 PDMS stamp of a microlens array master. This block of PDMS corresponds to the missing PDMS square in Figure 1-8b, though the actual master wafer for this PDMS stamp in not the one shown in Figure 1-8b. The microlens array is placed face down on a microscope slide. During replication, optical adhesive (Norland Optical Adhesive 61) would be sandwiched between the stamp and the glass slide. The glass slide becomes the substrate for the microlens array. Scale bar is 25 mm.

Stamping replication processes use an intermediate negative replica of the microlens array master (the stamp) to reproduce the microlens array. A common stamp material is poly(dimethylsiloxane) (PDMS). PDMS stamps are constructed by mixing a liquid precursor with a curing agent and pouring the blend onto the microlens array [79]–[81]. The liquid PDMS is then thermally cured and released from the master. Figure 1-8b shows a microlens array master that has been used as a template for a PMDS stamp and a photograph of a PDMS microlens array stamp is shown in Figure 1-9. Cured PDMS is a flexible rubbery material and does not adhere to photoresist, making separation of the negative replica from the master easy. With a negative replica stamp in hand, the master can be replicated in the desired optical material, for example a UV curable adhesive. The pre-cured optical material is sandwiched between a substrate (eg. glass) and the stamp and cured. The stamp is then removed, leaving a positive replica of the master lens array. Similar processes involving molding or embossing a negative replica of the microlens array are used for industrial scale production [39], [82]–[84].

1.3.2 Micro-optics in Microfluidic Pressure Sensing

The ability to efficiently fabricate micron scale fluidic channels has led to a surge in the miniaturization of fluidic devices [3], [85]–[88]. Figure 1-10a,b shows a multi-layered microfluidic device where hundreds of integrated valves enable the control of fluids around a chip. Along with the ability to produce complex microfluidic devices, there is a need to be able to probe the state of the device by monitoring crucial physical parameters, such as pressure and flow rate. An easy-to-use pressure measurement platform would be of great benefit for both studying microscale flow and live monitoring of lab-on-a-chip functionality [88]. Existing pressure measurement schemes for microfluidic chips typically involve electrical or optical read out [89]–[97]. Optical schemes involve measuring the deformation of microchannel walls with beam deflection [91], interferometry [95], [96] (Figure 1-10c), and particle or interface tracking [90], [92], [93], [97].

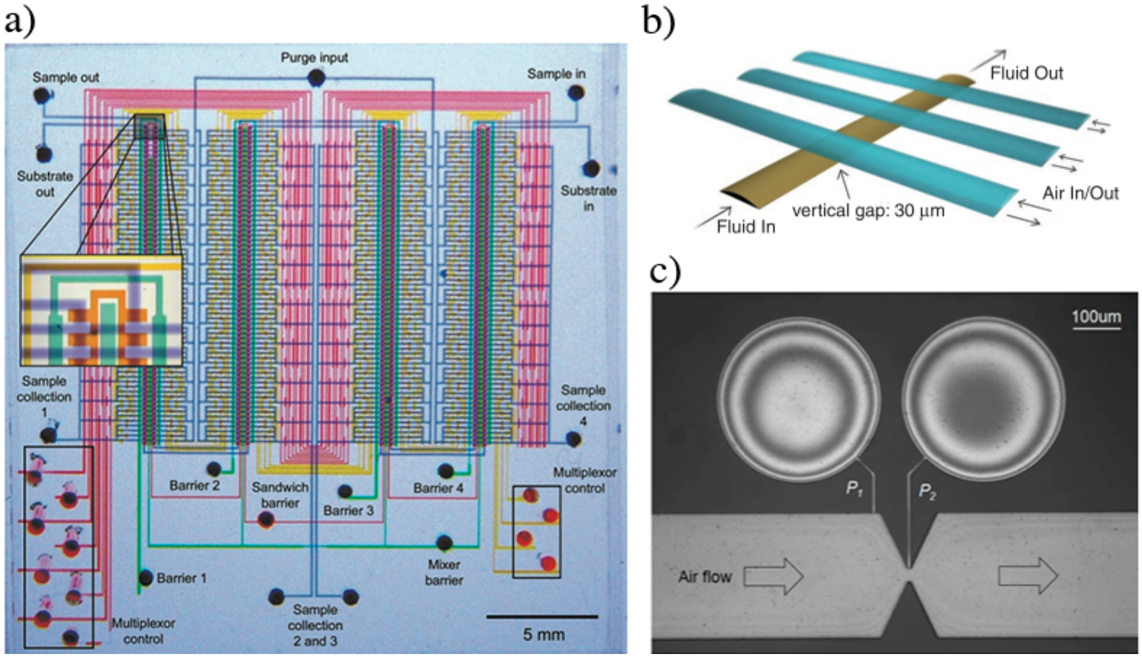

Figure 1-10 a) Multi-layer microfluidic comparator device. Dye has been added to each layer for visibility. Sample and substrate flow through the channels dyed in blue. Other colors indicate independently actuated circuits consisting of pneumatically actuated valves. Inset shows a magnified view of multiplexor (orange) and barrier valves (green) on top of sample and substrate channels (blue). Figure from [85]. Reprinted with permission from AAAS. b) Schematic of three microfluidic valves over top of a fluidic channel. Increasing the air pressure in the blue channels deflects a PDMS membrane into the fluidic channel, blocking fluid flow. Figure from [88]. Reprinted with permission from AAAS. c) Optical microfluidic pressure sensor fabricated out of PDMS. Two disk-shaped air cavities are attached to a microfluidic channel. Air pressure deforms the PDMS air cavities, leading to interference fringes that are images by a camera. The pressure can be directly related to the image of the interference fringes by a calibration procedure. Reproduced with permission from the OSA [96].

Elastomeric materials can be designed to alter their shape in response to flow properties such as pressure, temperature and pH [88], [98], [99]. Flexible and transparent materials such as poly(dimethylsiloxane) (PDMS) are especially intriguing as optical materials given that their flexible nature allows tunability in an optical system. Several groups have developed PDMS microlenses with pneumatically adjustable focal lengths based on pressurized fluid filled microfluidic reservoirs bounded by flexible transparent membranes [65], [67], [100]. These microlenses can display a wide range of focal lengths owing to the cubic variation of the membrane stiffness with its thickness [101], [102].

In Section 2 we introduce a novel application of pneumatically tunable microlenses. Instead of using pneumatic microlenses as tunable imaging lenses, we leverage their pneumatic response to report the local fluid pressure. The main benefit of using a small microlens structure for pressure sensing is the ability to perform spatially resolved measurements as well as minimizing hydraulic capacitance which speeds temporal response [103].

1.4 Light Field Imaging

The term "light field imaging" refers to techniques that captures not only the intensity of light as a function of position, but also its direction. Though the technique has received considerable renewed interest due to introduction of commercial products [59], the technique was first described as "integral photography" in 1908 by Lippman [42], [104]. Lippmann's scheme involved a lens array to both image and re-display an object, giving the observer a sense of parallax, and therefore depth. In 1930, Ives realized a more practical version that bears a closer resemblance to today's light field cameras [105]. Today, the microlens arrays needed for these imagers are easily mass-produced, and the integral photographs they produce may be digitally stored and manipulated. These two factors have led to a revitalization of integral photography (or light field photography) research and development.

1.4.1 Defining the light field

Traditional imaging devices record a (de)magnified version of the spatial distribution of light at a given two-dimensional plane. In the ray optics picture, the light distribution at this plane can be thought of as a continuum of infinitesimal planar sources, each radiating photons with its own particular angular distribution. The full spatio-angular description of light rays at a given plane is therefore given by a scalar four-dimensional function called the light field $\bar{L}(x, y, \theta, \phi)$, where (x, y) spatial coordinates and (θ, ϕ) are the traditional polar and azimuthal angles as defined in spherical coordinates (Figure 1-11a). The quantity $\bar{L}(x, y, \theta, \phi)\cos\theta\sin\theta dxdyd\theta d\phi$ is the differential power radiated from the location (x, y) into the direction defined by (θ, ϕ). The light field, $\bar{L}(x, y, \theta, \phi)$, has units of power per unit steradian per unit area: $\mathrm{W} \cdot sr^{-1} \cdot m^{-2}$. In radiometry literature, $\bar{L}(x, y, \theta, \phi)$ is called the “radiance” [106], [107]. The term “light field” dates back to a publication by Gershun in 1936, however it differs from the scalar light field used in the computer graphics community [106], [108]–[110]. Gershun’s light field $\vec{L}_G$ is a vector quantity, related to today’s scalar light field $\bar{L}$ by: $\vec{L}_G = \iint \bar{L}\,(r, \vec{n})\vec{n}d\Omega$, where $r = (x, y)$, $\vec{n}$ is a unit vector, $d\Omega$ is the differential solid angle and the integral is performed over all solid angles. Gershun’s light field now goes by the name “vector irradiance field” in the modern parlance [109], [110].

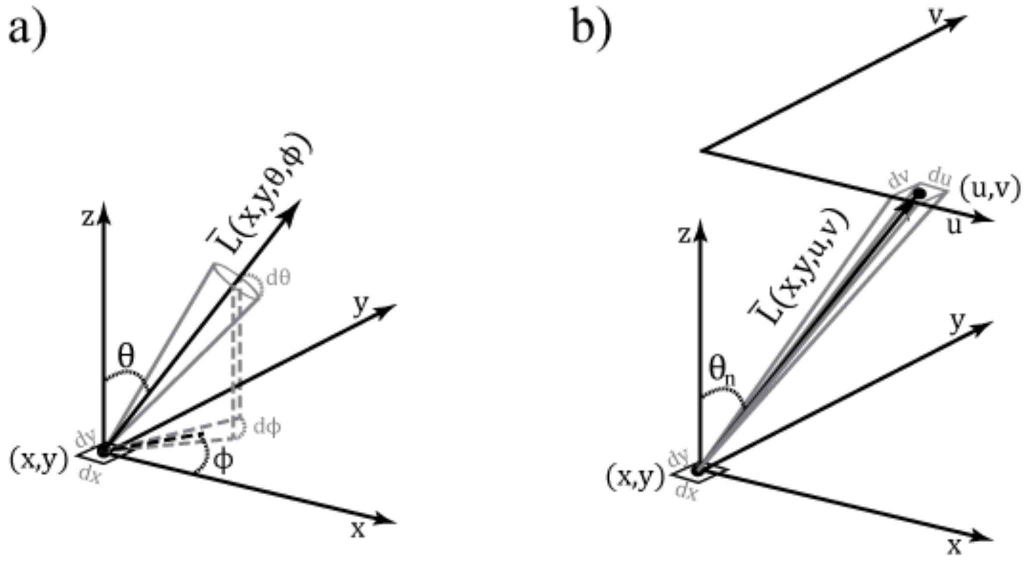

Figure 1-11 a) Spherical coordinates parameterization of the light field. B) Two-plane parameterization of the light field.

The angular parameterization $\bar{L}(x, y, \theta, \phi)$ is not unique nor is it common in today's light field literature. Most often the light field is given by the so-called two-plane parameterization, as depicted in Figure 1-11b [111]. Consider two parallel planes separated by a unit distance. The spatial coordinates on the first plane are given by (x, y) and on the second plane by (u, v). The power flux that crosses both the differential patches at (x, y) on the first plane and (u, v) on the second plane is given by $\bar{L}(x, y, u, v) \cos^4 \theta_n dxdydudv$ where θ_n is the angle between the plane normal and the line connecting the points (x, y) and (u, v). One can substitute $\cos^4 \theta_n = [1 + (x - u)^2 + (y - v)^2]^2$, however, the $\cos^4 \theta_n$ factor is typically ignored in practice and absorbed into the definition of the light field to form what we will call the observed light field $L_o(x, y, u, v) = \bar{L}(x, y, u, v) \cos^4 \theta_n$ [112].

A conventional camera only captures the spatial component of the light field. The recorded image $I(x, y)$ can be represented by an integral of the observed light field at the image sensor over its angular coordinates:

$$I(x, y) = \iint L_o(x, y, u, v)\, R(\theta) du dv \tag{1-1}$$

Where $\mathrm{R}(\theta)$ accounts for the angular response of the pixels and the particular illumination factors associated with the imaging optics. Once again the angular factor $R(\theta)$ is incorporated in a more compact representation which we shall call the recorded light field: $L(x, y, u, v) = L_o(x, y, u, v) R(\theta)$. This is the light field that is actually available to be recorded at the image sensor of a camera.

1.4.2 Manipulating the light field

The goal of a light field imager is to capture the recorded light field. Once that data is in hand, one can manipulate it in a number of ways.

Consider an imaging geometry where (x, y) are the coordinates of the object plane and (u, v) are the coordinates of the camera aperture plane. Suppose we apply a filter $\delta(u - u_0, v - v_0)$ to a recorded light field and construct the resulting image $I(x, y, u_0, v_0) = \iint \delta(u - u_0, v - v_0) L(x, y, u, v) du dv$. The physical interpretation of this filter is that we are placing a virtual pinhole at the position (u_0, v_0) in the camera lens aperture. The filtered image $I(x, y, u_0, v_0)$ is therefore what the scene would have looked like if it had been viewed from the position (u_0, v_0). Each (u_0, v_0) coordinate represents a different viewing perspective. As the viewing perspective is changed, objects may become occluded (or unoccluded) by objects close to the camera aperture. Also, objects behind the in-focus plane will appear to shift in the opposite direction from those in front of the in-focus plane; the magnitude of the shift is proportional to the depth of the object. This forms the basis of depth mapping and is a generalization of the principle used in stereo imaging. The ability to manipulate the viewing perspective of a scene yields a convincing impression of depth. For this reason, light field imagers and displays are poised to be at the heart of next generation 3D media technology [58], [59], [113]–[115].

Light field data can also be used to correct for aberrations. Suppose two rays R_1 and R_2 leave the same scene point $P = (x_0, y_0)$ in different directions and are both collected by a lens. The rays R_1 and R_2 exit the aperture of a lens at the points (u_1, v_1) and (u_2, v_2), respectively. If these rays converge at the same point (x_i, y_i) in the image, then the there is a faithful reproduction of the scene point P in the image. However, if R_1 and R_2 hit the sensor at different points (x_1, y_1) and (x_2, y_2), respectively, then the image is aberrated. That is, the image is a distorted version of the original object. If light field data is available and the nature of the aberration known *a priori*, ray aberrations can be corrected. In our simplistic example, this means defining a new corrected image value at the image point under consideration $I_c(x_i, y_i)$ that receives the energy that had been recorded at the 4D positions (x_1, y_1, u_1, u_1) and (x_2, y_2, u_2, u_2):

$$I_c(x_i, y_i) = L(x_1, y_1, u_1, v_1) + L(x_2, y_2, u_2, v_2) \qquad \text{1-2}$$

The most commonly encountered aberration in imaging systems is defocus. This aberration causes the image to come into focus before or after the image sensor. Consider the general ray R propagating from the point (u, v) on the lens exit aperture towards the image sensor, located at a position z_s. The ray R hits the image sensor at the point (x', y'), and crosses the z_0 plane at position (x, y). It is straightforward to relate the light field recorded at the z_s plane with the light field that would have been recorded at the plane z_0 using basic trigonometry. Noting similar triangles in Figure 1-12, we can write:

$$(x - x', y - y') = \frac{z_s - z_0}{z_0}(u - x, v - y) \tag{1-3}$$

This relates the coordinates in the image sensor plane to the coordinates in the exit aperture and z_0 planes. The quantities $x - x'$ and $y - y'$ are the transverse ray errors in the x- and y-directions, respectively. Recalling the image formation integral in Equation 1-1 and using Equation 1-3 to write (x', y') in terms of (x, y) and (u, v), we can reconstruct the intensity $I_0(x, y)$ distribution that would have been observed had the image sensor been placed at z_0 [112]:

$$I_0(x, y) = \iint L(x\alpha + u(1 - \alpha), y\alpha + v(1 - \alpha), u, v)\,du\,dv \tag{1-4}$$

where $\alpha = z_s/z_0$. In other words, given the light field data at a plane of misfocus, one can computationally correct for the defocus aberration, yielding an in-focus image. Though it may not be obvious at first glance, Equation 1-3 is correcting for the shifts of out-of-focus objects as would be seen from viewing perspectives.

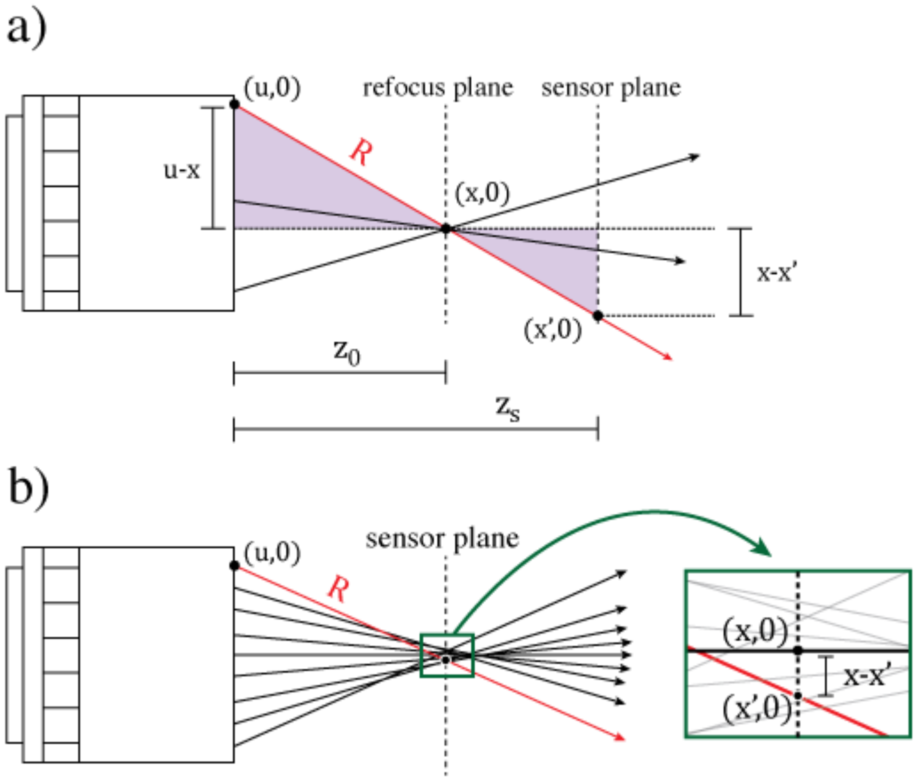

Figure 1-12 a) Ray diagram for light field refocusing. A lens images 3 rays to a point at $(x, 0)$ at the refocus plane. The sensor records a blurred image at the sensor plane. The transverse ray error of ray R at the sensor plane is $x - x'$. Purple shaded regions denote a pair of similar triangles. b) Ray diagram for light field correction of spherical aberration. A lens creates a focal spot with spherical aberration at the sensor plane. Inset: Magnified view of ray intercepts near the sensor plane. Rays other than the marginal ray are greyed out for visibility. The optical axis is indicated with a solid black line. Transverse ray error of ray R at the sensor plane is $x - x'$.

To correct for a more general aberration, one simply needs to insert the correct relationship between the actual ray position at the image sensor and its ideal corrected position, as a function of the aperture plane coordinates (u, v) [116]–[118]. For spherical aberration, for example, the correction takes the following form:

$$(x - x', y - y') = (S_1 u(u^2 + v^2), S_1 v(u^2 + v^2)) \tag{1-5}$$

Here, S_1 is a parameter indicating the strength and sign of the spherical aberration and (x, y) is the point at which the (x', y', u, v) ray would have hit the image sensor had spherical aberration been absent. As with defocus aberration one may digitally undo the spherical aberration to form a corrected image $I_c(x, y)$:

$$I_c(x, y) = \iint L(x - S_1 u(u^2 + v^2), y - S_1 v(u^2 + v^2), u, v) du dv \tag{1-6}$$

1.4.3 Light Field Imaging Systems

Adelson introduced the first digital light field camera in 1992 [119]. A similar arrangement was developed by Ng and Levoy at Stanford University and has now been developed into a commercial product sold by Lytro, Inc [58], [59], [120]. The Stanford light field camera consists of a main lens that forms a real image at the plane of a microlens array, as shown in Figure 1-13. Each microlens samples a small portion of the real image (ie. the portion of the image that falls within the microlens diameter). Because the main lens is much farther away from the microlens than the microlens focal length (ie. at optical infinity), the microlens array produces an image of the main lens aperture (for the rest of this section referred to as “the aperture”) at its focal plane. Thus each microlens creates a micro-image of the intensity at the aperture, scaled by the intensity intercepted by that particular microlens. This is a realization of the two-plane parameterization of the light field: microlens array inhabits the xy-plane, and each micro-image lies in its own uv space. To record the light field, one either re-images the microlens focal plane onto a digital image sensor, or simply places the digital image sensor at the microlens focal plane as is done in Figure 1-13. The image sensor pixels are grouped into collections of pixels called macropixels, each containing a single micro-image of the aperture. Each macropixel is assigned a spatial index (x, y) and each pixel within the group is identified by an aperture index (u, v). Extracting the 4D light field $L(x, y, u, v)$ is only a matter of organizing the image sensor data appropriately.

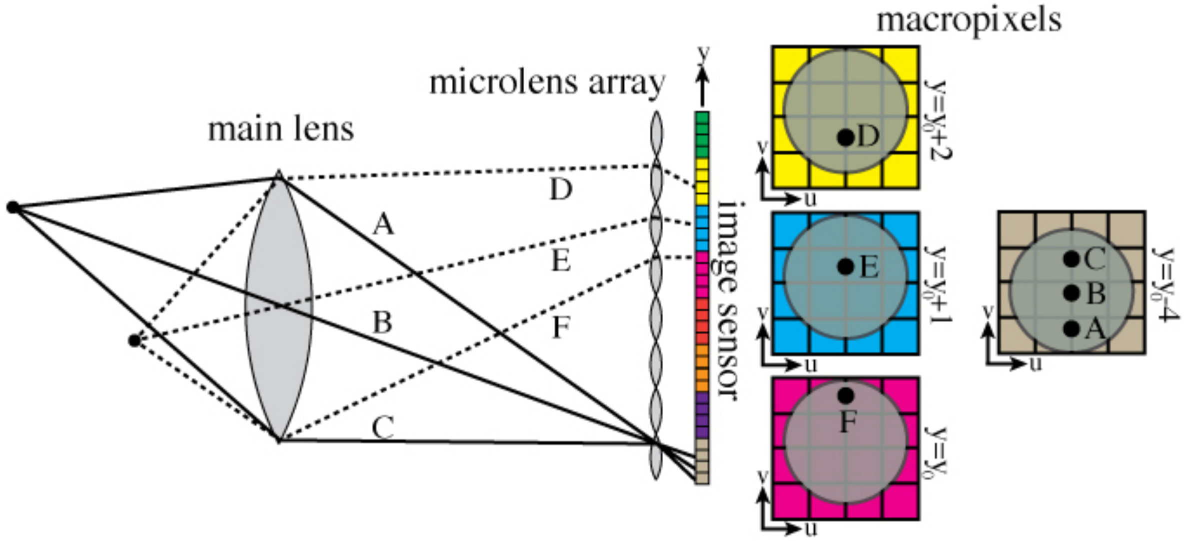

Figure 1-13 Schematic of Stanford microlens array based light field camera. A lens creates an image of a scene at the microlens array plane. The microlens array redirects rays onto an image sensor that is grouped into macropixels (4x4 pixels). Macropixels are identified by color and each corresponds to a different y-position in this figure. The circles within the macropixels are the micro-images of the main lens aperture. Rays A,B and C are imaged from an in focus scene point to the same macropixel (brown). Rays D,E and F originate from an out of focus point and are imaged to different macropixels (yellow, blue and pink).

The microlens array based system above is the most commonplace light field imaging system. An industrial grade variation of this camera, employing a microlens array with 3 different focal length microlenses is sold by Raytrix GmbH (Figure 1-14b) [59], [121]. Adobe has recently experimented with two geometries: one that places the image sensor slightly in front or behind the microlens focal plane, and another where the microlens array is replaced in favor of a large element lens array placed in front of the main lens [122], [123]. Yet another company, Pelican Imaging, is developing a compact module consisting of a 5x5 array of mm-scale microcameras arranged in a grid (Figure 1-14c) [59], [124]. There is yet another class of light field cameras that use absorptive masks instead of a refractive lens array in order to extract directional information from the light field. The simplest possible is a pinhole array placed at the image plane. The pinhole array plays much the same role as the microlens array but with significant loss and aliasing problems. More sophisticated mask-based systems that combine heterodyning principles and light field dictionaries have been developed at Mitsubishi Electric Research Laboratories and MIT Media Lab (Figure 1-14c) [125], [126]. Additionally, a light field image sensor containing a pair of gratings atop a photodiode array has been developed [127].

Figure 1-14 a) Lytro light field camera. b) Raytrix light field camera. c) Pelican light field camera module. Images are from [59], © 2011 IEEE.

All of these imagers rely on an extra element (eg. a microlens array or absorbing mask) to be placed in close proximity to an image sensor. This requires a redesign of the camera itself and lens array or mask must be precisely placed. The work in Section 4 of this thesis aims to replicate some of the abilities of light field imaging without altering conventional digital camera hardware.

2 Micro Optical Pressure Sensing

For a deep understanding of microscale fluid dynamics in single- and multi-phase flows, a toolbox for measuring basic flow properties such as flow rate and pressure is essential. The situation is analogous to the need for voltmeters and ammeters in order to probe an electric circuit. In microfluidic flows, pressure is analogous to voltage (potential energy of electrons), flow rate is the equivalent of electric current (flow of electrons) and hydraulic resistance plays the role of electrical resistance [103]. In this section, we present the development of a multiplexed optical pressure sensor for use in microfluidics. The pressure sensor is based on a pneumatically tunable microlens design that is fabricated entirely using soft lithographic techniques [88]. The compact size of the pressure sensor allows for the first time to our knowledge spatially resolved pressure measurements in a microfluidic network.

Similar to other microfluidic pressure sensing techniques, our pressure sensors use a membrane as the sensing element [89]–[91], [95]. The membrane is small enough (40 μm in diameter) that it does not dwarf typical dimensions of the microfluidic channels (tens of μm). Previous designs had dimensions of several hundreds of μm. Its compact nature allows multiple pressure sensors to be placed in close proximity for highly localized pressure measurements within a microfluidic network. Some microfluidic pressure sensors require fabrication steps such as reactive ion etching and sputtering that require expensive microfabrication equipment [91]. Our design uses only soft-lithographic fabrication techniques that are used extensively for the fabrication of microfluidic devices due to their simplicity and low cost [86]. Our pressure sensors are integrated into the microfluidics and interrogated optically, so that no external equipment other than a microscope is needed to perform experiments. The majority of microfluidic devices are operated with the help of a microscope, so our sensors require no additional equipment overhead.

Because the sensor is located in close proximity to the measurement region, the fluidic environment can be observed at the same time as the pressure is measured.

With previous optically based designs, this is only possible for a small region of the chip or with additional equipment such as a laser and photodiode [90], [91], [93]–[97]. Optically interrogated designs based on beam deflection or diffraction are also not amenable to multiplexing, severely limiting their range of applications [91], [94].

In this work we use pneumatically tunable microlenses to probe the local pressure in microfluidic channels. The pressure is read out optically by imaging the microfluidic device under a transmission microscope; the intensity of the focal spot of each lens is related to the deforming pressure using a family of calibration curves. In this manner, pressure can be spatially resolved at discrete locations in a microfluidic chip with high sensitivity. We note that the working principle is similar to that of an earlier study [100], which we now put into a microfluidic context. In this chapter we first discuss the multilayer soft lithographic fabrication of microfluidic chips with integrated elastomeric microlens-based pressure sensors. We then address the performance characteristics of the sensors and finally we demonstrate and discuss applications of multiplexed pressure measurements.

2.1 Fabrication

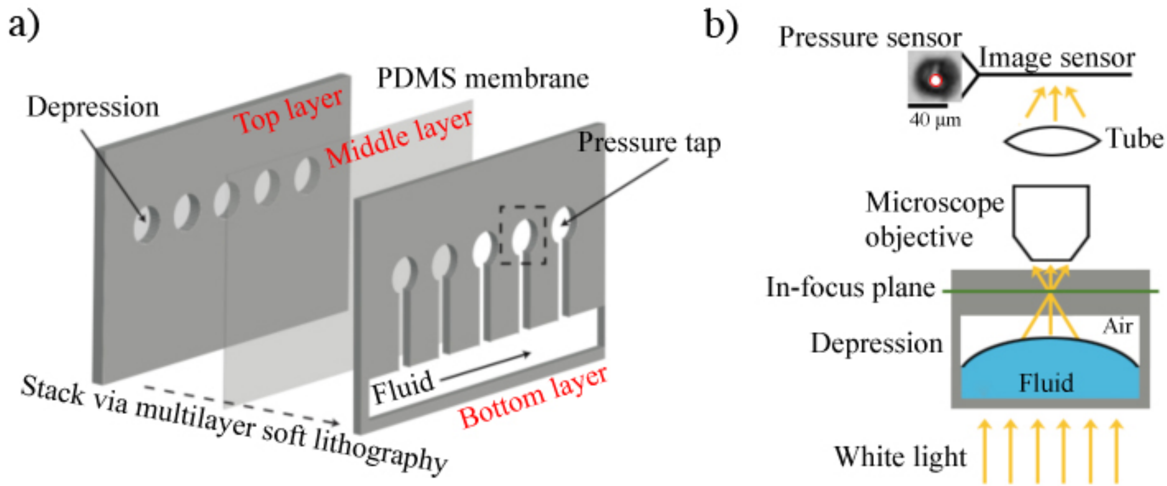

Figure 2-1 a) Schematic of multilayer PDMS device. A thin PDMS membrane is sandwiched between two thick pieces of PDMS that are patterned with features that define the microchannels and sensor regions. b) Experimental geometry showing the pressure sensor in the optical path of a transmission microscope. A micrograph of a typical pressure sensor as seen in an experiment is also shown. The red circle indicates the intensity averaging region.

The elastomer pressure sensors are fabricated using a multilayer soft lithographic technique, similar to that developed by Quake for microfluidic valves [88]. The microfluidic network is designed using a computer aided design program (Archicad 13). A straight microfluidic channel is modified to contain protruding pressure taps, as shown is Figure 2-1a. Each pressure tap ends in a circular dead end that houses the pressure-sensing microlens membrane. An SU-8 master of this design is created on a silicon wafer using standard photolithography techniques. Another SU-8 master is made that consists of only the circular ends of the pressure taps. Finally, a bare silicon wafer and the two SU-8 masters are treated with (tridecafluoro-1,1,2,2-tetrahydrooctyl)-1-trichlorosilane [128]. The bare silicon wafer serves as the spin coating substrate for the microlens membrane. Partially cured PDMS inverse replicas of the two patterned SU-8 masters are made with a 5:1 ratio of PDMS pre-polymer:curing agent by baking for 40 min on a level hotplate at 70°C. A 20:1 mixture of PDMS pre-polymer:curing agent is then diluted 1:3 by volume with hexanes to reduce the viscosity of the PDMS solution for spin coating. This solution is spin coated onto the bare silanized silicon wafer for 150 s at 4750 revolutions per minute (rpm). The spin coated wafer is then baked in an oven for 40 min at 65°C. This recipe yields a PDMS membrane that is 6.5 μm thick. The PDMS membrane is then plasma bonded to the PDMS replica that has isolated circular depressions. Finally, the first PDMS replica is aligned to the membrane-covered PDMS replica with corresponding circular depressions using a photolithography mask aligner. The multilayered device is baked at 65°C for 12 h to complete PDMS curing. The differences in curing agent concentration between the layers results in curing agent diffusion across the layers, ensuring a strong bond between the membrane and the microfluidic network layer. The devices are capable of withstanding pressures in excess of 15 pounds per square inch (PSI).

2.2 Device Calibration

PDMS devices with membrane pressure sensors are placed in a transmission microscope, as shown schematically in Figure 2-1b. A microscope objective lens (4x magnification) is used to image the device onto a CCD camera (Grasshopper, Point Grey Imaging) through a 200 mm focal length tube lens. A variable intensity white light emitting diode (LED) is used for illumination. The calibration procedure is as follows. The device is filled with water and attached at the inlet and outlet to a common air pressure source, whose pressure is controlled *via* a high precision pressure regulator (ControlAir). Air trapped in the dead-end pressure sensing channels is easily forced out of the gas-permeable PDMS. The pressure source is set to the maximum desired pressure. To ensure nearly linear deformation of the membrane, this maximum pressure should not exceed that allowed by the thin plate approximation. The imaging plane of the microscope is then adjusted so that it coincides with the focal plane of the membrane pressure sensors. Each membrane is deformed, thereby acting as a microlens and focusing the light from the LED. Micrographs of the device are obtained from the camera at a set of discrete pressures (typically 25 data points) that are controlled by the pressure regulator. These images are then imported into MATLAB. A feature finding algorithm is used to identify the position of the focal spots in the calibration images [129]. The mean pixel value (hereafter called the average intensity) of the central region of each pressure sensor (red circle in Figure 2-1b) is recorded for each pressure in the calibration sequence. The average intensity *vs.* pressure curves obtained in this way are interpolated using the *spline* function in MATLAB. A typical set of calibration curves for the device in Figure 2-2a is shown in Fig. 2b. The device has a 6.5 μm thick PDMS membrane.

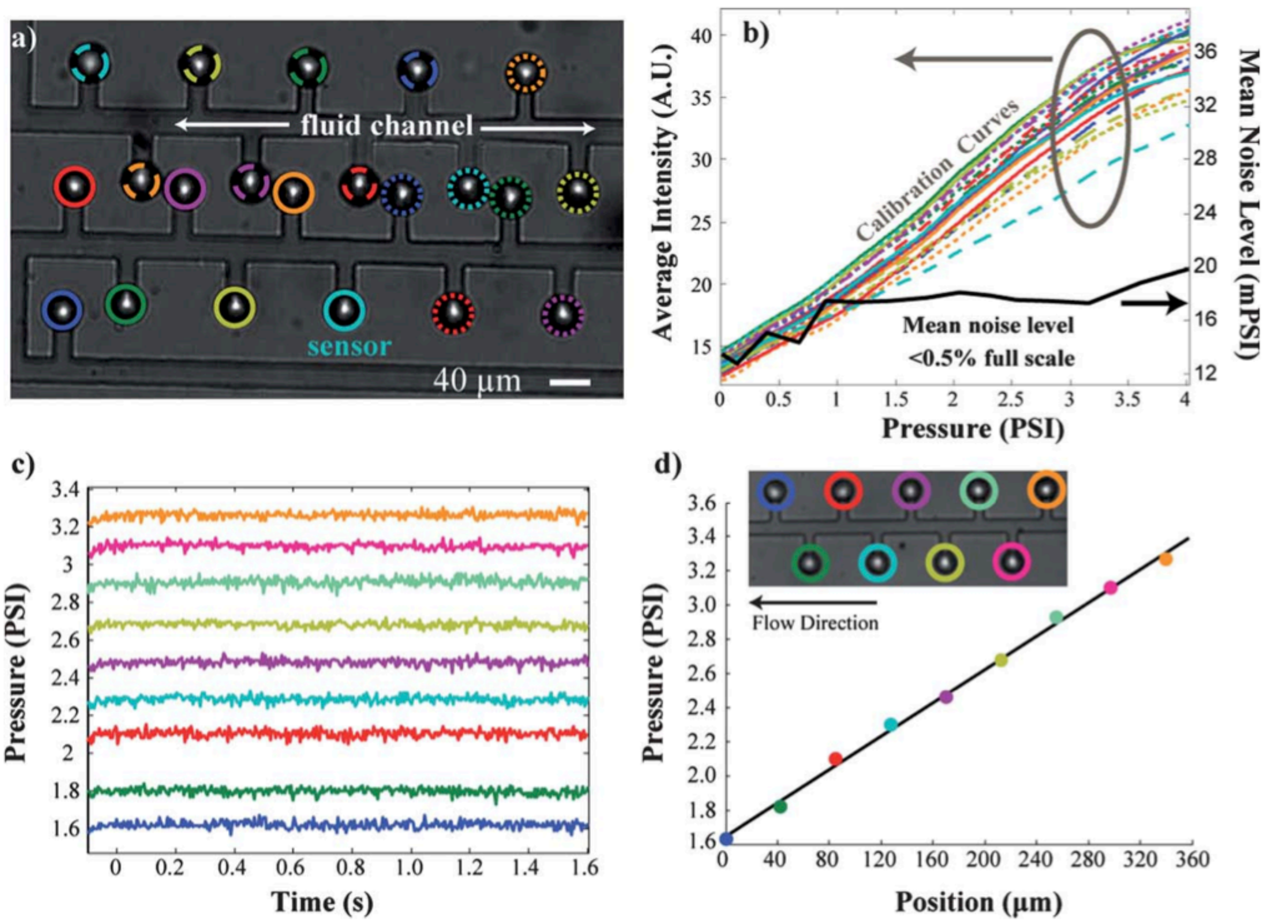

Figure 2-2 a) Micrograph of a pressurized microfluidic channel with integrated pressure sensors. Membrane thickness is 6.5 μm. Micrograph is taken at a small defocus so that the sensors focus light into the microscope's imaging plane. Each sensor's image is circled in a color and motif (solid, dotted and dashed) that corresponds to the calibration curves. b) Intensity *vs.* pressure calibration curves for the 21 encircled sensors of (a). Curves are roughly linear up to 3 PSI and then begin to saturate slightly at higher pressures. Mean noise level averaged over all 21 sensors is plotted *vs.* pressure as a solid black curve. Mean noise level is < 21 mPSI over the entire dynamic range of 4.02 PSI, corresponding to < 0.5% of the dynamic range. c) Pressure *vs.* time measured for pressure sensors formed along straight microchannel in a device with an 8.5 μm thick membrane. Center to center distance between pressure sensors along the direction of flow is 42 μm. d) Pressure *vs.* distance along straight microchannel. Inset: Micrograph of microchannel.

During each experiment, the pressure is deduced from the measured intensity using the calibration curve for that particular membrane. The illumination intensity and shutter speed of the camera are kept constant from calibration to experiment in order to faithfully reproduce the calibration conditions. Fluctuations in light level are compensated for by normalizing the sensor readings to the intensities recorded from inactive regions of the micrograph. We correct for drift of the device, *i.e.* the position of a membrane in the CCD image varies with time, by referencing the position of sensors in the experimental image frames with those in the calibration images. Using miscible fluids with different optical properties can invalidate the calibration because the focusing capability of the pressure sensor is dependent on the refractive index of the fluid. For example, at a given membrane curvature, the focal spot will appear brighter if the refractive index increases because its focal length will be decreased. Additionally, optical absorption can also scale down the brightness of the focal spot, again causing discrepancies between the actual pressure and the calibration curves.

As a canonical test of our sensors, we subject a straight microchannel with constant width and depth to a pressure driven flow by applying a pressure differential across the input and output ports. The pressures at various locations along the channel are recorded (Figure 2-2c) using the previously determined calibration. Because fluid does not flow into the dead end pressure sensors in a steady-state main channel flow, we do not expect that the pressure sensors alter the hydraulic resistance of the microchannel. As expected for laminar flows, we observe a linear drop in pressure along the direction of flow (Figure 2-2d).

2.3 Characterization

2.3.1 Stability and Sensitivity

The sensitivity of the sensor decreases slowly with increasing pressure owing to the sub-linear dependence of the intensity on pressure at the top of the dynamic range, as shown in Fig. 2b. The standard deviation of static pressure measurements (averaged over all sensors in the device) is less than 0.021 PSI over the entire pressure range. This corresponds to <0.5% of the full scale value of 4.02 PSI. These data are obtained at 132 frames per second (fps) with a shutter speed of 1 ms. Since the background noise is white, one may increase the sensitivity with square root dependence on averaging time. The sensitivity can also be increased significantly (albeit at the expense of a smaller dynamic range) by decreasing the thickness of the membrane. For example, a membrane with a thickness of 2.5 μm yielded pressure sensors with standard deviations (averaged over the device) of under 10 mPSI throughout its entire dynamic range of 2.00 PSI.

We find the stability of pressure measurements for a device with a dynamic range of 4.02 PSI to be ± 0.02 PSI over a period of 20 min. This is attributable to the stability of the pressure regulator itself, as monitored *via* the pressure gauge. Additionally, the repeatability of the sensor is limited by the accuracy of the pressure gauge used for calibration, quoted by the manufacturer to be 1%. We note no discernable repeatability or stability issues from the membrane sensor itself for time scales up to 20 min. At longer time scales, we expect the stability to be limited by sample drift in the FOV of the microscope. However, this should be correctable by de-drifting algorithms [129].

2.3.2 Time Response

We investigate the time response of the pressure sensors using a method that takes advantage of their geometry. Our goal is to measure the response time of a single pressure sensor.

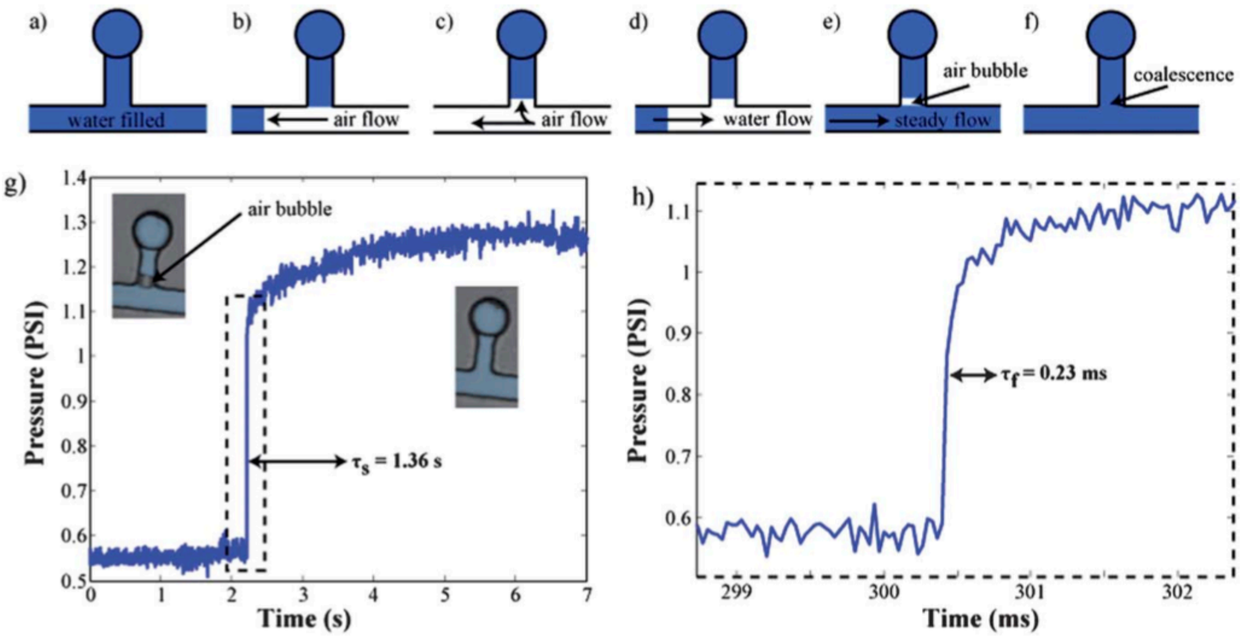

Figure 2-3 a)–f) Sketch of the steps involved in the time response experiment. See text for detailed explanation. g) Pressure sensor response to step stimulus, imaged at 202 fps. The relaxation of the sensor amplitude occurs on a time scale $\tau_s = 1.36$ s. Inset: Micrographs depicting fluid and air geometry before (left) and after (right) coalescence. Pale blue false color indicates water filled regions. h) Pressure sensor response to step stimulus, recorded at 30k fps. The fast component of the sensor relaxation occurs on a time scale $\tau_f = 0.23$ s.

However, temporal characterization of the sensors is challenging because of the parasitic hydraulic resistance and compliance of the entire device. In order to isolate the response of a single pressure sensor, we perform the following experiment. First, the device is filled with water through the inlet (Figure 2-3a). The water is subsequently displaced by injecting air into the device through the outlet (Figure 2-3b). During this displacement, water not only retreats back up the main microchannel but also shears off water that is trapped in the pressure tap. After shearing, the air flow is kept on for 5 s to force the trapped water a small distance down the pressure tap (Figure 2-3c). With the main channel now completely air-filled, water is re-introduced into the device through the inlet (Figure 2-3d). Because the trapped water interface is located down the pressure sensing channel, an air bubble in the pressure tap separates the water trapped in the pressure tap from the water in the main channel (Figure 2-3e). A steady flow is established in the main channel, forcing the air bubble in the pressure tap slowly into the air-permeable PDMS. When the water in the pressure tap and in the main channel coalesce, the pressure sensor records a step increase in pressure, localized to the pressure sensor itself (Figure 2-3f). We record the response of the pressure sensor with a high speed camera (Phantom v7.3) operating at 30k fps.

Figure 2-3g and Figure 2-3h shows the step response of an isolated pressure sensor with a 6.5 μm thick membrane; two time scales are apparent. The first time scale, which is significantly faster, relates to the time required for fluid to fill the extra volume vacated by the deflection of the membrane. In an idealized system, a fluid reservoir fills in a time scale $\tau = \mathrm{RC}$, where R and C are the hydraulic resistance and capacitance of the pressure sensing structure, respectively [103]. The membrane incurs hydraulic capacitance as well as the entire channel leading to the membrane reservoir. The latter is responsible for the hydraulic resistance.

We hypothesize that the second time scale involved arises from the fact that PDMS is air permeable. When the pressure sensing membrane is deflected due to a change in fluid pressure, the volume of the region bounded by the membrane and the PDMS depression changes. The pressure in this air cavity region therefore will deviate from atmosphere. The air cavity pressure slowly equalizes to atmosphere *via* air exchange through the gas permeable PDMS. As a result the membrane deflects further in the same direction as the initial response, but on a slower time scale.

To quantify these time scales, we consider both the rise time of the sensor response as well as the behavior of its time derivative. The latter is particularly useful as it makes use of the fact that the two time scales take very different values in order to extract information on the faster time scale. We define τ_f as the time at which the time derivative of the sensor response decreases to 10% of its peak value. We define τ_s as the time at which the sensor response rises to 90% of its maximum value. We find that $\tau_f = 0.23$ ms and $\tau_s = 1.36$ s for a sensor with a membrane thickness of 6.5 μm. Because we expect the short time behavior to be dominated by the fast time scale, we compare it to the fluid reservoir model discussed above. Tabulated results for the hydraulic capacitance and resistance of the geometries involved are used to calculate the theoretical RC constant [101], [102]. We obtain an RC time constant $\tau = 0.13$ ms for a sensor with a tap length, width and depth of 90, 10 and 10 μm, respectively, along with a PDMS membrane thickness of 6.5 μm, diameter of 40 μm and a Young's modulus of 700 kPa. The time derivative of an exponentially decaying function with time constant $\tau = 0.13$ ms falls to 10% of its peak value in 0.30 ms. This is in reasonable agreement with $\tau_f = 0.23$ ms measured experimentally. Deviations are expected due to the cubic and higher order variation of the RC constant with the pressure sensor dimensions. Because the fast and slow time scales differ by more than three orders of magnitude, we anticipate that many applications requiring fast time resolution are indeed possible with these pressure sensors. We present such an experiment in the following section. Specifically, if the relevant dynamics occur on a time scale much faster than $\tau_s = 1.36$ s, then there will be negligible contribution to the sensor response from the mechanism described above, since there will be little permeation of air through the PDMS during the time interval of these dynamics. Provided that the dynamics are also slower than $\tau_f = 0.23$ ms, the sensor response will represent the true pressure, though differing by an approximately constant scale factor unless the calibration procedure is modified so that it is performed in a time-resolved manner.

2.4 Applications

2.4.1 In-vitro Microcirculation Pressure Dynamics

To demonstrate a potential application of high-speed pressure sensing, we fabricate a microfluidic device consisting of parallel channels each having 5 μm constrictions. On either side of the constriction, a pressure sensor monitors the local fluid pressure. For this device, the membrane is 3 μm thick and 15 μm in radius. Chicken red blood cells (RBCs, Innovative Research, used as received) are flowed through the constrictions by pressure driven flow. When a RBC occupies the constriction, it increases the hydraulic resistance across the constriction leading to an increase in the pressure drop. This phenomenon was used by Abrikan *et al.* to study the stiffness of human RBCs when subjected to a stiffening agent (glutaraldehyde) [8]. Because this technique compares the relative magnitude in pressure dips that occur on a time scale of tens of milliseconds, we anticipate that there is negligible contribution to the sensor signal from the slow portion of the pressure response of Figure 2-3. A typical pressure trace obtained by our device is shown in Figure 2-4. When no cells are present in the constriction, there is a pressure drop of 0.12 PSI across the two sensors. Simultaneous increase and decrease of pressure readings up- and downstream of the constriction are clearly resolvable and occur coincident with the presence of two or more chicken RBCs in the constriction at once. We expect that with higher resolution photolithography transparency masks for better fabrication of small channels and careful design of the sensor parameters, it should be possible to observe the passage of a single chicken RBC. Pressure variations on the order of 0.1 PSI and above have been reported for human RBCs travelling through similar constrictions [8]; this pressure resolution is already achievable with the current design. Because a low magnification microscope objective is employed, it is possible to fit many of these constrictions within one FOV, opening the door to high throughput cell mechanics measurements. Given the sub-millisecond fast component of the time response, we posit a top operating speed on the order of 100 cells per second for each constriction should be achievable. We expect that the high sensitivity and multiplexing ability of these pressure sensors will enable them to find applications in *in vitro* microcirculation diagnostics and the basic science of cell mechanics.

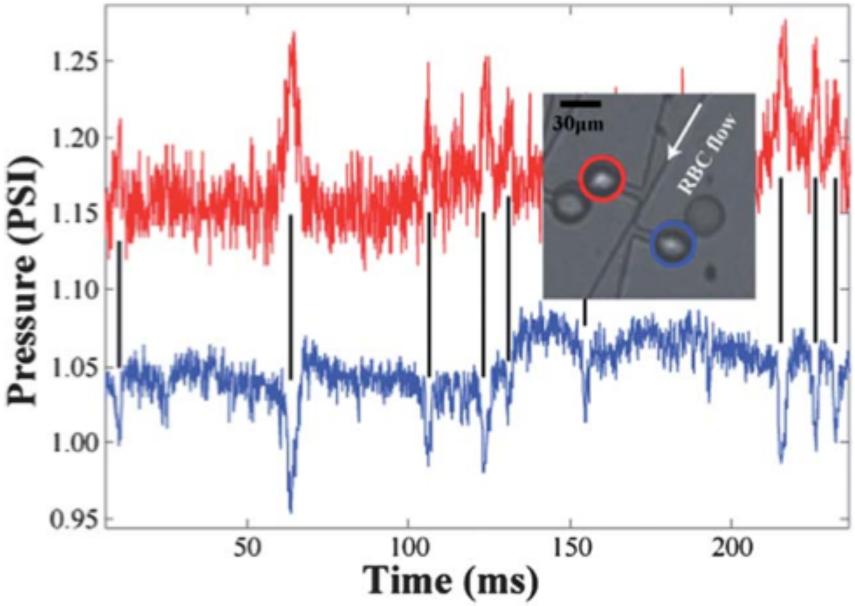

Figure 2-4 Pressure traces of two sensors on either end of a 5 μm constriction. Chicken RBCs flow through the constriction, incurring increased pressure differential between the sensors. The pressure peaks and troughs are marked by black lines. These resolvable pressure jumps are caused by two or more RBCs squeezing through the constriction simultaneously. Inset: Micrograph of device, obtained with 4x objective lens. Membrane radius is 15 μm and thickness is 3 μm.

2.4.2 Two-dimensional Pressure Mapping

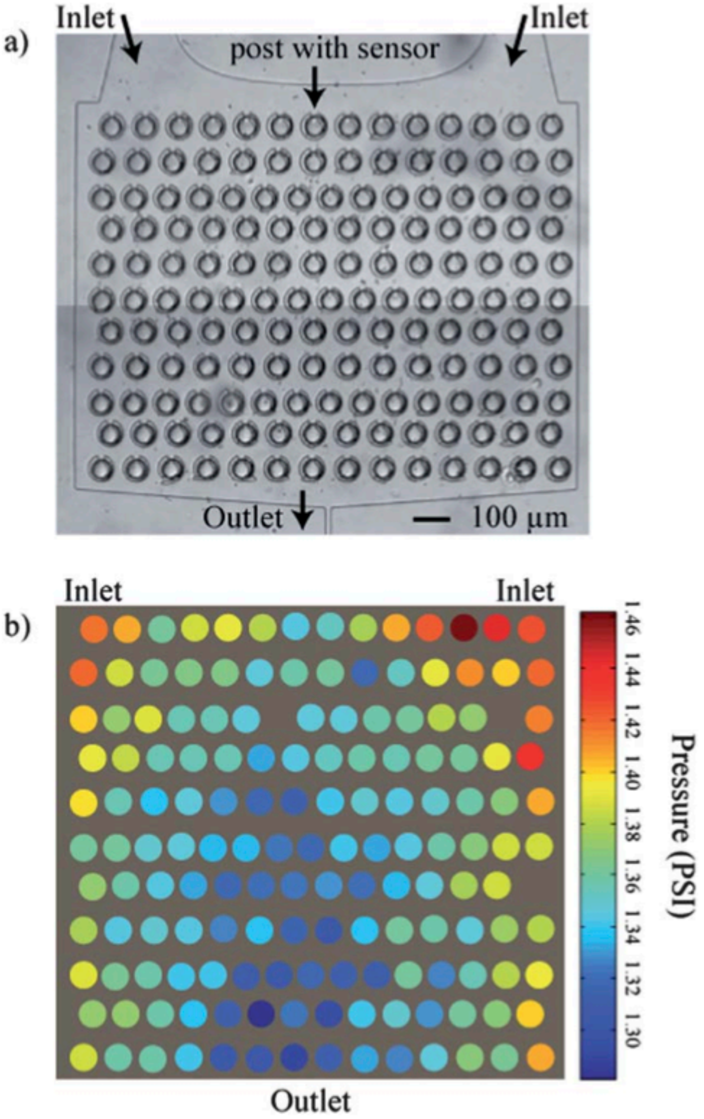

Figure 2-5 a) Micrograph of a porous Hele-Shaw cell fabricated in PDMS. A slightly disordered array of horseshoe-shaped posts form a 2-D field of obstructions. Each post contains a membrane sensor that samples the local fluid pressure. b) The local fluid pressure under steady flow is color-coded from red (high pressure) to blue (low pressure). The pressure map shows high pressure at both inlets, and low pressure towards the bottom and middle of the cell near the outlet. Missing pressure spots from (b) correspond to sensors that were not recognized by the feature finding algorithm.

Two-dimensional mapping of flow is also possible with these sensors. Figure 2-5 depicts a field of pressure sensors, each consisting of a partially enclosed PDMS post, inside a Hele-Shaw cell. Each post incorporates the membrane and functions as a pressure sensor. The cell dimensions are 1.4 mm × 1.1 mm × 10 μm. The posts both enable pressure measurements to be made, and serve to add an element of disorder to the flow environment in order to mimic a porous medium. This is similar to the environment encountered in oil-saturated rock, and we anticipate our device may find application in understanding the behavior of complex fluids in oil-saturated rock. The pressure throughout the cell is mapped at discrete locations. From Figure 2-5 it is clear that the pressure is highest at the top corners near the inlets and lowest near the outlet at the middle of the bottom of the cell as one would expect for a laminar flow [103].

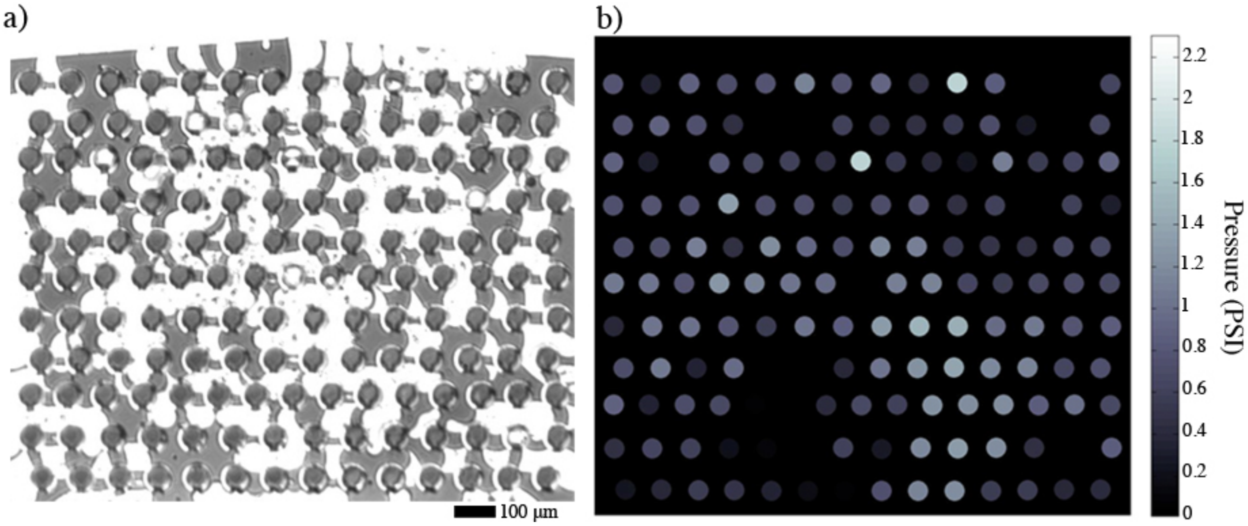

Figure 2-6 a) Micrograph of Hele-Shaw cell filled with blue-dyed water and air. Both air and blue-dyed water are forced through the top inlet (the outlet in Figure 2-5). Air appears white and blue-dyed water appears dark grey. A handful of pressure sensors are not filled with water and thus do not report a pressure reading. b) Pressure map of the Hele-Shaw cell, measured at each pressure sensing post. Movie 2-1 shows the pressure development inside the Hele-Shaw cell at 30 fps, alongside the raw microscope movie.

We used the same Hele-Shaw cell to demonstrate multiphase flow dynamics. The microfluidic Hele-Shaw cell was flooded with a water/blue food dye mixture (phase 1), with each circular pressure-sensing region being filled with blue dyed water. Calibration curves were then obtained for each pressure sensor with the microfluidic chip. Next, pressurized air (phase 2) was forced through the system, removing the majority of the dyed water from the Hele-Shaw cell. Water in the pressure-sensing regions generally stayed put due to favorable surface interactions between water and PDMS. Finally, a combination of dyed water and air was forced through the outlet through the outlet leading to a complex dual-phase flow. Video is recorded at 30 fps, and the pressure map for each video frame is extracted using the calibration curves. A micrograph from this experiment is shown in Figure 2-6a, and the extracted pressure map in shown in Figure 2-6b. The illumination intensity is increased up so that the air filled regions completely saturate the camera sensor, therefore appearing white. The dyed water absorbs significantly more light than the air filled regions, and therefore appears dark. This allows for easy distinction between air and water phases. Occasionally, pressure sensors become air-filled (appearing white). An air filled pressure sensor does not return a true pressure reading. Completely air-filled pressure sensors are deemed off-scale and are set to black in the pressure map (Figure 2-6b). A movie of the raw microscope video alongside a dynamic pressure map is shown in Movie 2-1. Interesting dynamics such as viscous fingering can be observed [130], [131].

2.5 Conclusions

We have demonstrated a monolithic PDMS chip with compact and integrated membrane pressure sensors, fabricated entirely using soft-lithography. These pressure sensors have good stability, low noise (standard deviation below 0.5% of the dynamic range), and a dynamic range that can vary from 2 PSI up to at least 15 PSI. The sensors are inexpensive to incorporate into microfluidic chips and are easily calibrated and read out, necessitating only a regular transmission microscope for operation. Furthermore, the sensors are readily multiplexed, allowing for many measurements in a FOV with concurrent microscopy of the microfluidic network. We expect that these sensors will find use in various fields within microfluidics from measuring pressure fields in multiphase flows to monitoring the pressure dynamics of *in vitro* microcirculatory devices.

3 High Throughput Microlens Microscopy

Optical microscopy is a workhorse technique in modern biological research [12], [132], [133]. Many areas of inquiry, such as drug discovery, are greatly facilitated by extremely large data sets [17], [133]. These are becoming ever more commonplace, enabled by continual improvements in the cost:performance ratio of computing power and digital storage capacity. These huge datasets often come in the form of large-scale fluorescence micrographs. Commercial units, termed high throughput automated microscopes, are tasked with imaging centimeter-scale cell cultures at micron resolution.

Typically, the cell cultures are grown in an arrayed holder called a microwell plate. A microwell plate is made up of an array of isolated cell culture wells, each typically housing a distinct cell culture. The area of a single well in a 384-wellplate is 11.56 mm^2, giving a total imaging area of 44.4 cm^2 [134]. At a spatial sampling frequency of 0.5 μm/pixel, this corresponds to 17.7 gigapixels (Gpx) per wellplate. Using a five megapixel (Mpx) camera, one could construct such an image from approximately 3500 FOVs. Indeed, today's automated microscopes build up a large image by sequentially imaging and stitching together thousands of FOVs. The serial nature of this approach makes it inherently slow, due to the fact that there is temporal overhead associated with the mechanical scanning process, namely the time needed to move the stage, allow it to settle, and refocus the image. This is discussed in detail in Section 1.2.1. From the point of view of imaging throughput, these steps represent dead time, during which the image sensor remains idle.

There are currently many efforts to push imaging into the gigapixel (Gpx) regime at both larger length scales [135], [136], and in microscopy [137], [138]. In microscopy, large FOV techniques often leverage scanned focal spot arrays to parallelize imaging. These techniques have highly scalable architectures, meaning that they can take advantage of the continual improvements in computer and camera technologies that are currently taking place in order to increase imaging throughput.

In this chapter we introduce a novel high throughput fluorescence microscopy architecture. The development of this technique takes place in three stages with each generation gaining more functionality. The general approach is similar to a spinning disk confocal microscope or a multi foci multiphoton microscope: A microlens array is employed to create an array of focal spots that are raster scanned over the sample. Our approach differs from these established techniques in that the microlens array directly focuses excitation light onto the sample with no reimaging optics such as a microscope objective. This allows the focal spot array to be spread out over a larger area, relaxing the reliance on long range mechanical scanning.

The first prototype system, detailed in Section 3.1 represents a proof-of-concept. We show that fluorescent objects can be imaged directly with a scanning microlens array, and discuss the various properties of the imaging system. The second generation microscope, discussed in Section 3.2, uses an immersion fluid to extend the working distance of the microlens array in order to image through coverslips. The pixel throughput is also vastly improved over the previous generation. In Section 3.3, we showcase the third iteration of the design with multichannel capabilities and improved resolution over the second generation.

The three microscope iterations are detailed in the following subsections. For each generation, the microlens array fabrication is described followed by system characterization and imaging examples.

3.1 First Generation: A Prototype System

The goal of the first generation microlens array microscope is to image fluorescent samples directly with an in-house fabricated microlens array. We first describe the microlens array fabrication process followed by a characterization of the imaging resolution. In Section 3.1.1 we describe the fabrication workflow for the first generation. Modifications to the fabrication procedure in subsequent microscope iterations will be described in Sections 3.2.1 and 3.3.1. The imaging setup and mechanics of the image scanning process are discussed as in Section 3.1.2, followed imaging characterization and results in Sections 3.1.4, 3.1.5 and 3.1.6.

3.1.1 Microlens Array Fabrication

We base our microlens fabrication method on the reflow technique introduced in Section 1.3.1. The detailed process is shown schematically in Figure 3-1. A silicon wafer is spin coated with a positive photoresist (AZ-40XT, Microchemicals GmbH) to a thickness of 5 μm. The photoresist is baked at 125°C for 5 minutes on a hotplate and then left to cool to room temperature. The wafer is then loaded into a UV flood exposure mask aligner and a laser printed transparency mask is placed on top of the photoresist layer. The transparency mask consists of a 100×100 square grid of 40 μm diameter transparent circles on an otherwise opaque sheet. The pitch of the square grid is 55 μm; the packing density of the circles is limited by the resolution of the laser printing ($\approx 10-15$ μm). The photoresist is exposed to UV illumination through the mask and is subsequently baked on a hotplate at 95°C for 3 minutes. The wafer is cooled and developed in AZ 300 MIF to reveal 5 μm tall cylindrical posts 40 μm in diameter. The wafer is placed on a hotplate at 125°C for 1 minute, then removed and let cool to room temperature. The heating melts the photoresist, taking on a smooth curved surface. After melting, each cylinder has been melted into a droplet shape, 15 μm tall and 37 μm wide at its base. This defines the lens array master.

In order to produce a replica mold, we first fabricate a flexible inverse mold from PDMS. PDMS precursor and curing agent are mixed together at a 10:1 ratio and then degassed. The resulting liquid mixture is poured over the master mold and cured in an oven at 125°C for 3 hours. The PDMS covered master is removed from the oven and the PDMS is subsequently cut and peeled off of the master, yielding an inverse mold. Finally, photoresist master is replicated in a polymer (Norland Optical Adhesive NOA 61, n = 1.56) on a microscope slide using the inverse PDMS mold as a stamp. The resultant polymer refractive microlens array contains 10,000 elements, and is used for imaging experiments that we describe in the remainder of this chapter.

Figure 3-1 Microlens array fabrication schematic. M1-M5 Denote the “master” fabrication process. M1: Photoresist is deposited onto a silicon wafer and spin coated. M2: The photoresist is baked. M3: The photoresist is exposed to pattered UV illumination consisting of an array of circular holes with no UV irradiation. M4: The exposed resist is developed. The regions of unexposed resist define an array of cylindrical posts remain on the wafer. M5: The wafer is placed on a hotplate at $125^{o}\mathrm{C}$ to melt (reflow) the photoresist into smooth droplets. The wafer is let to cool to room temperature, and the curved resist droplets harden. S1 and S2 are the stamp fabrication process steps. S1: Liquid PDMS is poured onto the microlens array master. S2: PDMS is heat-cured and peeled off the master, leaving a negative copy of the master. R1-R3 details the fabrication of the replica microlens array. R1: Norland Optical Adhesive 61 (NOA) is dispensed and spin-coated onto a glass slide. R2: The PDMS stamp is placed face down onto the liquid NOA. The NOA is flood illuminated with UV radiation. R3: The PDMS stamp is peeled off of the UV cured NOA, leaving a positive replica of the master in NOA on the glass substrate. The PDMS stamp can be reused to fabricate more microlens array replicas. Each material is identified by a unique color as per the legend at the bottom.

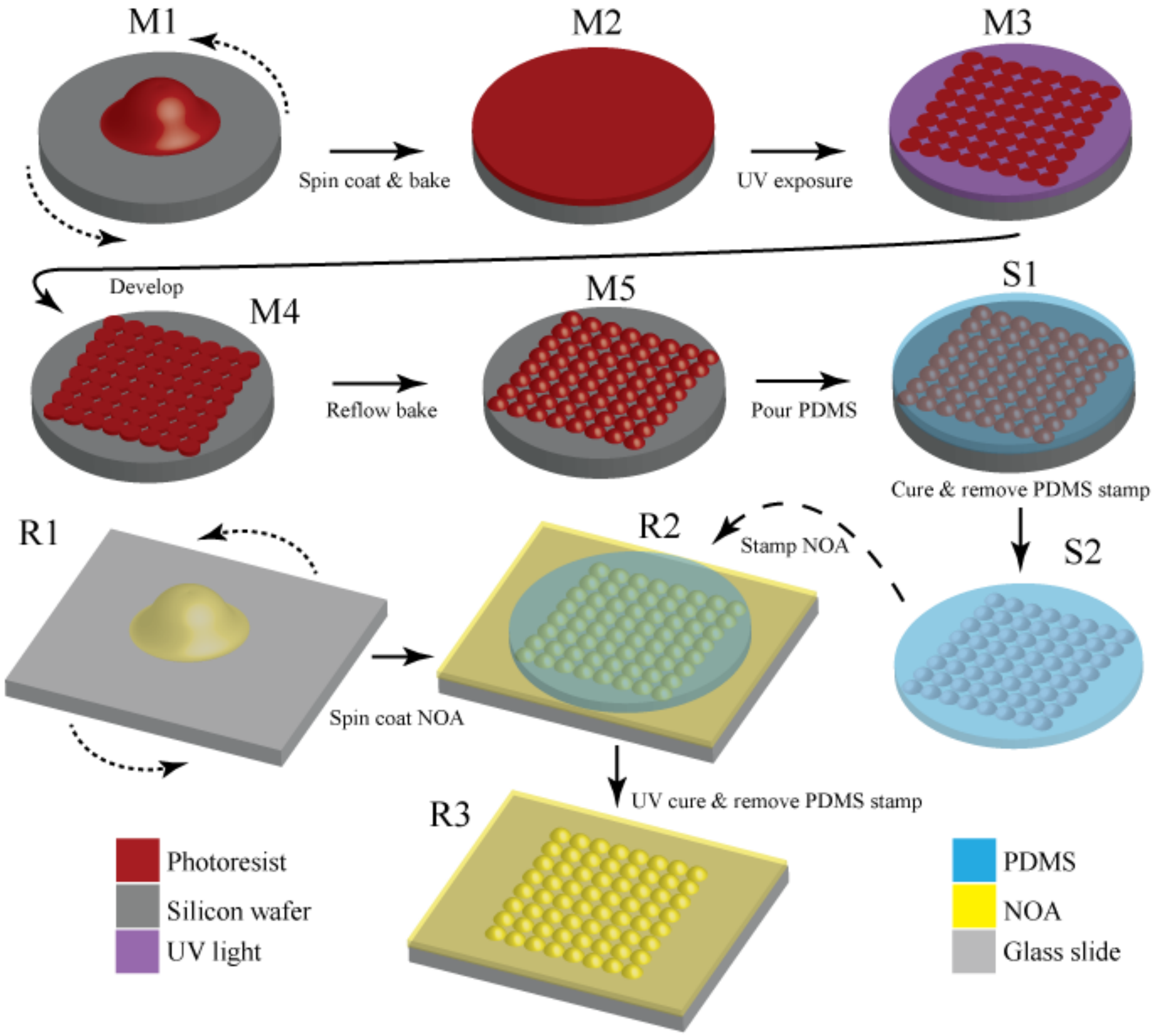

Figure 3-1 (Continued)

3.1.2 Optical Setup

We use a parallelized epifluorescent geometry to both illuminate and detect fluorescence from the sample. A refractive microlens array is illuminated with a collimated laser beam with a wavelength of λ = 532nm and an output power of 38 mW. This creates an array of focal spots on the sample as shown in Figure 3-2a.

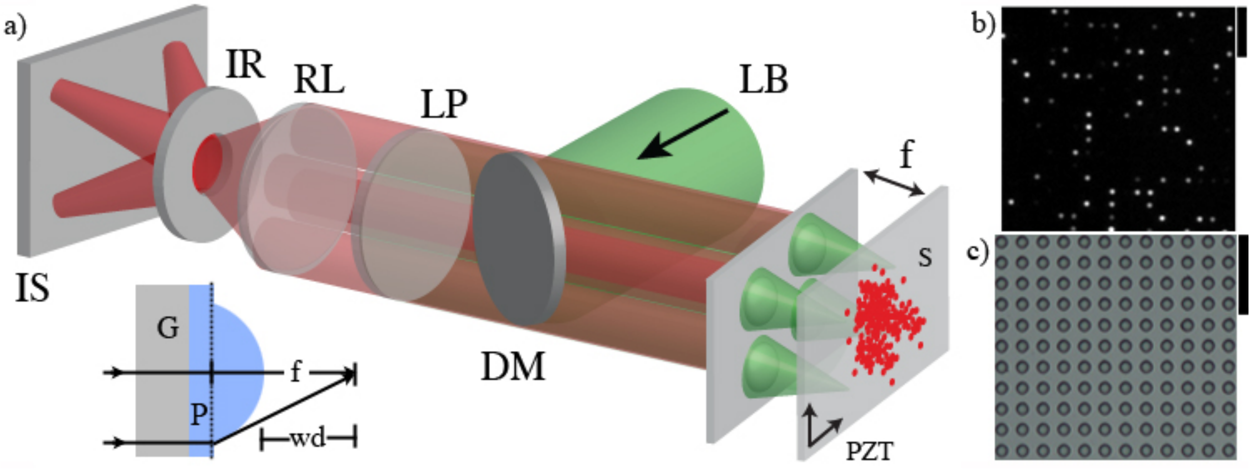

Figure 3-2 (a) LB: Laser Beam; DM: Dichroic Mirror; MLA: Microlens Array; Microlens array focal length f = 40.6 μm; S: Sample; PZT: Axes along which the sample is piezo scanned; LP: Long-pass Filter; RL: Relay Lens; IR: Iris; IS: Image Sensor. Inset: Schematic of a microlens, showing a central and marginal ray to define the focal length (f) and working distance (wd). G: Glass Slide; P: NOA 61 Polymer. (b) Representative raw data frame captured by the image sensor. Scale bar is 200 μm. (c) Bright-field micrograph of microlens array. Scale bar is 200 μm.

The sample is placed one focal length from the microlens array. The microlens array consists of a grid of 100x100 plano-convex refractive lenslets, oriented with their curved surfaces facing the sample. The working distance of the array is 26 μm, with an NA (numerical aperture) of 0.41. Fluorescence excited by each microlens focal spot at the sample is collected by the same microlens, and proceeds as an approximately collimated beam to a 100 mm relay lens [139]. The relay lens projects an image of the microlens array apertures onto a charge-coupled device (CCD) digital camera (Point Grey Grasshopper or Phantom V7) at unity magnification (Figure 3-2b) through a long pass filter (λ > 575 nm). A variable diameter iris is placed in the back focal plane of the relay lens, which is itself conjugate to the sample plane for each microlens. The iris acts as a confocal spatial filter for each microlens in the array [140].

The image of the microlens array recorded on the CCD appears as an array of bright circles (Figure 3-2b), with each circle representing the fluorescence relayed by a particular microlens. Each microlens acts as a point scanning confocal microscope, with its signal read out by the appropriate CCD pixels. To construct an image, the sample is raster scanned in two dimensions using a piezo stage (Thorlabs). Ideally, the scan region would be equivalent to the microlens pitch (55 μm × 55 μm). The piezo stage used, however, has a maximum travel of 20 μm × 20 μm. We therefore perform a 4 × 4 mosaic of scans to cover the microlens unit cell. A 4 × 4 mosaic, as opposed to a 3 × 3 mosaic, is needed to provide sufficient overlap between adjacent images to allow image stitching. Because the stage must be manually adjusted between each mosaic tile, we have additional acquisition time overhead over an ideal system with a piezo stage with a long enough travel to scan over the entire microlens cell at once. This additional acquisition time overhead will be completely eliminated in future iterations by the use of a longer travel piezo stage. For this reason, we quote our acquisition times as the elapsed time during which the piezo stage is actively scanning, and do not include the time for manual adjustment of the stage between tiles.

After scanning, images are constructed by plotting the fluorescent emission signal as a function of stage position. The fluorescent emission signal is found by summing the pixel values associated with each microlens (bright circles of Figure 3-2b). For the images we present in this paper, camera frame rates of 202 or 404 frames per second (fps) are used. The number of frames acquired per line of the raster scan is 130. The line scan time is set to an integral number of camera frames to avoid image shearing.

3.1.3 Microlens Array Characterization

We characterize the focal spots created by the microlens array by illuminating the array with a collimated laser beam (wavelength $\lambda = 532\ \mathrm{nm}$). The microlens array as fabricated on a microscope slide reflects ~6% of the incident laser illumination, attributable to Fresnel reflections at the air/glass and air/polymer interfaces. The focal spot array is imaged onto a CCD camera using a 100x 0.8NA objective lens. The focal lengths of individual microlenses, as defined in Figure 3-2a are obtained as follows. The microlens array is attached to a mechanical translation stage equipped with a manually-actuated micrometer. The stage position is adjusted so that the region where the curved microlens surface becomes flat (microlens periphery) is in focus on the CCD (Figure 3-2a inset). The stage position for which the microlens focal spot on the CCD camera takes maximum intensity is then found. The focal length is the distance between these stage positions. The focal length is the sum of the working distance and the lens thickness (15 μm). This process is repeated for 10 microlenses in the array. The focal lengths are measured to be 40.6 μm +/− 0.9 μm across the array; the error represents one standard deviation from the mean. The array therefore has a working distance of roughly 26 μm from the summit of the microlens to the sample. A typical focal spot created by a microlens is shown as Figure 3-3.

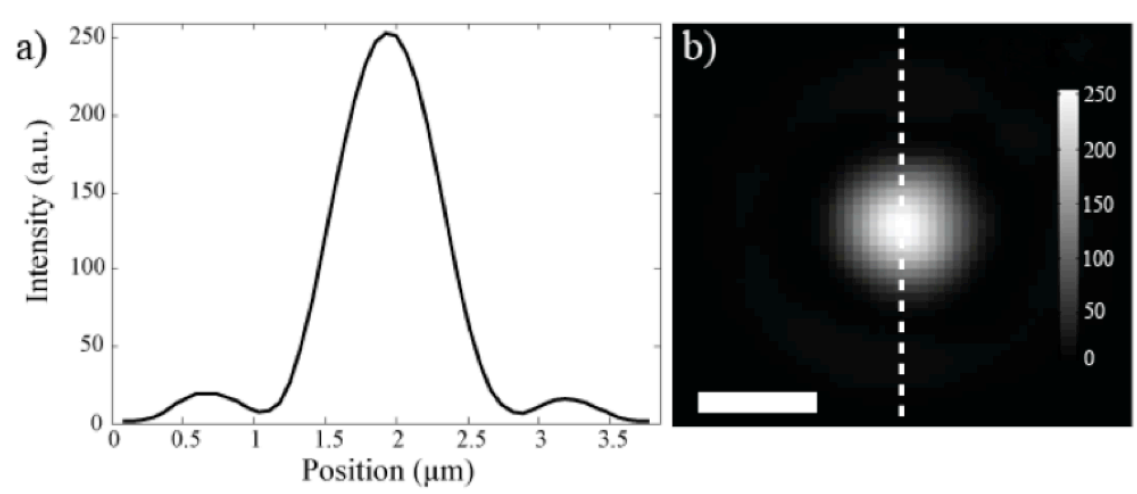

Figure 3-3 (a) Line-cut of focal spot intensity. (b) Intensity distribution of a microlens focal spot. Dotted white line indicates line along which 1D intensity is plotted in panel (a). Scale bar: $1\mu m$.

The focal spot images are deconvolved using the DeconvolutionLab plugin for ImageJ [141]. This procedure results in the full width at half maximum (FWHM) of the laser illumination focal spots being determined to be 781 nm +/− 15 nm, which is larger than the FWHM = 649 nm expected with a diffraction-limited 0.41 NA lens at 532 nm. The discrepancy is due to spherical aberration incurred reflow lens profile [142]. We perform further characterization by imaging small (200 nm diameter) fluorescent spheres. This is described in the following section.

3.1.4 Imaging Resolution

Samples consisting of fluorescent microspheres (Invitrogen) dried onto a microscope slide are imaged by raster scanning them under the focal spot array with a piezoelectric scanning stage. As described above, for each stage position, the CCD image sensor is read out (Figure 3-2b). The signal from each microlens is integrated by summing the intensities of the pixels that comprise it. The image of the sample is then constructed by plotting the signal as a function of stage position. A typical result is shown as Figure 3-4.

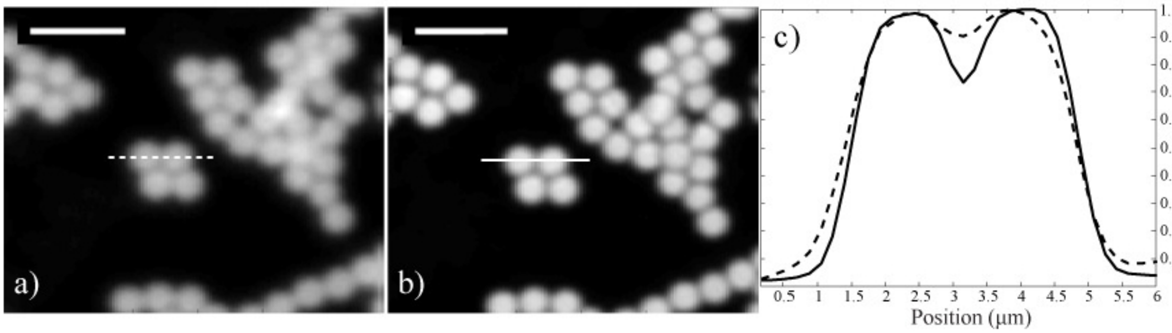

Figure 3-4 (a) Image of 2 μm beads obtained with iris fully open. (b) Image of 2 μm beads with iris diameter 2 mm. Scale bar is 5 μm. (c) Line cut of intensity through a pair of neighboring beads, dotted curve: open iris, solid curve: 2 mm wide iris.

The sample consists of fluorescent spheres with diameters of 2 μm. Figure 3-4 illustrates the effect of iris width on the image characteristics. The image taken with the iris open (Figure 3-4a) is blurred compared with an image taken with a 2 mm iris width (Figure 3-4b). This sharpening is evident in the line-cuts of Figure 3-4a and Figure 3-4b that are shown in Figure 3-4c. The improved image quality is a result of confocal filtering. Overlapping images of each microlens FOV occur at the iris plane. For each microlens, the Airy disk diameter at the iris plane is $A_d = \frac{2.44\lambda_{em} f_r}{d} = 3.8$ mm, where λ_{em} is the fluorescence emission wavelength (575 nm), f_r is the focal length of the relay lens (100 mm) and d is the microlens diameter (37 μm) [140], [143]. An iris with a diameter of 2 mm therefore functions as a confocal pinhole with a width of 0.52 of the Airy disk. To compare the results to what one would expect from the experiments of Figure 3-3, we perform the following analysis. We take the measured focal spots (Figure 3-3), then construct a confocal PSF, given a 2 mm diameter iris [144]. These PSFs are convolved with two 2 μm spheres separated by a gap of 100 nm to produce simulated images. The spheres are modeled as circles with a fluorophore density proportional to the sphere thickness at each point.

These simulated images have a trough to peak ratio of 0.07 ± 0.04 for an open iris and 0.23 ± 0.04 for a 2 mm ± 0.25 mm diameter iris. The uncertainty indicates the standard deviation over all 10 measured PSFs. Within the variability of the PSFs, this trough to peak ratio is in agreement with the values from Figure 3-4c of 0.08 and 0.27 for an open iris and 2 mm diameter iris, respectively.

The imaging of small (200 nm diameter) fluorescent beads provides an additional means for determining the system resolution. The fluorescent beads approximate a point object, effectively mapping out the PSF of the imaging system. Isolated fluorescent spheres are identified by a feature finding algorithm [129]. A 2-D Gaussian is fit to each sphere and its FWHM extracted, enabling the resolution of the system to be found. With the iris fully open (no confocal filtering), the beads have a FWHM (± standard deviation) of 787 nm ± 39 nm, in agreement with the excitation focal spot size. With an iris diameter of 4 mm ± 0.25 mm (roughly one Airy disk diameter), the FWHM of the beads drops to 706 nm ± 34 nm. Confocal filtering of the PSF shown in Figure 3-3, with an iris width of 4 mm ± 0.25 mm, is expected to reduce the FWHM to 752 nm ± 18 nm. The observed shrink in the FWHM of the confocal PSF agrees with theoretical expectations, within the error of our measurements.

3.1.5 Imaging Results

A section of Hematoxylin and Eosin (H&E) stained rat femur is imaged using 3210 microlenses at a frame rate of 202 fps. Typically H&E staining is used for analysis with brightfield transmission microscopy. Here, however, we image the eosin dye using our fluorescence system, because it provides a convenient demonstration of fluorescent imaging in biological samples. The raw pixel throughput of the image is therefore 0.6 Mpx/s. Each frame is 304 × 304 pixels, obtained using the region of interest (ROI) function of the Phantom V7 camera employed.

A 4×4 mosaic for each microlens is stitched together using a custom MATLAB script. The offsets between overlapping pairs of images are determined via 2D cross correlation, followed by gain compensation and linear blending [145]. The FOVs from each microlens, i.e. the 4×4 mosaics, is stitched to its neighbors by the same method. The result is shown as Figure 3-5.

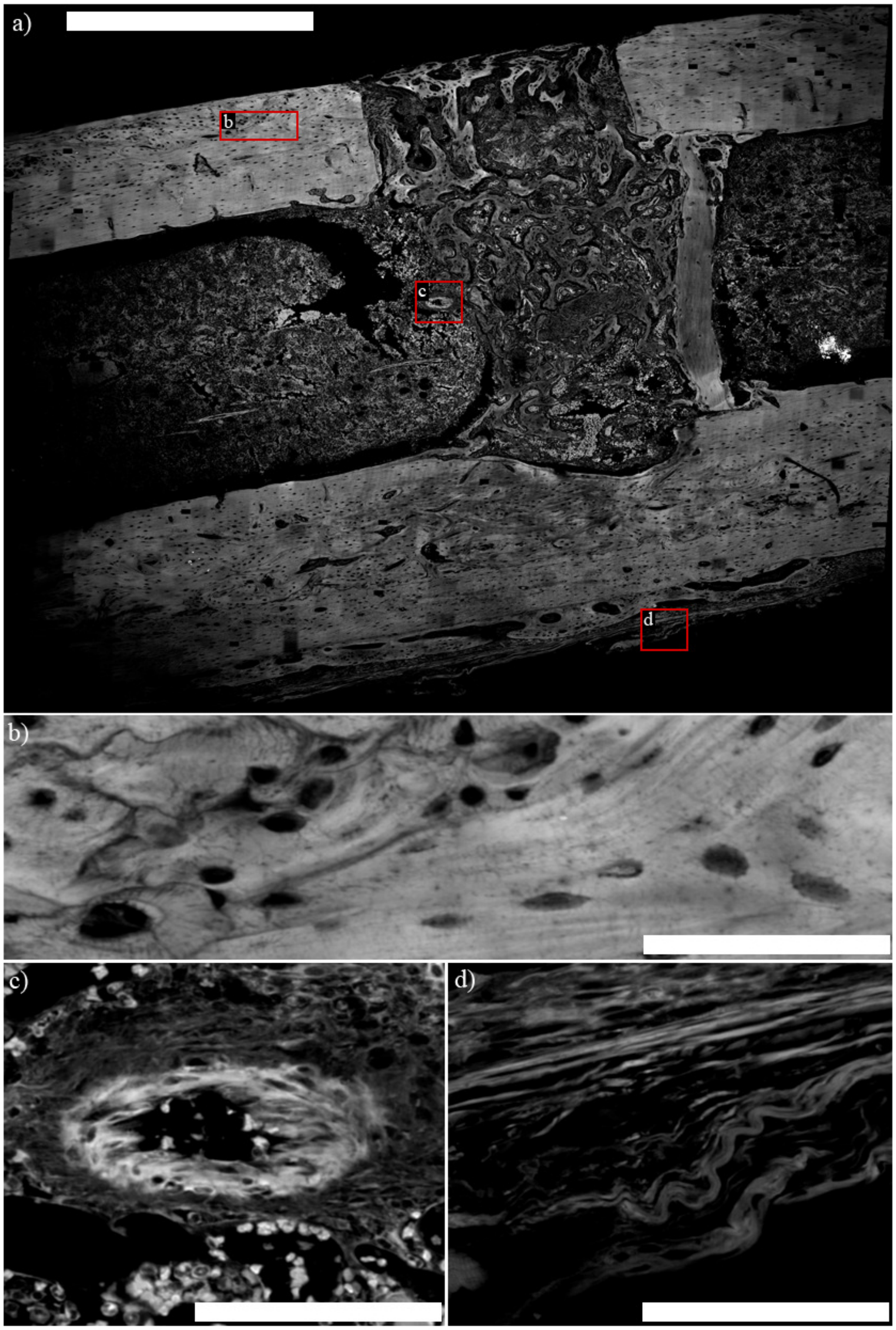

Figure 3-5 (a) Image of H&E stained rat femur. Scale bar is 1 mm. (b) Zoom-in of cortical femoral bone. (c) Inside of the medullary canal of the femoral bone. Blood cells and fibrous structures are visible. (d) Zoom-in of periosteum. Scale bars for (b)-(d) are 80 μm.

Bone, bone marrow, fibrous structures and blood cells can all be seen in the image. The entire image takes 22 minutes of acquisition time, which does not include the time taken for manual stage adjustment between the 4 × 4 tiles or post processing stitching time. The manual stage adjustment overhead will be eliminated in future iterations with a longer travel piezo stage.

There are two ways in which to increase the imaging throughput of our system: using a larger number of microlenses and imaging at a greater frame rate. We achieve a raw pixel throughput of the image of 4 Mpx/s by increasing the camera frame rate to 404 fps and by using all 10,000 microlenses in the array (Figure 3-6).

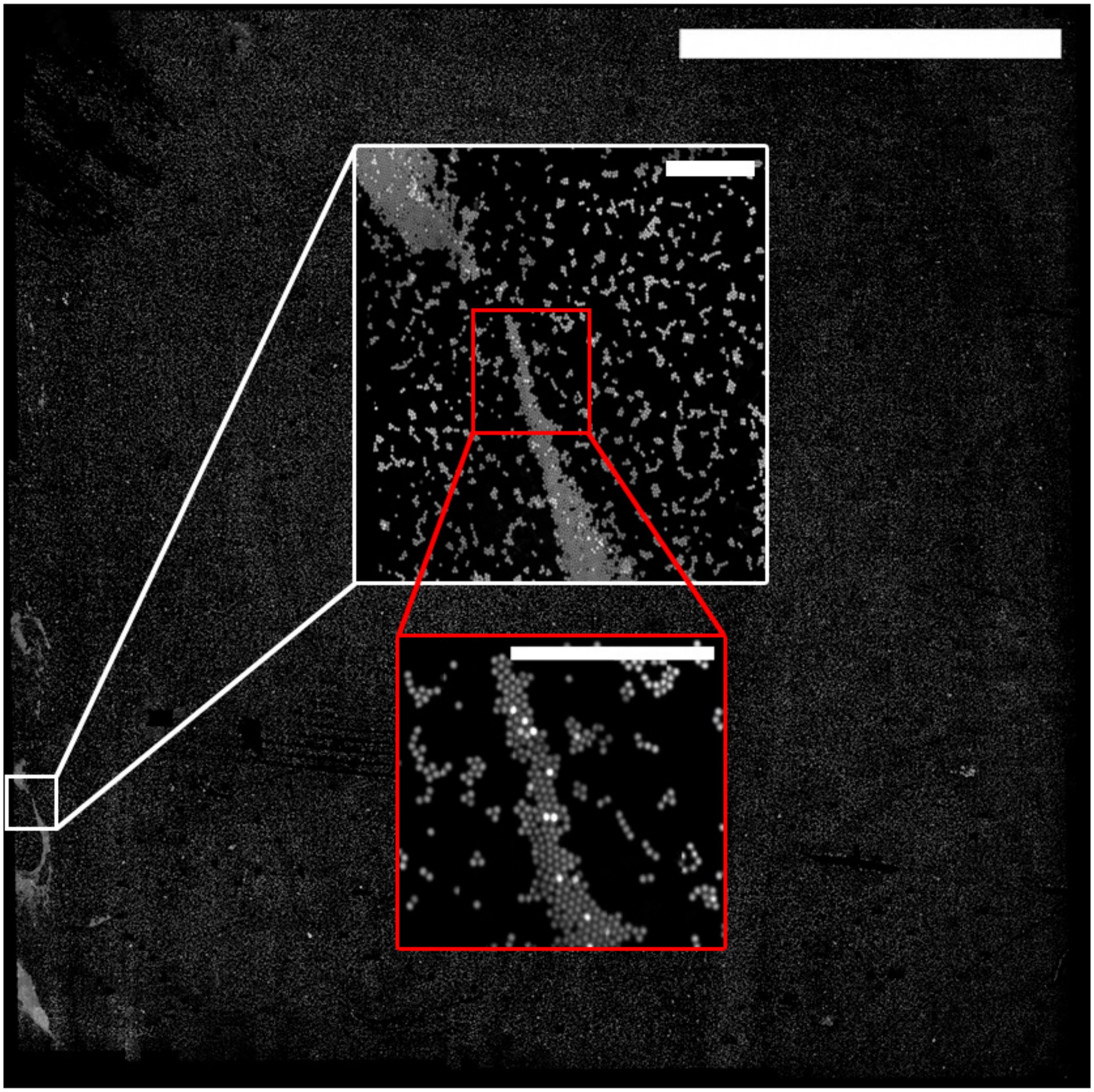

Figure 3-6 A 5.5 mm × 5.5 mm image of 2 μm fluorescent beads. Scale bar is 2 mm. Top inset: Zoom-in of boxed-in region (white border). Scale bar is 50 μm. Bottom inset: Zoom-in of boxed-in region in top inset (red border). Scale bar is 25 μm.

The entire image takes 11 minutes of acquisition time, again leaving out the manual stage adjustment time and stitching time. After stitching, the image size is 0.85 Gpx. The apparent pixel throughput after stitching is less than the raw throughput because of the overlap between tiles. This reduction in apparent throughput will be avoided with a longer travel stage. This raw throughput of 4 Mpx/s is nearly as high as what, at the time of writing, comprises the state-of-the-art, for example the Molecular Devices ImageXpress Micro XLS, which achieves ~4-5 Mpx/s under similar conditions and before stitching is factored in [35].

The sample in Figure 3-6 is larger than the rat femur sample, and consists of fluorescent microspheres with diameters of 2 μm. At this frame rate, the camera (Phantom V7) operates with a frame size of 352×352 pixels. We therefore adjust the magnification of the relay lens system so that the image of the microlens array fits within this frame size. This corresponds to a sampling density of 12 pixels per microlens at the image sensor – a factor of 3 larger than theoretically necessary according to the Nyquist criterion. In future iterations, we expect to use the full frame of Mpx-sized camera sensors, as opposed to the 0.124 Mpx ROI used here, in order to increase the pixel throughput.

3.1.6 Scanning Light Field Imaging

A ray optics picture of the experimental setup is depicted in Figure 3-7a and Figure 3-7b. Because imaging is performed by a point scanning procedure, all rays emanate from a pseudo point source on the sample. Therefore, the position at which a ray hits the microlens aperture corresponds directly to the direction in which the ray emanated from the sample. Knowledge of both the initial position (u, v) of the ray in the sample plane and its point of intersection with another plane (s, t) parallel to the sample plane, fully parameterizes the ray. The 4-D data set composed of the intensity at each (u, v, s, t) coordinate is called the “light field function” and is denoted by $L(u, v, s, t)$. Light field recording has been previously used in microscopy to obtain perspective views and to perform refocusing [56].

The experimental geometry employed in this work images the irradiance at the microlens aperture. The scan position corresponds to the (u, v) position while the pixel position in the microlens subimage gives the (s, t) coordinate. As a result, the light field function L is obtained in addition to the conventional image. The conventional images (such as those shown in Figure 3-4, Figure 3-5 and Figure 3-6) are obtained by integrating the irradiance over the entire microlens aperture. This can equally be thought of as an integral over all ray angles impinging on the microlens.

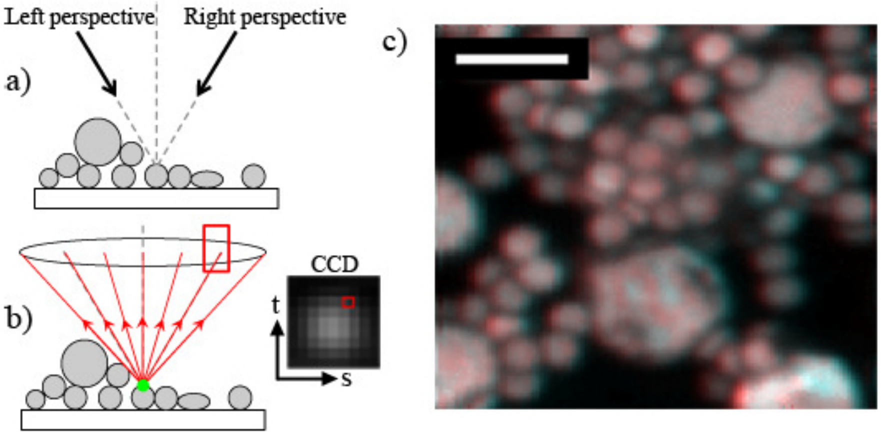

Figure 3-7 a) Left and right perspective views are observations of a scene taken from opposing viewpoints. b) Ray-optics schematic of angular mapping onto image sensor. The angular distribution of rays emitted from within the excitation spot (green region) corresponds to the intensity distribution impinging on the lens aperture and its image at the image sensor. Each pixel on the CCD image of the microlens aperture corresponds to a distinct perspective view. The space occupied by the image of the microlens aperture is described by the coordinates (s, t). c) Red/cyan anaglyph of a pile of 2 μm and 5 μm fluorescent beads, constructed using left and right perspective images shows this sample from multiple perspectives). Scale bar is 5 μm. Movie 3-1 shows the viewpoint of (c) rotating at 12° from the optical axis.

We can digitally filter the irradiance to acquire light field images at specific $(s = s_0, t = t_0)$ planes. This is done by using only the (s_0, t_0) pixel in a microlens subimage to construct the raster scanned image, effectively replacing the detection optics by a pinhole at position (s_0, t_0). Each (s, t) coordinate corresponds to a unique viewpoint. As the viewpoint is changed, beads that are out of the focal plane appear to shift position; this is the basis of depth perception. Figure 3-7 shows an anaglyph of a pile of beads, constructed by overlaying images obtained from two diametrically opposed pixels in the microlens aperture, color coded as red and cyan. The two diametrically opposed pixels lie halfway to the edge of the microlens from its center. The angle between the red and cyan colored images is 24°. The parallax and three-dimensional structure of the sample is particularly evident in Figure 3-7a (Movie 3-1), in which the viewpoint is made to circulate at 12° from the vertical.

The maximum angle of parallax is limited by the collection angle of the microlens. In this work, the microlens NA is 0.41 in air so that the maximum collection angle is 48.4°. The angular resolution is dependent on the iris diameter. The iris acts as a low pass filter for the microlens array image projected onto the camera sensor. As the iris is stopped down, there are fewer resolvable spots within a microlens aperture, and therefore the resolution in the (s, t) plane (equivalently the angular resolution) is degraded. This is analogous to the tradeoff described in [56], where the number of diffraction limited spots impinging on each microlens determines the angular resolution. Here, the number of diffraction limited spots sampled by each microlens is controlled by the iris in the sample's conjugate plane, i.e. the iris effectively controls the FOV of each microlens. Even though only one diffraction limited spot is illuminated in the microlens FOV, the entire spatial bandwidth relayed by the microlens is used for resolution in the (s, t) plane.

3.2 Second Generation: Water Immersion Microlens Microscopy

Here, we demonstrate the imaging of samples loaded into a micro well plate, the first time this has been reported for any parallelized microscopy system, to the best of our knowledge. This is significant because, at the time of writing, micro well plates are used very extensively in high throughput screening labs. Considerable investments have been made in robotic systems with which well plate samples can be handled efficiently. Our approach could therefore employ such systems for sample handling. We also image a tissue microarray and a fluorescently labeled section of mouse kidney, demonstrating the sensitivity and resolution of our system with biologically relevant samples.

The short focal length microlens arrays used in Section 3.1 produced high resolution fluorescence images due to their large numerical aperture (NA) of 0.41. However, the drawback of such a large NA along with a small microlens diameter (37 μm) is that the working distance can be prohibitively short. Typically, fluorescent samples are mounted underneath a cover slip ranging from 100 to 300 μm thick in order to prevent sample movement and degradation. However, the microlens array used in Section 3.1 has a working distance of only 26 μm, thus precluding the possibility of imaging any samples mounted behind even the thinnest cover slip.

In order to demonstrate the applicability of our system with real world samples (that is, samples that are mounted with coverslips), we employ an immersion medium (water, $n_w = 1.33$) between the microlens array and the sample coverslip. The immersion medium's purpose is twofold. First, the immersion fluid reduces the refractive index contrast between the microlens array material and the surrounding medium, thereby increasing the focal length of the microlens array. The increased focal length results in a longer working distance but a small NA and therefore lower resolution. The second convenient property of the immersion fluid is that it increases the NA of the microlens by a factor of n_w. Thus, a water immersion microlens has a diffraction limited resolution n_w times higher than an air immersion microlens with the same focal length.

In the following subsections we detail the immersion microscopy setup and fabrication of the microlens array used therein. We then continue to demonstrate imaging of a large microwell plate sample and a coverslip sealed fluorescent tissue sample.

3.2.1 Microlens Array Fabrication

The microlens array is fabricated via a reflow molding process similar to that of section 3.1.1. A 695 × 695 rectangular array of cylindrical posts is written onto a 100 mm diameter silicon wafer in SPR220-7.0 photoresist using a prototype direct write lithography system (Heidelberg µpg-501).

The direct write lithography system takes a 7-bit greyscale image from the user and reproduces the image on a digital micromirror device (DMD) array. The DMD is illuminated by a UV LED ($\lambda = 395\ nm$), and imaged onto the photoresist by a 20x, 0.75 NA microscope objective. Each DMD pixel maps to a 500 nm square in the projected image. The exposure of the photoresist is proportional to the grey value of the input image. Large area exposures are realized by separating a large input image into smaller image tiles. Each tile is exposed onto the resist sequentially. In between each exposure, the sample is translated by $400\ \mu m$ along each line and by $300\ \mu m$ in the orthogonal direction at the end of each line.

The input image to the direct-write lithography system is a binary image file of circles 188 px in diameter arranged on a square grid with a pitch of 200 px. Inside the circles, the image file takes on a value of 0 (no exposure) whereas the region outside the circles has a grey value of 127 (maximal exposure). When projected onto the photoresist, the circle array has pitch of $100\ \mu m$ and each circle has a diameter of $94\ \mu m$. A total of 40,252 sequential exposures over 5 hours are needed to write the entire 695×695 array onto the resist.

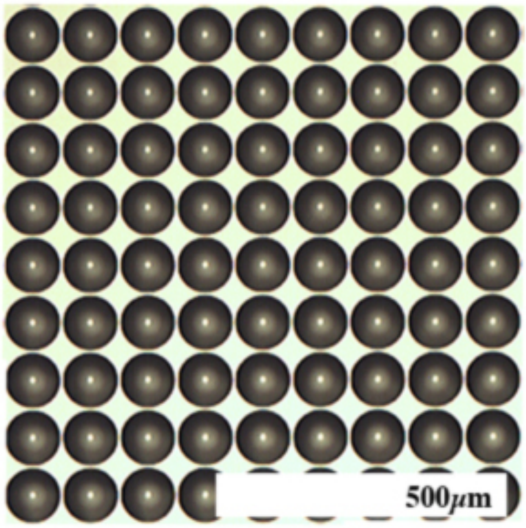

Figure 3-8 Reflection micrograph of a section of the microlens array used in section 3.2.

After development, the wafer is placed on a hotplate at 140°C for 1 minute to melt the photoresist pillars into smooth lenses. The microlens height after melting is $18.3\ \mu m$. A negative of the photoresist master is then replicated in polydimethylsiloxane (PDMS) [12]. Finally, the photoresist template is replicated in a polymer - Norland Optical Adhesive 61 (NOA 61, n=1.56) - on a 50 × 75 mm microscope slide using the inverse PDMS mold as a stamp. The microlens array spans an area of 50 × 69.5 mm and contains ~347,000 elements. A micrograph of a portion of the microlens array is shown in Figure 3-8. The microlens array has a focal length of 141.5 μm in air, and 345 μm in water, the latter yielding a theoretical NA of 0.18.

3.2.2 Optical Setup

The immersion microscopy setup depicted in Figure 3-9 is similar to that of the short focal length system in Figure 3-2, however, an immersion fluid is added and alterations are made in order to increase the FOV and imaging throughput. A green laser beam ($\lambda = 532\ nm$) is sent through a microscope objective (50× and 10× for wellplate and tissue imaging experiments, respectively). The resultant divergent beam is then reflected by a long pass dichroic mirror (cutoff $\lambda = 550\ nm$) and converted into a beam that diverges more weakly by a tube lens (f = 200 mm). The diverging beam is clipped both at the dichroic mirror and at the tube lens aperture, so that only the central portion of the beam illuminates the sample; a small amount of beam divergence is necessary in order to illuminate a sample area larger than the tube lens aperture. The excitation uniformity over a 3.6 × 3.6 cm region of interest (ROI) at the sample when using the 50× objective is 15% (center to edge). A refractive microlens array (pitch 100 μm, f = 345 μm in water) is located at a distance of 200 mm from the tube lens. The microlens array focuses the laser beam into an array of focal spots at the sample plane. The beam divergence must be small enough for the off-axis aberrations experienced by focal spots at the periphery of the ROI to be small. In our case the beam divergence is $<7.5^{o}$, small enough so that off-axis aberrations are insignificant. The microlens array is mounted on a tip/tilt stage (Edmund Optics), enabling it to be adjusted to be parallel to the sample. The sample is placed at the focal spot array plane on a 2-axis closed loop piezoelectric stage (Newport NPXY200SG) that scans the sample over a 110 × 110 μm square at the focal spot array plane. Water is used as an immersion liquid between the lens array and sample in order to increase focal length. It also has the benefit of improving the resolution compared to what would be obtained with a microlens array of the same focal length operating in air. The fluorescence excited at each focal spot is collected by its respective microlens and relayed through a long pass filter (cut on $\lambda = 575\ nm$) to a CMOS camera (Basler acA2000-340km, 2048 × 1088 pixels) via a combination of the tube lens and a single lens reflex camera lens (SLR, Nikon 28-80mm, f/3.5). The camera sensor is located one focal length behind the SLR lens, and records an image of the fluorescence as seen at the back of the microlens array. Compared with the singlet relay lens used in the first version of the microlens microscope (Figure 3-2), the SLR lens produces a highly corrected image of the microlens apertures over a large FOV. Therefore a larger area of the microlens array can be faithfully imaged onto the camera sensor. Since the total imaging throughput is proportional to the number of microlenses imaged onto the camera sensor, the use of a SLR lens directly results in a higher imaging throughput. In all experiments presented here, the SLR lens focal length is set to be 30 mm, meaning that the image on the camera sensor has a magnification of 0.15× (30mm/200mm). One can consider the microlens array to function as an array of point scanning microscope objectives, with the camera performing the task of a detector array.

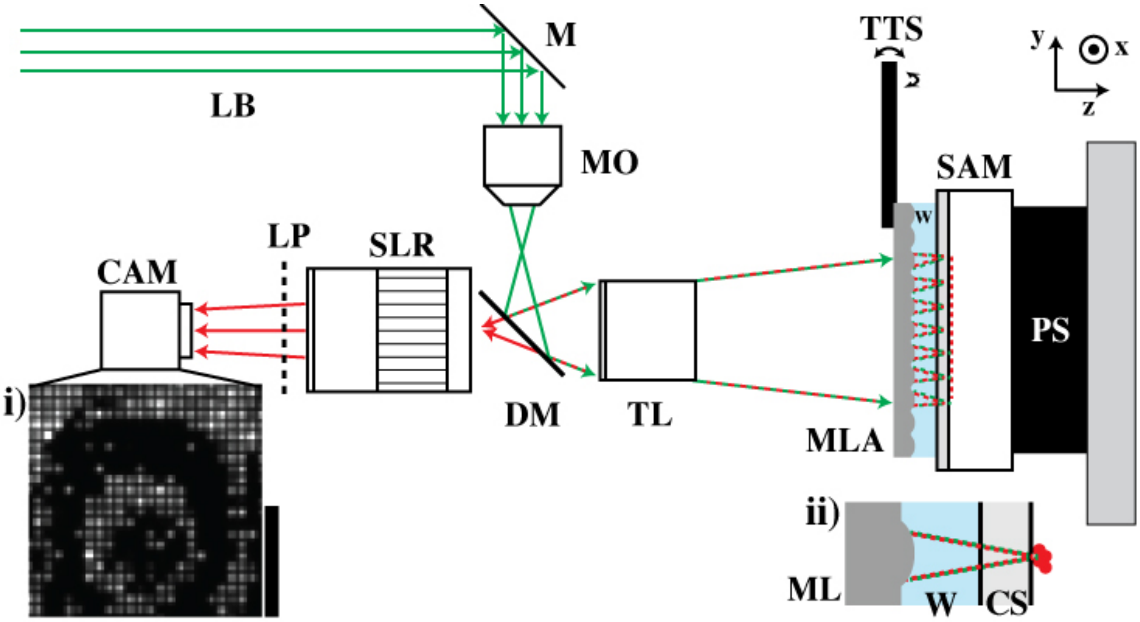

Figure 3-9: Experimental setup. Green rays: laser excitation (λ=532nm); Red rays: fluorescence emission (λ=575nm); LB: laser beam (green, λ=532nm); M: mirror; MO: 10× or 50× microscope objective; DM: dichroic mirror (cut off λ=550nm); TL: tube lens (focal length of 200 mm); TTS: tip/tilt stage. Tip and tilt are around the x- and y-axes. MLA: microlens array, focal length of 345 μm in water; W: water (immersion fluid); SAM: sample (well plate or tissue slide); PS: piezoelectric stage. The stage is scanned along the x- and y-axes; SLR: SLR camera lens (focal length of 28-80 mm); LP: Long-pass filter (cut on λ=575nm); CAM: camera; Inset i): A section of a raw camera frame during imaging. Scale bar is 1 mm in object space. Inset ii): Detailed view of a microlens (ML) focusing the laser (dashed lines) through water (W) and a #1.5 coverslip (CS) and into the fluorescent sample, depicted as red shape.

As was the case in first microlens microscope prototype in Section 3.1, the raw image at the camera is an array of bright spots, each corresponding to the fluorescence excited and collected by one microlens (Figure 3-9i). By recording the intensity relayed by a given microlens as the sample is scanned, an image of the portion of the sample directly under that lens may be obtained. The camera is operated at 200 frames per second (fps), and the raster scan line rate is set to an integral number of camera frames to avoid image shearing. The rate at which the software can compress the data is the limiting factor for the pixel throughput when using the large pixel count CMOS image sensor (2 Mpx) along with the SLR lens. We restrict the camera to a 976×976 pixel region of interest so that the computer can losslessly compress the incoming image stream without requiring a large RAM buffer.

3.2.3 Imaging Resolution

In order to determine the resolution of our system, we image sub-resolution fluorescent beads, i.e. having diameters (500 nm) that are smaller than the spot size. The image of a sub resolution bead provides a good approximation to the PSF of a fluorescence imaging system [13]. We fit a two dimensional Gaussian to the images of each of ten beads dried onto a microwell plate. The image of a typical 500 nm bead is shown in Figure 3-10, along with a line plot of the image intensity along the x-direction (FWHM = $1.74\ \mu m$ for this particular bead). The mean FWHM of the bead images is $1.72 \pm 0.08\ \mu m$, and indicates the resolution of our system. This is slightly worse than would be expected of a diffraction limited lens 0.18NA lens ($1.49\ \mu m$). This is due to the spherical aberration inherent when producing microlenses via resist reflow [142].

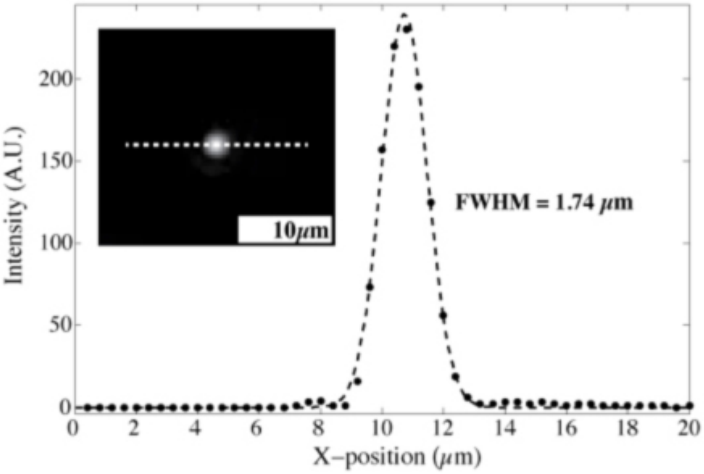

Figure 3-10 Typical intensity line cut of an image of a fluorescent bead (500 nm diameter), obtained by microlens array using water immersion imaging. Dots are experimental data and dashed line is a Gaussian fit (FWHM = 1.74 μm). Inset: Image of the 500 nm fluorescent sphere, with dashed white line indicating position of line cut for one-dimensional intensity plot.

3.2.4 Gigapixel Imaging

A 384-well microwell plate (Figure 3-11a,b) is loaded with fluorescent beads (Nile red, Invitrogen, 5 μm diameter) in water and then left to dry. This sample is then imaged as described in section 3.2.2 with an integration time of 1 ms per pixel, and raster scan step size of 500 nm. A microscope objective with a magnification of 50× (Figure 3-9) is used in order to create a relatively flat excitation field. The images formed by the microlenses are stitched together using a custom written MATLAB script to produce a 6600 px × 6600 px image of each well. The stitching procedure uses the 10 μm overlap between each pair of FOVs to compute the relative signal gain and pixel offset between FOVs, thereby correcting for possible fabrication imperfections. The overlapping areas of each pair of FOVs (e.g. FOV 1 and FOV 2) are then multiplied by the vignetting functions $V_1(u) = (u/b)^{1.5}$ (applied to FOV 1) and $V_2(u) = 1 - V_1(u)$ (applied to FOV 2), where u is distance from the FOV 1 border, and b is the width of the 10 μm overlap region in pixels. Note that for any two overlapping regions, the sum of the vignetting functions is unity over the entire overlapping region. After vignetting, each FOV is translated by the previously calculated pixel offset and the vignetted signal in the overlap regions is summed, yielding seamless stitching of thousands of FOVs [15].

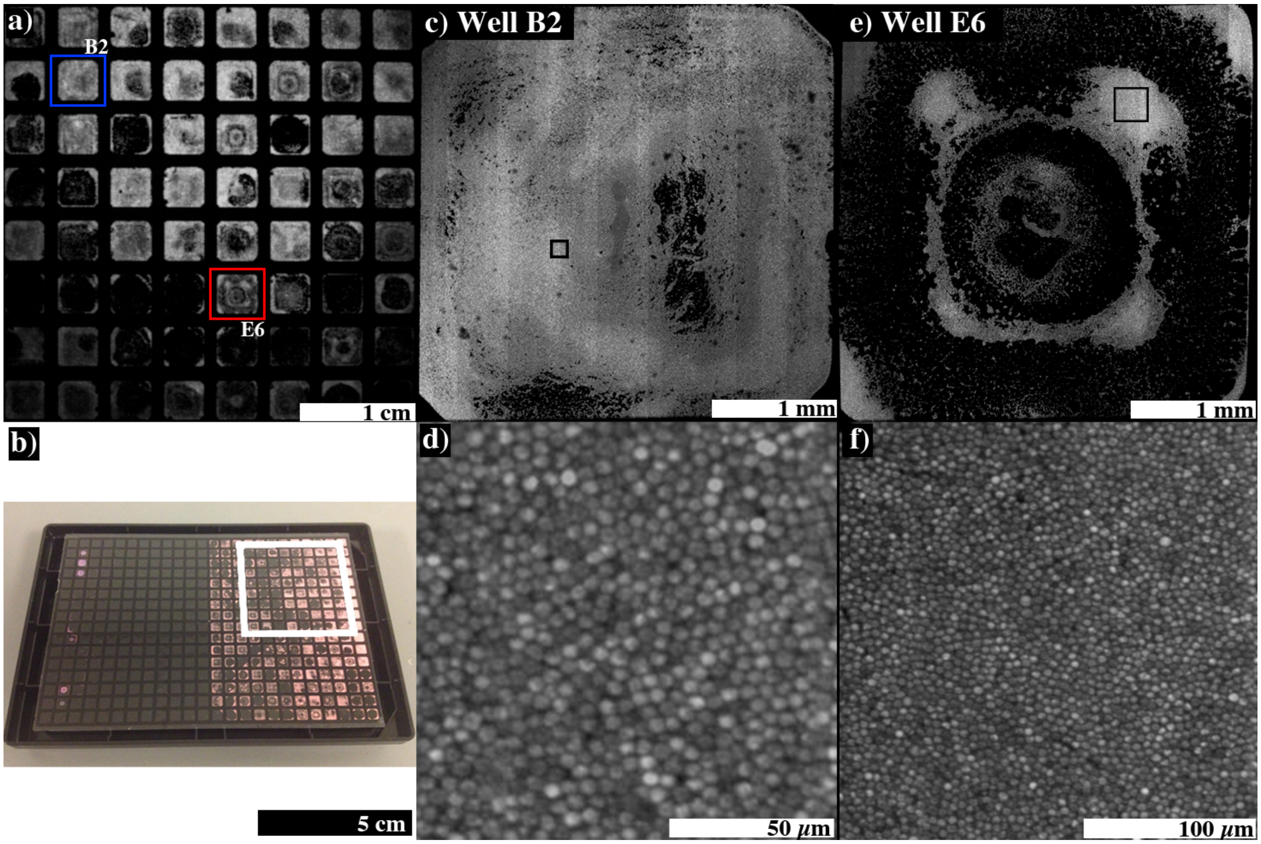

Figure 3-11 (a) Low resolution image of the 8 × 8 well imaged area. The entire FOV is 3.6 × 3.6 cm, corresponding to the boxed region in (b). (b) Photograph of the 384-well plate showing loaded fluorescent sample (5 *μm* beads) in the right half of the plate. The white box indicates the FOV in (a). (c) Close up of well B2. (d) Zoom in of the boxed region in well B2 showing fluorescent beads. (e) Close up of well E6 (c). (f) Zoom-in of the boxed region in well E6 (e) showing fluorescent beads.

Images of typical wells are shown in Figure 3-11c-f. Each well is imaged by an array of 34 × 34 microlenses that correspond to a region on the camera sensor with an extent of 96 × 96 pixels (~8 pixels / microlens). The entire FOV consists of 64 (8x8) wells that are imaged in parallel by the microscope array. The well plate scan produces 5.24 Gpx of raw data in 3.5 minutes, corresponding to a raw pixel throughput of 24.9 Mpx/s. The well plate image of Figure 3-11a is therefore shown in low resolution, since the image at full resolution (5.24 Gpx) could not of course be shown in one figure panel. Accounting for the fact that nearly half of the well plate area that is imaged onto the camera corresponds to the plastic support structure of the well plate, the well plate scan corresponds to 2.78 Gpx of sample data and a sample pixel throughput of 13.2 Mpx/s. This throughput is more than double that of commercial state-of-the-art systems such as the ImageXpress Micro from Molecular Devices, which achieves 4-5 Mpx/s [16].

When imaging the 64 well sample, the image on the camera takes up 976 × 976 pixels, corresponding to 360 × 360 microlenses. Thus, we use less than half of the available camera sensor area and available microlenses. This is because the desktop computer employed is not capable of streaming the data sufficiently fast for the entire sensor and entire microlens array to be used. For a 64 well scan with a raster scan step size of 500 nm, the compressed 8-bit data from the camera is ~44 GB. This limitation could be overcome with a faster image compression algorithm, more random access memory (in order to buffer all of the incoming images) or a solid-state hard drive array to store the uncompressed data.

3.2.5 Tissue Imaging

We use our lens array to image a H&E stained tissue microarray (TMA) slide (USA Biomax, BLSC1501), mounted on a microscope slide and sealed with a #1.5 coverslip. TMA slides are used in biological research for high throughput gene expression studies, often for cancerous tissues [17,18]. We image the eosin dye in the TMA slide in one 3.5 minute scan at a raster scan step size of 500 nm and an integration time of 4.5 ms per pixel. A low resolution image of the entire sample is shown in Figure 3-12a. Typical images of 1.1 mm diameter tissue slices are shown as Figure 3-12b and e. Zoom-ins of the tissue cores in Figure 3-12c,d and f show the level of detail captured in each image. We note that because a TMA slide is small compared to the 8 × 8 well region of the microwell plate in Figure 3-11, we do not take full advantage of the pixel throughput of our technique. A larger TMA with a denser array would be more appropriate with our setup and could see sample pixel throughputs exceeding even that of the well plate sample.

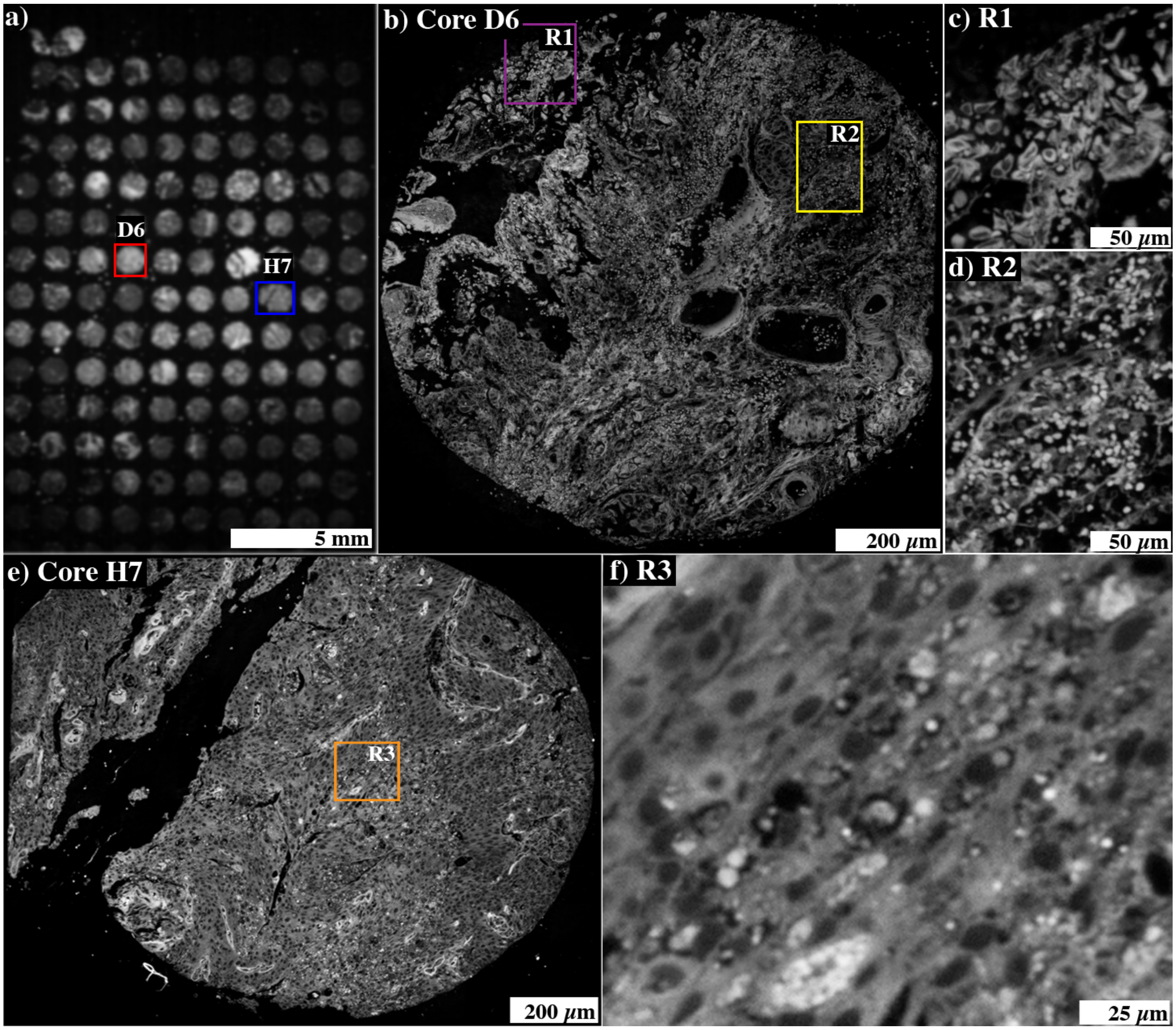

Figure 3-12 H&E stained tissue microarray imaging. (a) A low resolution image of the entire imaging area. Cores of interest D6 and H7 are boxed. (b) Close up of core D6. Regions of interest R1 and R2 are boxed. (c) Zoom in of region of interest R1 in core D6 (b). (d) Zoom in of region of interest R2 in core D6 (b). (e) Close up of core H7. A region of interest, R3, is boxed. (e) Zoom in of region of interest R3 from core H7 (e).

We also image a coverslip-sealed mouse kidney section stained with AlexaFluor 568 Phalloidin (Invitrogen FluoCells Slide #3). The sample, shown in its entirety in Figure 3-13a has an extent of $1\times0.6\ cm$. Actin filaments in the glomeruli are visible in Figure 3-13b.

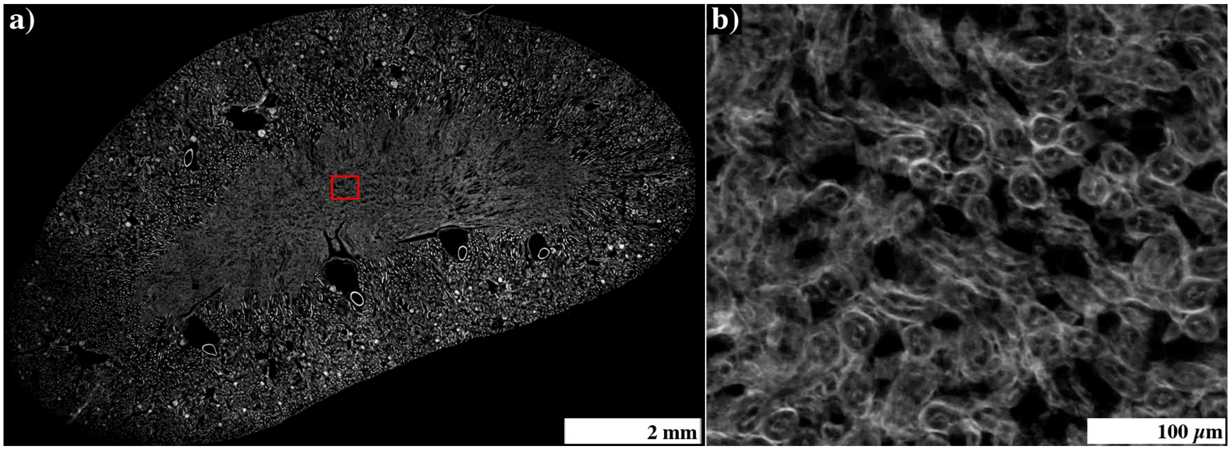

Figure 3-13 Imaging of a mouse kidney section (Invitrogen Fluocells prepared slide #3). (a) Image of AlexaFluor 568 Phalloidin fluorophore.distribution. The image has extent 1 × 0.6 cm, and represents the entire tissue section. (b) Zoom-in of boxed region of panel a.

Because both tissue samples (Figure 3-12 and Figure 3-13) have weaker fluorescent emission than the microsphere sample, we use an objective with a magnification of 10× to expand the beam, rather than one with a magnification of 50×. This means a larger portion of the original beam is reflected by the dichroic mirror into the excitation path, resulting in more power at each excitation focal spot. It also results in a more uneven (Gaussian) illumination profile at the microlens array, which is apparent in Figure 3-12a. Imaging larger tissue samples would require a higher power laser spread out over a larger area, perhaps coupled with more efficient beam shaping optics such as a flat and collimated beam generator. At the current illumination intensity we have not observed any photobleaching effects in our system.

3.3 Third Generation: Multi-channel Fluorescence Imaging

Most high throughput fluorescence microscopy applications require multiple fluorescent channels. For example, co-localization assays in drug discovery compound screening can indicate whether there is uptake of a certain chemical into the cell. In tissue imaging, multicolor labeled neurons (Brainbow) can facilitate the mapping of the nervous system of small animals [146], [147].

In the third generation of the microlens array microscope, we expand the applicability of the system by introducing a three channel laser excitation source (473/532/658 nm) which allows for multichannel fluorescence imaging. We also refine the microlens array in order to increase imaging resolution and optical efficiency. Additionally, we explore the extended dynamic range made possible by the microlens array microscope.

3.3.1 Microlens Array Fabrication

In the third generation of the microlens array microscope, we sought to increase the resolution beyond that of the second generation system. This requires increasing the microlens diameter while shrinking the focal length to obtain a higher NA. Larger microlens diameters improve resolution but can decrease pixel throughput because fewer microlenses are imaged onto the image sensor for a given sample size. This effect can be mitigated by employing a hexagonal grid microlens array, which has a higher maximum packing density than a square grid (90.6% vs. 78.5%). A hexagonally packed microlens array gives 15% more microlenses per unit area than a square grid array.

Shrinking the microlens focal length presents practical issues with sample geometry. The microlens focal length must be at least $220\ \mu m$ in order to focus through a #1.5 cover slip (nominal thickness $170\ \mu m$) and to allow for height variations of the cover slip and sample. Furthermore, the sample and microlens array must be extremely flat; variations in distance between the focal spot array and the sample over the FOV must not exceed the depth of field of the microlens array. This condition becomes increasingly difficult to fulfill as the NA of the microlens array is increased since the depth of field varies as $1/\mathrm{NA}^2$. For example, for a 3 cm square FOV, and a microlens depth of field of $10\ \mu m$, this corresponds to a flatness of 1 part in 3000.

This flatness requirement became problematic due to the flexible nature of the PDMS mold. When curing the optical adhesive in the final step of fabrication, the PDMS mold deforms, leading to a significantly bowed microlens array. This bowing, coupled with a smaller depth of field results in part of the microlens array microscope FOV being out of focus.

This tight tolerance requirement necessitated a few modifications in the microlens array fabrication process. We list the alterations to the fabrication process below along and reference the relevant steps in Figure 3-1:

1) **M1**: The microlens array master is fabricated on a 3×3 inch quartz slide 1 mm thick because it is a more robust and rigid substrate than a silicon wafer.
2) **S1,S2**: A small volume of PDMS is poured onto the quartz/photoresist master (only enough to cover it). A 2×3 inch glass slide (1 mm thick) is placed directly on top of PDMS covered master. The glass/PDMS/quartz sandwich is degassed to get rid of air bubbles in the PDMS and then is baked in an oven for 3 hours at 65°C. The PDMS adheres preferentially to the glass slide. The master is separated from cured-PDMS-on-glass inverse replica by gently prying with a razor blade.
3) **R2**: The inverse replica is made up of a thin (≈ 100 µm) layer of PDMS on a rigid glass substrate. This rigidity prevents deformation of the inverse mold during the replication process (R2). After stamping and curing the optical adhesive (NOA 61), the rigid inverse mold and positive microlens array replica must be separated by gently prying with a razor

blade. The optical adhesive tends to adhere moderately to the PDMS making this step delicate. This step has a success rate of about 1 in 3. Further investigation of possible release agents is needed for a higher yield.

3.3.2 Optical Setup

The optical layout of our approach is shown in Figure 3-14. A multi-wavelength excitation laser (Laserglow, 473/532/658nm) emits a beam with an output power of up to 150 mW per channel. The beam is expanded by a 50× microscope objective and reflected into the optical path by a quad-band dichroic mirror (Chroma zt405/473/532/660rpc). A 125 μm pitch hexagonal grid microlens array splits the laser beam into an array of focal spots. The microlenses have diameters of 122 μm and sags of 11.7 μm. A micrograph of a portion of the microlens array is shown in Figure 3-15. The entire array measures 4.5 cm × 4.5 cm and contains more than 140,000 microlenses. We observe no measurable axial chromatic aberration; the microlens array has a focal length of $248\mu m \pm 2\mu m$ (NA=0.24) for all three laser wavelengths.

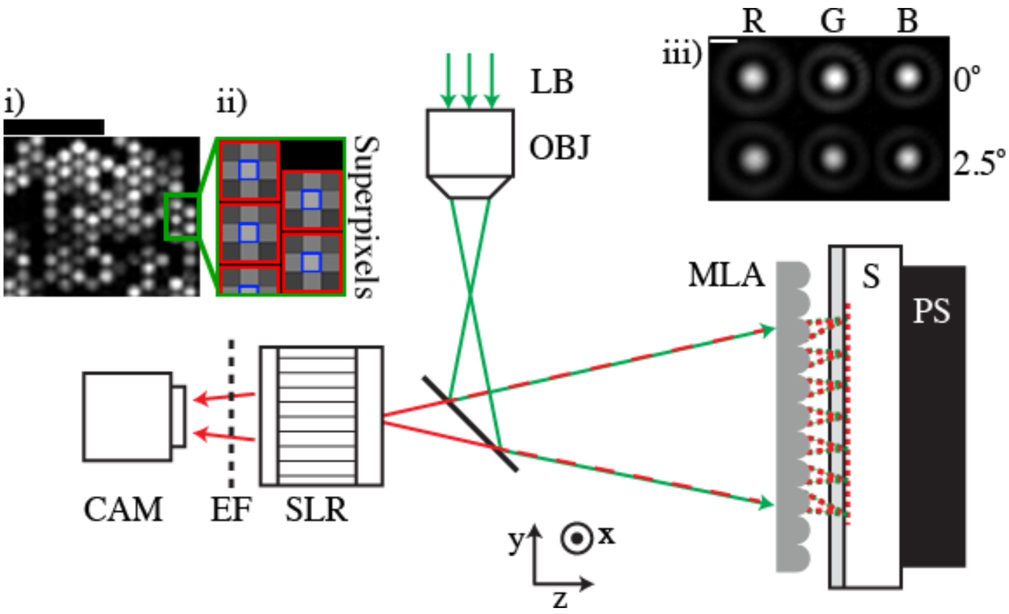

Figure 3-14 Schematic of the multichannel microlens microscope. A microscope objective (OBJ) expands a laser beam (LB) that is focused into an array of focal spots by a microlens array (MLA) on a fluorescent sample (S). The sample sits on a raster scanning piezo stage (PS) and the microlens array is imaged onto a camera (CAM) by a single lens reflex (SLR) lens. A quad-band dichroic mirror (DM) reflects the laser lines (473/532/658nm) while passing fluorescence wavelengths; an emission filter (EF) provides additional wavelength filtering. Inset i) Raw image of microlens array as recorded by the camera. Scale bar is 1 mm. Inset ii) Zoom-in of green area outlined area in i). Representative N=9 superpixels are outlined in red; N=1 superpixels are outlined in blue. Inset iii) Representative focal spots created by the microlens array with red (R), green (G) and blue (B) lasers at field angles of 0^o and 2.5^o. Scale bar is 2 μm.

Each microlens in the array functions as an independent point scanning microscope by collecting the fluorescence emitted at its focal spot and relaying it back to a CMOS camera (Basler acA2000-340km) via a 50 mm focal length, f/1.4 single lens reflex (SLR) camera lens with an aperture set to f/8. The SLR lens is placed 400 mm from the microlens array, equal to the separation between the focal plane of the expansion microscope objective and the microlens array.

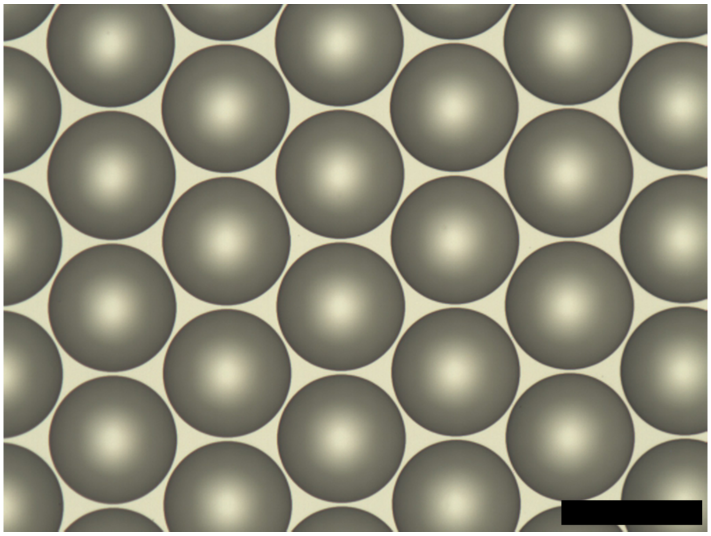

Figure 3-15 Brightfield reflection micrograph of the hexagonal grid microlens array used for experiments in Section 3.3. Scale bar is 125 μm.

The fluorescence collected by each microlens exits its aperture at the same angle as the laser illumination at that given position in the microlens array. Consequently, the fluorescence converges to the center of the SLR aperture. This geometry is critical for avoiding vignetting from microlenses towards the periphery of the array. For example, if the illuminating laser beam were collimated, some of the signal from non-central microlenses would miss the physical aperture of the SLR lens. This is a similar concept to the de-scanning mirrors in a point scanning confocal microscope [12]. Without de-scanning the fluorescence collected by the microscope objective, the signal in a confocal microscope would miss the confocal pinhole for non-zero field angles (ie. away from the center of the FOV).

A fluorescence filter between the SLR lens and the camera filters out the wavelength range appropriate for the fluorophore being employed. The SLR lens is placed ~400 mm from the microlens array, resulting in a ~7× demagnification factor at the camera sensor plane. The fluorescence distribution on the camera sensor is an array of bright spots (Figure 3-14i,ii), with each corresponding to an image of a microlens. The brightness of each microlens imaged in this way is proportional to the fluorescence excited from the sample at its focal spot. The set of camera sensor pixels corresponding to the image of each microlens can therefore be thought of as playing the same role as the point detector of a conventional scanning confocal microscope.

The camera acquires a video at 200 fps with the camera gain set to its minimal value. The sample is raster scanned under the focal spot array as the movie is recorded. A photograph of the microlens array and sample during the scanning process is shown in Figure 3-16. The sample sits on a closed loop piezoelectric stage (Newport NPXY200SG) that is driven by a sawtooth wave to yield a speed of $100\,\mu m/s$ along the x-direction, resulting in a sampling density of $0.5\,\mu m$ per camera frame. A slow linear ramp of $0.37\,\mu m/s$ is applied along the y-direction. The image of the portion of the sample gathered by each microlens (a sub-FOV) is assembled by summing pixel values of the microlens image in the raw video and reorganizing them appropriately into a two dimensional image. This image has dimensions $135\,\mu m \times 118\,\mu m$ and a pixel size of $0.5\,\mu m$. Fluctuations in laser intensity are mitigated by dividing by the normalized average of all microlens intensities from each camera frame. A large FOV image is created by stitching together all of the sub-FOVs on a hexagonal lattice using nonlinear blending to minimize seams [145].

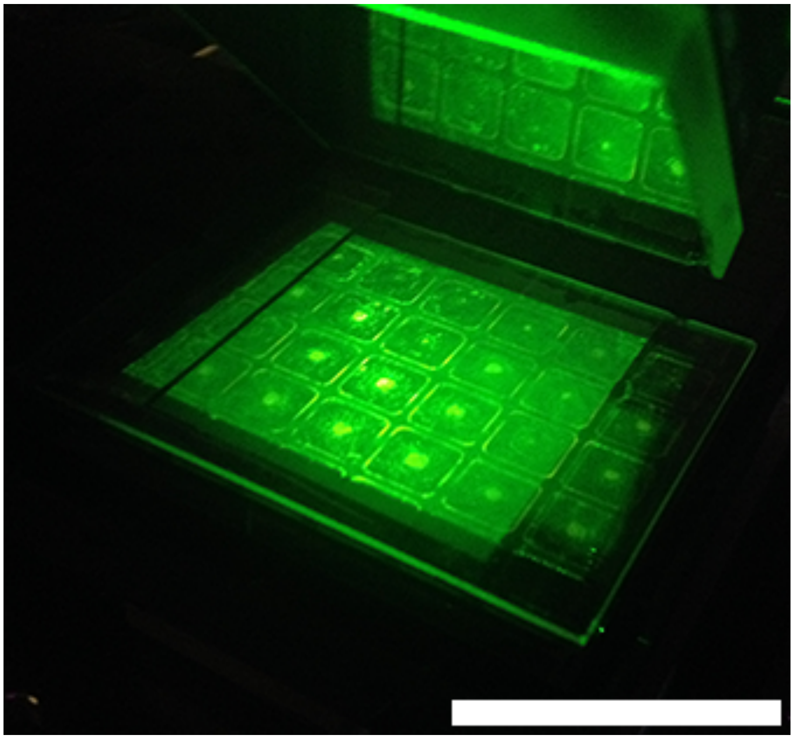

Figure 3-16 Photograph of the microlens array above a 96-well plate during the scanning process. The small squares are the wells of a 96-well plate. A mirror, visible above the microlens array, reflects the slowly diverging excitation laser beam down onto the microlens array. Scale bar is 50 mm.

The resolution of our system is determined by the focal spot size. As with the first two generations of the microlens microscope, the focal spots created by the microlens array do not reach the diffraction limit owing to spherical aberration inherent in the reflow molding fabrication technique. We measure the full width at half maximum (FWHM) values of the microlens focal spots by imaging the focal plane with a microscope objective with a NA of 0.80 and a magnification of 100×. Gaussian fits are applied to the images of the focal spots (Figure 3-14iii), for field angles of 0° and 2.5° (the maximum field angle used in this work). A focal stack is acquired by moving the microlens array slowly through the focus of the microscope objective. We then extract the frame with the highest peak pixel value and use this image for focal spot characterization. The focal length was determined experimentally by recording the distance between this focal spot plane and the base of the microlens. Thus, the working distance W_d of the microlens array is equal to the focal length minus the sag: $W_d = 248\,\mu m - 11.7\,\mu m = 236.3\,\mu m$.

The small field angle has almost no discernable effect on the focal spot size and shape. The focal spot FWHMs at 0° field angle are $1.44\,\mu m \pm 0.03\,\mu m$, $1.30\,\mu m \pm 0.03\,\mu m$ and $1.20\,\mu m \pm 0.03\,\mu m$ for red, green and blue excitation lasers, respectively. At a field angle of 2.5°, the FWHMs are $1.47\,\mu m \pm 0.03\,\mu m$ (red), $1.30\,\mu m \pm 0.03\,\mu m$ (green) and $1.22\,\mu m \pm 0.03\,\mu m$ (blue). The uncertainty is a 95% confidence bound for the Gaussian FWHM parameter when fit to an experimentally measured focal spot. The FWHM values are slightly larger than the FWHMs for a diffraction-limited 0.24 NA lens approximated by a Gaussian focal spot: 1.37 μm, 1.10 μm and 0.98 μm, respectively.

3.3.3 Depth of Field

Fluorescent samples are not completely flat over large areas. In HCS applications, fluorescent samples typically reside in microwell plates. For our system to have applicability in drug discovery labs that employ HCS, it is necessary that the microwell plate flatness be sufficient to ensure that the height variation within the FOV is less than the depth of field of the system. Figure 3-17a shows a contact profilometry trace of the bottom of an Ibidi 96-well plate. Over a 3 cm line trace, the variation in well height is $\sim 15\,\mu m$. The Figure 3-17a insets show a focus stack of a FOV containing wrinkled 5.3 μm diameter Nile Red beads (535/575nm excitation/emission peaks), imaged with the green excitation channel (532 nm) of the microlens microscope. Subjectively, the image quality variation over the 15 μm range is nearly imperceptible. We quantify the imaging quality by imaging an isolated sub-resolution 500 nm

Nile Red fluorescent bead (Invitrogen), yielding the PSF of the green channel of the system. The modulation transfer function (MTF) for each imaging depth is calculated by taking the magnitude of the Fourier transform of the measured PSF [148]. In Figure 3-17b we plot the MTF and PSF for imaging depths 6 μm above, 9 μm below and at the plane of best focus. As per convention, the MTFs are normalized to unity. Corroborating the observation that the imaging quality varies minimally over a 15 μm depth of focus, the MTF has almost no change over this range. Interestingly, at low spatial frequencies, the MTF of our system lies above that of a diffraction-limited 0.24 NA circular aperture widefield system. This is likely due to apodization of the microlens apertures by the steep angle of the lens at the periphery [148]. The result is increasing reflection losses towards the edge of the microlenses. This effect manifests itself as low-pass filtering. Note that this does not mean that our microlenses are more efficient at imaging low spatial frequencies than a diffraction-limited system. Because the MTF plot is normalized, the correct interpretation is that the low spatial frequency signal is boosted relative to the high spatial frequency signal when compared to the diffraction-limited case.

Figure 3-17 a) Blue curve: Contact profilometry height trace along a 3 cm line on a 96-well plate. Greyed out vertical bars are sections of plastic support on the well plate where there is no fluorescent sample. Insets: FOV of 5 μm diameter fluorescent microspheres (Nile Red, green channel) at the focal distances indicated by the dotted horizontal lines. Positions are relative to the best focus plane. Negative distances are closer to the microlens array and positive distances are farther away from the microlens array. Scale bar is 20 μm. b) Modulation transfer functions (MTFs) for the green laser channel at -6 (red), 0 (green) and 9 μm (blue) from the best focus plane. Diffraction limited MTFs for 0.24 NA wide field and confocal microscopes with circular apertures are shown in purple and cyan, respectively. All MTFs are normalized to a maximum value of 1. Scale bar is 2 μm.

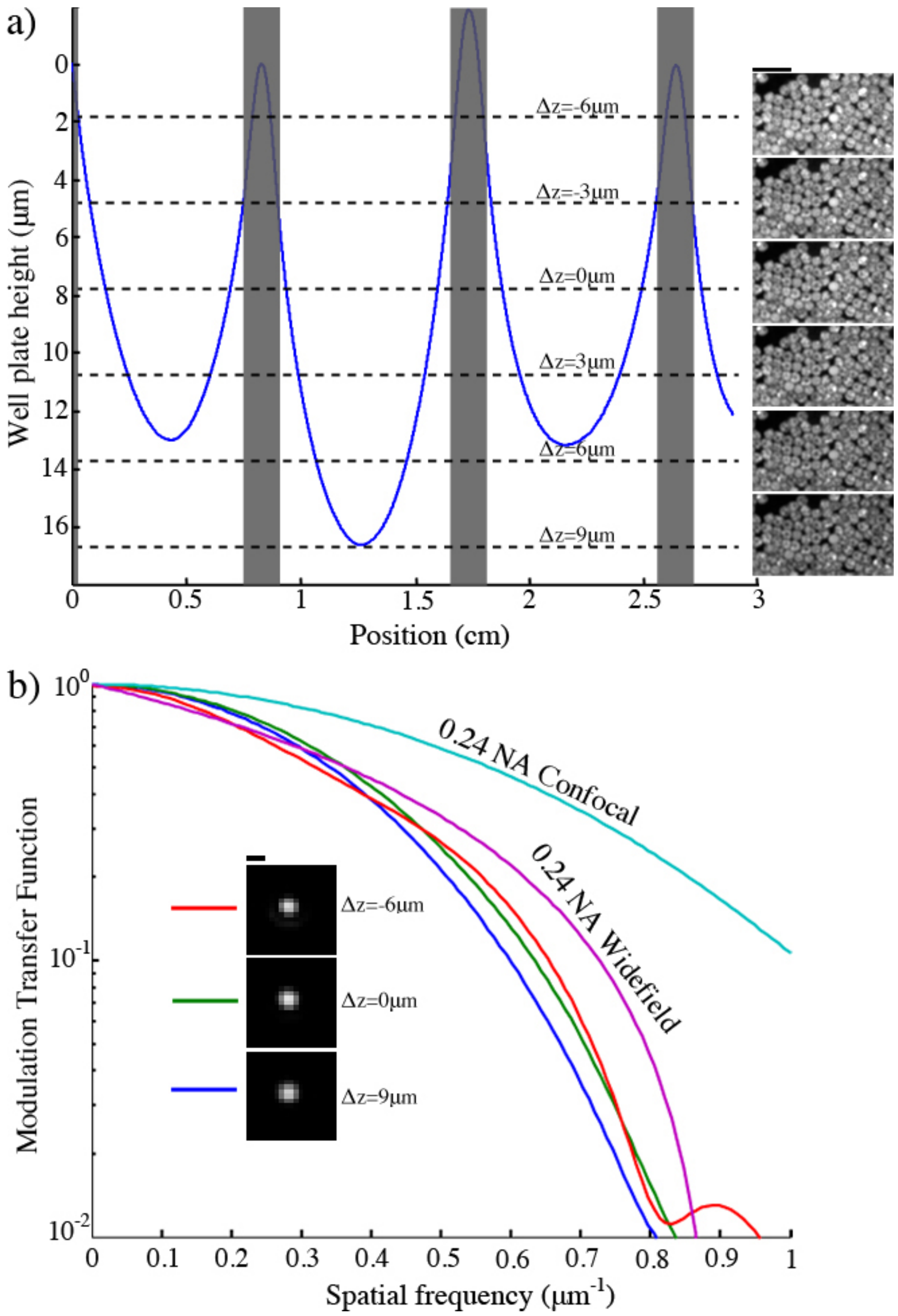

Figure 3-17 (continued)

3.3.4 Sequential Multichannel Imaging Results

To demonstrate the high throughput capabilities of our system, we fill 16 (4×4) wells of a 96-well plate (Ibidi) with a mixture of Dragon Green (Bangs Labs), Nile Red (Invitrogen) and Flash Red (Bangs Labs) fluorescent beads. The Dragon Green and Flash Red beads are nominally 7.3 μm in diameter and have excitation/emission peaks at 480/520nm, and 660/690nm, respectively. The Nile Red beads have excitation/emission peaks at 535/575nm, are nominally 5.3 μm in diameter and have been aged so that their surface is wrinkled, yielding high spatial frequency features. Three separate images of the 4×4 well area are acquired with laser wavelengths of 473 nm (blue), 532 nm (green) and 658 nm (red). The camera exposure time is 3.5 ms/frame and the approximate optical power in each focal spot is 0.13 μW, 3.1×10^{-2} μW and 3.7×10^{-2} μW for blue, green and red lasers, respectively. For 473 nm excitation, a 10 nm FWHM bandpass fluorescence emission filter centered at 500 nm is used. Long pass filters with cut on wavelengths at 575 nm and 664 nm are used for excitation wavelengths of 532 nm and 658 nm, respectively. These excitation wavelength and emission filter combinations separate the beads into their constituent populations without the need for spectral unmixing.

Figure 3-18 a) Three channel image of a 16 well section of a 96-well plate, filled with fluorescent microspheres. Red, green and blue fluorescent microspheres are excited with red, green and blue laser lines, respectively. Red and blue microspheres have a nominal diameter of 7.3 μm. Green microspheres have high spatial frequency features due to wrinkling and have a nominal diameter of 5 μm. White boxes denote locations of figures (b)-(e). Scale bar is 8 mm. b) to e): Zoom-in of regions indicated in (a). Scale bars are 25 μm.

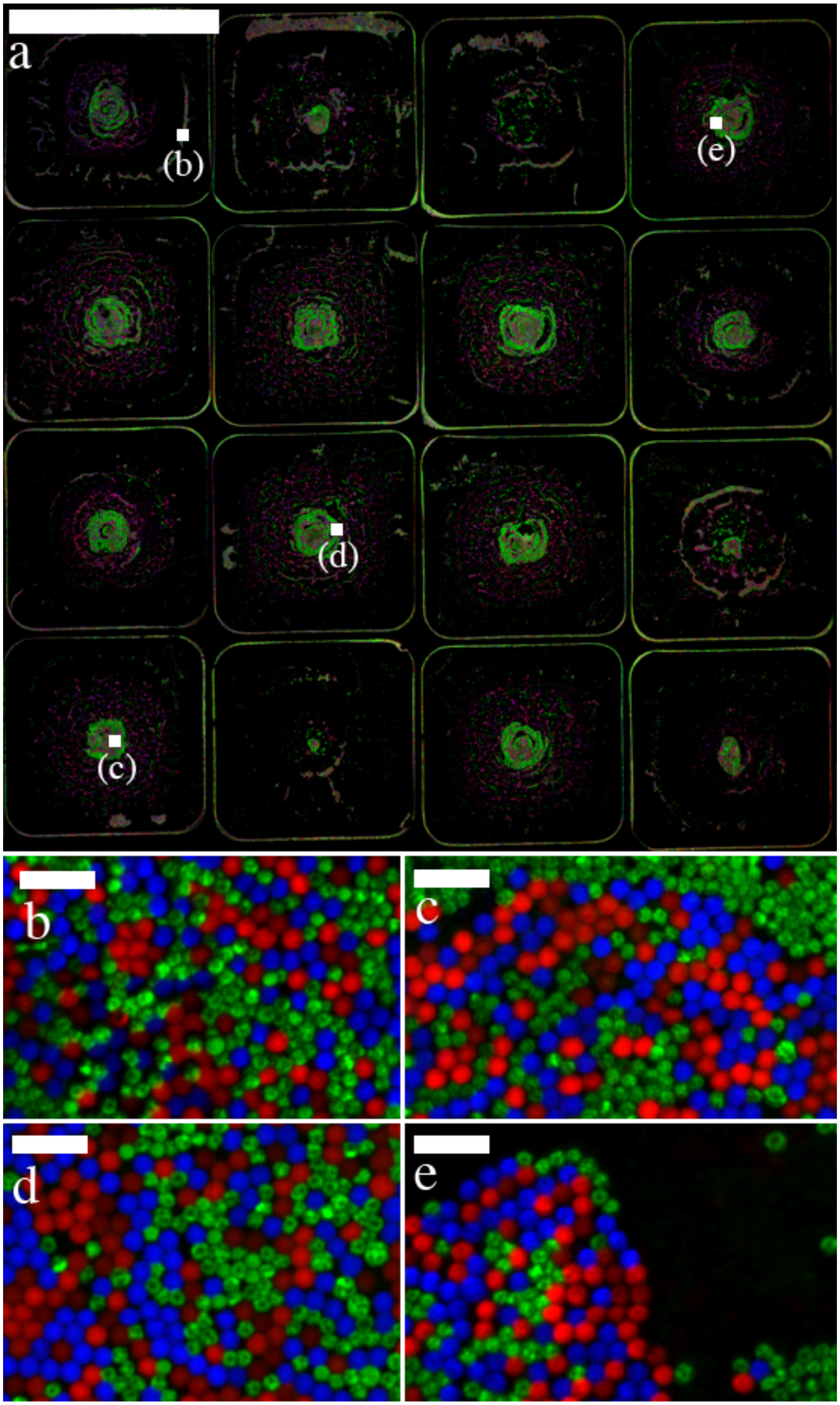

Figure 3-18 (continued)

In Figure 3-18, we show a 3-channel image of all 16 wells imaged (Figure 3-18a), along with magnified regions of four wells (Figure 3-18b-e). The red/green/blue color channels of the presented images correspond to the images obtained with red/green/blue lasers, respectively. Color channels are aligned by finding the position of their cross correlation minimum and correcting for this offset. Wrinkling of the green-colored beads is evident, while the blue- and red-colored beads have smooth surfaces. All areas of the 4×4 well region are in focus owing to the large depth of field of the microlenses, which accommodates both intra- and interwell height variations. The 4×4 well region has an area of $12.25\ cm^2$, corresponding to 90,550 microlenses. At a frame rate of 200 fps this is a total pixel throughput of 18.1 Mpx/s. A portion of this data corresponds to the plastic support regions between wells, which contain no fluorescent sample. Also, a small amount of overlap ($10\ \mu m$) between neighboring sub-FOVs is necessary for the stitching process. After accounting for these two factors, the final dataset for each color consists of 16 images each 16000×16000 pixels in size. The acquisition time is 320 s, corresponding to a pixel throughput of 12.8 Mpx/s.

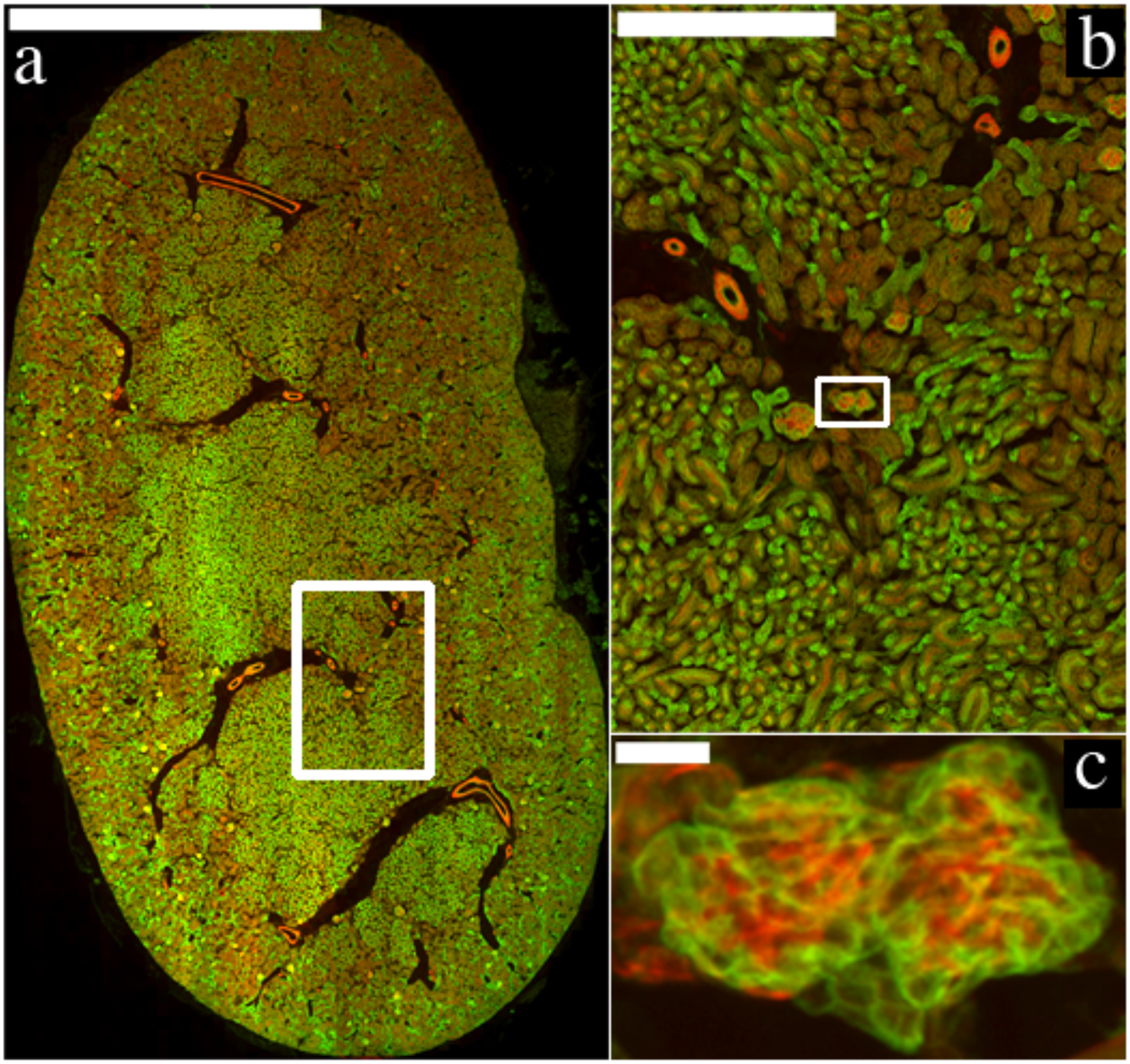

Figure 3-19 a) Full-field view of a dual channel image of a mouse kidney slice. Scale bar is 3 mm. b) Zoomed-in view of boxed region in (a). Scale bar is 500 μm. c) Further magnified view of boxed region in (b). Scale bar is 10 μm. Animation showing the zooming in from (a) to (b) to (c) is shown as Movie 3-2.

We demonstrate the tissue imaging capability of our system by imaging a 16 μm thick slice of mouse kidney (Life Technologies FluoCells Prepared Slide #3), sealed between a microscope slide and a #1.5 coverslip. The tissue section is stained with Alexa Fluor 488 and Alexa Fluor

568 Phalloidin, while the fluorescent stain 4',6-diamidino-2-phenylindole (DAPI) is also present but not imaged. Laser excitation wavelengths of 473 nm (focal spot power ≈ 0.20 μW) and 532 nm (focal spot power ≈ 0.55μW) are used to excite the Alexa Fluor 488 and 568 fluorophores, respectively, whose emission is filtered with long pass filters with cut-on wavelengths of 500 nm and 575 nm. The camera integration time is set to 4.9 ms/frame. As some of the tissue features stained with different fluorophores tend to be co-localized, we align the channels by finding their cross correlation maximum and correcting for that shift. The resulting aligned image is shown in Figure 3-19a, with the Alexa Fluor 488 (568) channel in green (red). The sample has an extent of $\sim 0.5 \times 1$ cm. At a moderate zoom level, the brush border and glomeruli can be identified (Figure 3-19b). At full image size (Figure 3-19c), fine features such as filamentous actin and microtubules are visible.

3.4 Parallel Multichannel Imaging

Not all fluorescent samples are large enough to take full advantage of the large FOV imaged by our microlens microscope. For example, the throughput of the sequential multichannel system in the previous subsection is only roughly 0.75 Mpx/s when imaging the small mouse kidney sample. This throughput is modest because the sample is small, meaning that not all of the microlenses within the array are used. To increase throughput for small samples, we split the fluorescent signal from the sample into low-pass ($500\, nm < \lambda < 532\, nm$) and high-pass ($575\, nm < \lambda$) spectral components, and image both simultaneously. Spectral decomposition is achieved by inserting a long-pass dichroic mirror (edge $\lambda = 532\, nm$) between the quand-band dichroic mirror and SLR lens in Figure 3-14. A pair of broadband mirrors is positioned on either side of the long pass dichroic mirror. The broadband mirrors are tilted at small (and opposite) angles with respect to the long-pass dichroic, sending the fluorescence signals from the short-and long-pass components into the SLR lens at opposing angles. Emission filters are inserted at 45^0 with respect to each of the broadband mirrors to cut out any residual laser illumination. This arrangement of a long-pass dichroic filter, pair of broadband mirrors and emission filters will be termed a spectral splitting module (SSM).

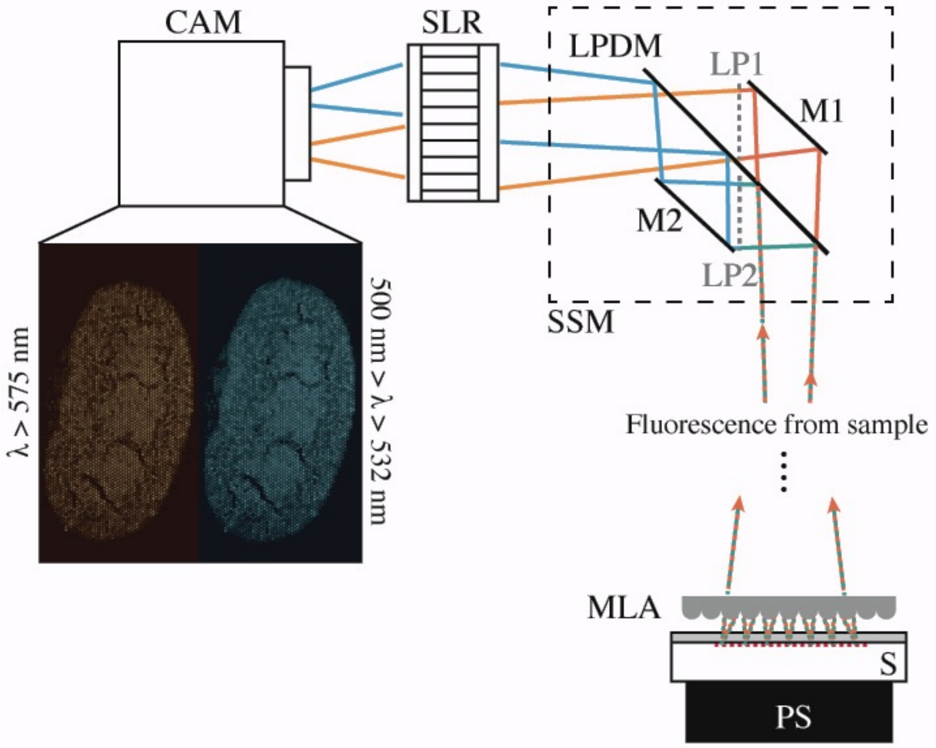

Figure 3-20 Parallel multichannel microscopy with a microlens array (MLA). The excitation geometry (not shown) is identical to that in Figure 3-14. Fluorescence from the sample (S) - which sits on a piezo stage (PS) - enters a spectral splitting module (SSM) after the quad-band dichroic mirror (not shown, see Figure 3-14). The SSM consists of: a long-pass dichoic mirror (LPDM [edge $\lambda = 532\, nm$]); a pair of broadband mirrors (M1 & M2); a pair of long-pass emission filters (LP1 [$\lambda > 575\, nm$] & LP2 [$\lambda > 500\, nm$]). The SSM relays long- and short-pass spectral copies at opposing angles into the SLR lens, yielding spatially separated spectral images (inset) on the camera (CAM) sensor. The spectral copies are shown in false color in the inset (actual camera sensor is greyscale only).

The spectral components of the fluorescent signal arrive at the SLR lens at opposing angles. As a result, the SLR lens images two copies of the microlens apertures onto the camera sensor – one for each spectral component. The setup is shown schematically in Figure 3-20. We use long-pass filters ($\lambda > 500\,nm$ and $\lambda > 575\,nm$) as emission filters in the SSM, but in general any pair of filters such as bandpass filters may be used provided that the signal level of each spectral copy is comparable.

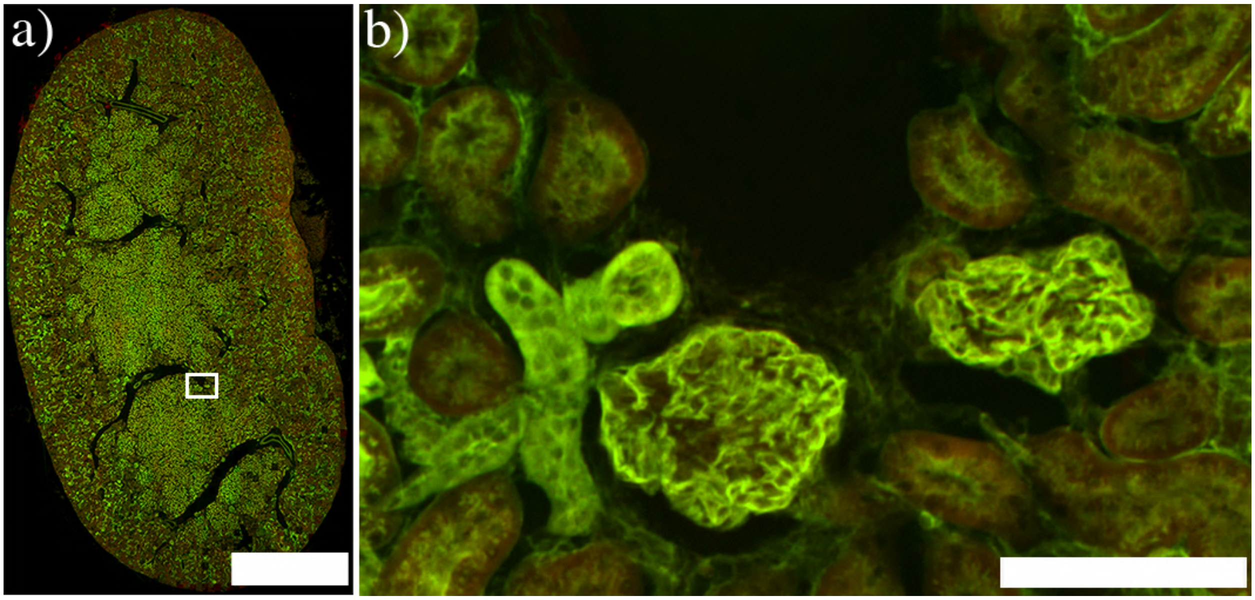

Figure 3-21 a) Dual-channel mouse kidney slice image, acquired in the parallel configuration. Red color is the $\lambda > 575$ nm channel and green color is the 500 nm $> \lambda > 532$ nm channel. Scale bar is 2 mm. b) Magnified view of boxed region in (a). Compare the right hand glomerulus with the same structure in Figure 3-19c. Scale bar is 50 μm.

The kidney section shown in Figure 3-19 is reimaged using the parallel multichannel setup described above, using 473 nm laser excitation. The resulting image is shown in Figure 3-21. Spectral multiplexing results in a direct doubling of effective pixel throughput to 1.5 Mpx/s. There is appreciable bleed through of the two spectral channels because of the emission filters used. Nevertheless, the localization of the fluorescent stains to their appropriate cellular structures is evident. Spectral bleeding can be mitigated or avoided altogether by using bandpass filters within the SSM that are appropriate for the given fluorophore.

3.5 Extended Dynamic Range

As discussed, our method records the fluorescence collected by each microlens by integrating the pixels associated with its image on the camera sensor. Interestingly, this extends the dynamic range of our imaging technique to exceed that of each pixel of the camera. Recall from Figure 3-14ii that each microlens aperture is imaged to a $n \times n$ pixel region on the camera sensor. Therefore, even though the camera records an 8-bit video, the conglomeration of the $\mathrm{N} = n^2$ pixels assigned to each microlens can take on values from 0 to $255\times\mathrm{N}$. We will call this combination of N pixels a "superpixel". The extent of each microlens (122 μm), the extent of the camera sensor pixels (5.5 μm) and the ~7× demagnification provided by the SLR lens result in the superpixel comprising N=9 pixels.

The PSF created by the SLR lens on the camera sensor is comparable in size to the image of a microlens, leading to an image of a microlens that resembles a Gaussian spot. As a result, the center of the image of a microlens will saturate its camera pixel before a pixel on the periphery of the microlens image saturates. This restricts off center microlens pixels to smaller dynamic ranges than the center. Thus, unsaturated superpixel values are restricted to values smaller than $255\times9 = 2295$.

To quantify the dynamic range of our system, we record a movie of microlenses relaying fluorescence in the following configuration. The piezo stage is not scanned and the SLR lens aperture is set to f/8. The microlens focal spots are brought into focus so that they excite fluorescence at the sample. We record 300 frames at 200 fps. Laser fluctuations are mitigated by dividing each frame by the average intensity of all microlenses in the frame. For normalization purposes, we also multiply by the highest average microlens intensity of all of the frames. The signal-to-noise ratio (SNR) of a superpixel i is calculated by dividing the mean superpixel value μ_i by its standard deviation σ_i. The SNR curve for a N=1 superpixel is calculated using only the central pixel in each superpixel (blue boxes, Figure 3-14ii). For the N=9 case we sum all 9 pixels that make up the image of each microlens and then calculate the SNR using this summed value (red boxes, Figure 3-14ii). In order to avoid pixel value saturation, we do not include any superpixels for which any pixel reaches a value of 255 during the movie.

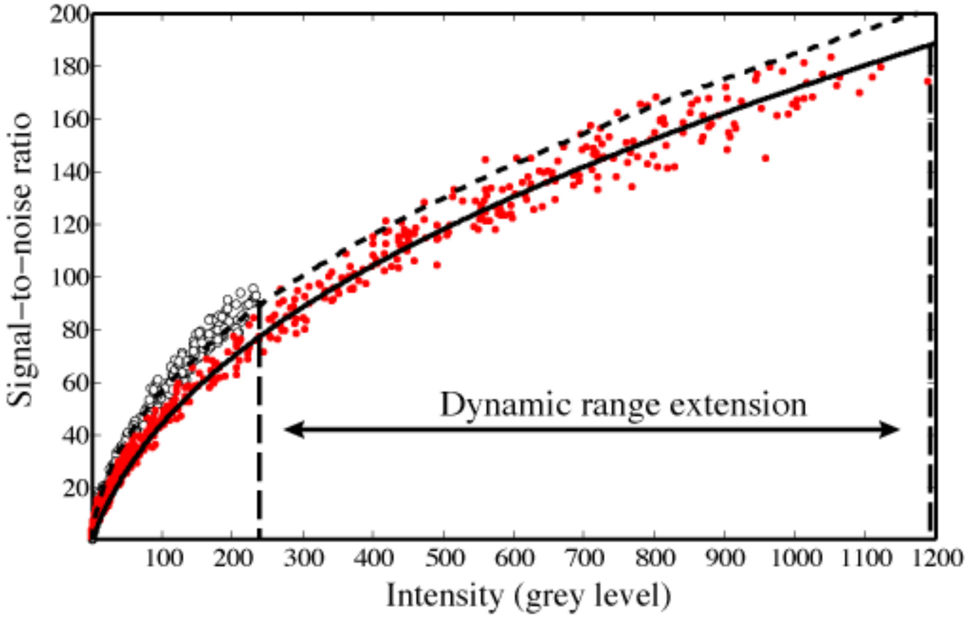

Figure 3-22: Signal-to-noise ratio (SNR) curves of microlens imaging system. White circles and red dots are SNR curves for superpixel sizes of N=1 and N=9 pixels, respectively. The dashed (solid) curve is a fit to the N=1 (N=9) data of the form SNR $= aI/\sqrt{aI + n_r^2}$, where a and n_r are fitting parameters and I is the pixel intensity (grey level). Dynamic range extension occurs for intensities (grey levels) lying between the vertical dashed lines.

Figure 3-22 shows a comparison between the SNR curves for superpixels of size N=1 and N=9 pixels. The N=9 curve shows lower SNR than the N=1 curve due to increased read noise arising from the use of 9 pixels. This property is captured by a model that accounts for shot noise $\sqrt{aI}$ and camera pixel read noise n_r: SNR $= aI/\sqrt{aI + {n_r}^2}$, where I is the signal intensity in grey level units (e.g. 0 to 255 for N=1) [12]. We fit this model to the data in Fig. 4, resulting in best fit parameters of $(a, n_r) = [(34.21, 13.64); (31.00, 41.97)]$ for N=1 and N=9 superpixels, respectively. For the N=9 fit we only use data points where every pixel in the superpixel has a grey level above 0. Pixels within a superpixel that contain no signal do not contribute to the overall noise because the read noise is below one grey level. As expected, we find that the read noise for an N=9 superpixel is 3.1-fold ($\sim\sqrt{9}$) higher than for the N=1 case, because noise sources within a superpixel add in quadrature.

At the top end of the dynamic range, the SNR is dictated by shot noise. Because an N=9 configuration can collect more photons before saturation, the maximum SNR is increased. We measure an 87% larger SNR for N=9 (SNR=174) than for N=1 (SNR=93) at the top of the dynamic range.

The dynamic range is also improved with the N=9 superpixel configuration. The largest unsaturated signal for N=9 takes a grey value of 1190 while the fitting results in Fig. 4 imply that the noise floor (SNR=1) is at a grey level of 1.37. The dynamic range of an N=9 superpixel is therefore 1190/1.37=868 (58.77 dB). For an N=1 superpixel, the dynamic range is limited to 255 (48.13 dB) by 8-bit digitization. The dynamic range for an N=9 superpixel is increased 3.4-fold (868/255) over the intrinsic dynamic range of the camera, from 8 bits to 9.76 bits. The increase in dynamic range comes with the caveat that it inherently occurs at higher signal levels – the extra bits come at the top end of dynamic range, as indicated by the dynamic range extension region in Figure 3-22.

For weakly fluorescent samples, imaging can become read noise dominated [12]. A superpixel of size N contributes $\sqrt{\mathrm{N}}$ times more read noise than a single pixel, modifying the SNR by a factor of $1/\sqrt{\mathrm{N}}$. Therefore, when sensitivity is paramount, it is optimal to reduce the magnification in order to direct all the photons from a single microlens to as few pixels as possible (small N). However, the magnification must be kept large enough to ensure that the images of the microlenses are still resolvable on the camera. The magnification can thus be tailored according to the nature of the sample in order to maximize either sensitivity or dynamic range.

3.6 Conclusions

We have developed three generations of a microlens array fluorescence microscope for HCS applications. The first prototype system demonstrated that high quality imaging was possible with the proposed configuration. Subsequent upgrades to the piezoelectric scanning stage, microlens array and laser source yielded significant improvement in pixel throughput and spectral flexibility. The current third-generation system is capable of imaging multiple fluorescent channels at up to 3 times the pixel throughput of commercial HCS systems. Future iterations of the microscope will be tested with real world HCS assays.

4 Light Field Moment Imaging

In the two dimensional (2D) representations of scenes captured by digital image sensors in conventional cameras and microscopes, depth information is discarded. Many applications, however, would benefit from an improved ability to record the three dimensional nature of the real world, and there are several techniques that aim to do so. In stereo imaging, the depths of points in a scene are determined from the disparity between two perspective views [149]. A method termed "shape from focus" extracts depth information from a focal stack of a scene, under the assumption that all objects are opaque [150]–[152]. In "light field imaging", both the intensity and direction of rays impinging on the image sensor are recorded [58], [111], [153]. This enables images to be formed post-capture in which properties such as viewing perspective, aperture size and focal plane position are varied. Light field imaging implementations, however, require significant modifications to conventional cameras and microscopes, e.g. the addition of a microlens array [58], [111] or an absorbing mask [125], [126].

We present a novel imaging technique in which the angular moments of light rays collected by an image sensor are determined. The angular moments are then used to reconstruct 3D perspective views of a scene. We call this light field moment imaging (LMI). Our method has the advantage that it only requires two images of a scene each obtained from a different focus position, and is implemented using conventional cameras and microscopes. Unlike stereo imaging and shape from focus techniques, which can also produce perspective views [154], [155], LMI makes no assumption as to the opacity of objects in the scene. LMI is therefore capable of producing 3D perspective views for partially absorbing objects, which are often encountered in biological microscopy. We present three examples of this method using common imaging systems and discuss further applications of LMI.

4.1 Theory

The light field function is a spatio-angular description of irradiance in the ray optics regime and can take on a number of parameterizations [56]. In this work we use the parameterization $\overline{L}(x, y, z, \tan\theta_X, \tan\theta_Y)$, representing the density of rays at a point (x, y, z), propagating in the direction specified by angles θ_x and θ_y (Figure 4-1a). This is equivalent to the two-plane parameterization introduced in Section 1.4.1. We have chosen to identify the z-coordinate explicitly in this Section because we will often be dealing with derivatives of image intensity along the z-direction.

The starting point for the development of LMI is to derive a continuity equation for the light field. Consider rays travelling through a box with side lengths $\Delta x, \Delta y$ and Δz. We assume that the box does not contain any optically absorbing or emitting materials. Furthermore, we assume that there are no refractive or diffractive interfaces, or scatterers of any kind within the box. This accurately describes the space between the imaging lens and sensor of an imaging system. With these restrictions, the net flux of optical energy through the box must be zero for any arbitrary ray direction. In other words, for a ray propagation direction given by the unit vector $\hat{n}_r$, we can write:

$$\begin{gathered}\overline{L}(x+\Delta x, y, z, \tan\theta_X, \tan\theta_Y)\langle \hat{n}_r \cdot \hat{x} \rangle \Delta y \Delta z - \overline{L}(x, y, z, \tan\theta_X, \tan\theta_Y)\langle \hat{n}_r \cdot \hat{x} \rangle \Delta y \Delta z + \\ \overline{L}(x, y+\Delta y, z, \tan\theta_X, \tan\theta_Y)\langle \hat{n}_r \cdot \hat{y} \rangle \Delta x \Delta z - \overline{L}(x, y, z, \tan\theta_X, \tan\theta_Y)\langle \hat{n}_r \cdot \hat{y} \rangle \Delta x \Delta z + \\ \overline{L}(x, y, z+\Delta z, \tan\theta_X, \tan\theta_Y)\langle \hat{n}_r \cdot \hat{z} \rangle \Delta x \Delta y - \overline{L}(x, y, z, \tan\theta_X, \tan\theta_Y)\langle \hat{n}_r \cdot \hat{z} \rangle \Delta x \Delta y = 0\end{gathered} \tag{4-1}$$

Where $\hat{x}, \hat{y}$ and $\hat{z}$ are the Cartesian unit vectors, and the angular brackets indicate a dot-product. Upon dividing both sides of Equation 4-1 by the volume of the box, and taking the limit as the box side lengths go to zero, we can write the following differential equation:

$$\frac{\partial \bar{L}}{\partial z}\langle \hat{n}_r \cdot \hat{z}\rangle = -\frac{\partial \bar{L}}{\partial x}\langle \hat{n}_r \cdot \hat{x}\rangle - \frac{\partial \bar{L}}{\partial y}\langle \hat{n}_r \cdot \hat{y}\rangle \tag{4-2}$$

To simplify further, we note that $\hat{n}_r = l^{-1}[\Delta z \tan\theta_X, \Delta z \tan\theta_Y, \Delta z]$, where l^{-1} is a normalization parameter. Substituting this relation into Equation 4-2, and defining $\mathbf{V} \overset{\text{def}}{=} [\tan\theta_X, \tan\theta_Y, 1]$, we obtain a continuity equation that can be written compactly as:

$$\nabla \cdot \left(\bar{L}\mathbf{V}\right) = 0 \tag{4-3}$$

Or equivalently,

$$\partial \bar{L}/\partial z = -\nabla_\perp \cdot \bar{L}[\tan\theta_X, \tan\theta_Y] \tag{4-4}$$

The intensity recorded by an ideal imaging system is related to the light field in object space via an integral over angular space: $I = \iint_{-\infty}^{\infty} \bar{L}(x, y, z, \tan\theta_X, \tan\theta_Y) R(\theta) \cos^4\theta \, d\tan\theta_X d\tan\theta_Y$, where θ is the angle between the ray and the image sensor normal and $R(\theta)$ captures the angular response of sensor pixels and illumination factors specific to the imaging system[1]. This is known as the $\cos^4\theta$ law [153], [156]. Typically, $R(\theta)\cos^4\theta$ is lumped in with the angular dependence of $\bar{L}$ to create a new "recorded" light field $L = \bar{L}R(\theta)\cos^4\theta$. This is the light field as seen at the image sensor plane in the camera, inclusive of vignetting and illumination factors. Following the light field literature we will work with the recorded light field L [153].

---

[1] For simplicity we have assumed unity magnification; non-unity magnification is introduced by scaling the spatial arguments of the light field.

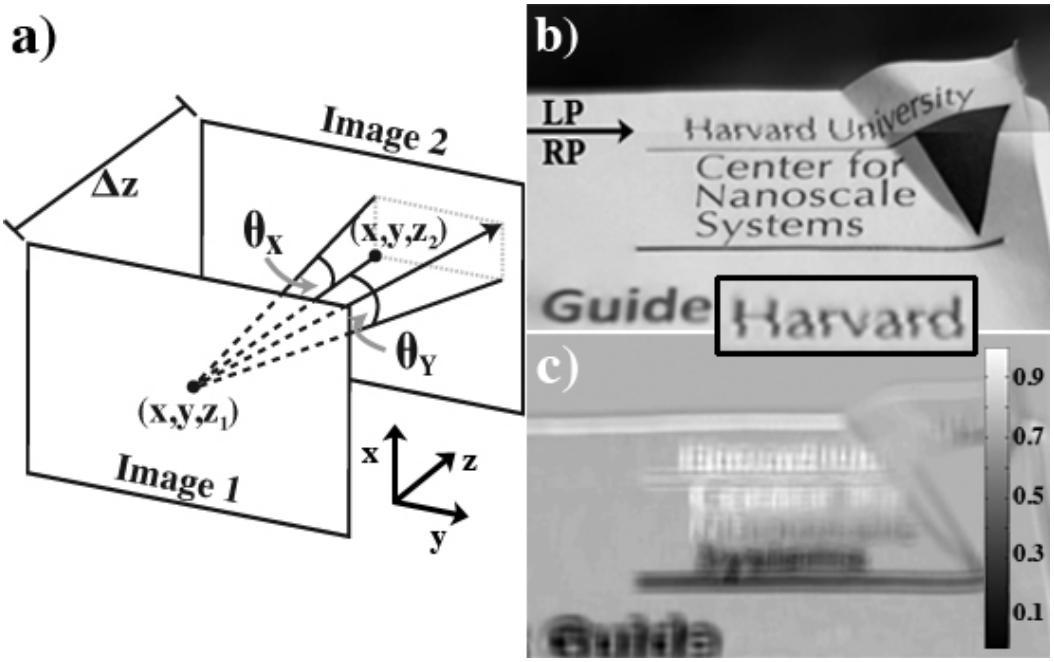

Figure 4-1 a) Schematic of the light field parameterization used. θ_X and θ_Y are defined by the projections of a ray onto the xz- and yz planes, respectively. b) A composite image of perspective views of a slanted sheet of paper as seen from horizontally displaced viewpoints. Below (above) the horizontal arrow is the right (left) perspective view, denoted by RP (LP). Inset: Note the mis-registration of the text "Harvard" at the border between the two views. This is a manifestation of parallax. A video of the viewpoint traveling horizontally is shown in Movie 4-1. c) Normalized depth map of the sheet with grayscale bar indicating depth. Normalized depth ranges from 0 (closest to camera) to 1 (farthest from camera).

Multiplying Equation 4-4 by $R(\theta)\cos^4\theta$ and integrating over angular space yields a Poisson Equation:

$$\partial I(x,y;z)/\partial z = -\nabla_{\perp}^{2} U(x,y;z) \qquad 4\text{-}5$$

Here, we have defined a scalar potential $U(x,y;z)$ by $\nabla U(x,y;z) = I(x,y;z)\mathbf{M}(x,y;z)$, where $\mathbf{M}(x,y;z) = [s(x,y;z), t(x,y;z)]$ is a vector containing the normalized first moments of the light field L over its angular coordinates:

$$[s,t] = \frac{\iint_{-\infty}^{\infty} L[\tan\theta_X,\tan\theta_Y] d\tan\theta_X d\tan\theta_Y}{\iint_{-\infty}^{\infty} L d\tan\theta_X d\tan\theta_Y} \tag{4-6}$$

Equation 4-5 is solved in Fourier space, and $\mathbf{M}$ is calculated via its relationship to $U(x,y;z)$ [157]. We implement this solution in MATLAB by applying a filter H to the approximate derivative calculated by taking the difference of the two input images $I_1 = I(x,y;z_1)$ and $I_2 = I(x,y;z_2)$ focused at different planes:

$$H(f_x, f_y) = [-4\pi^2(f_x^2 + f_y^2)]^{-1} \text{ for } (f_x^2 + f_y^2) \neq 0 \tag{4-7}$$

$$H(f_x, f_y) = 1 \text{ for } (f_x^2 + f_y^2) = 0 \tag{4-8}$$

$$U = \mathrm{IFT}[\mathrm{H}\times\mathrm{FT}\{(I_1 - I_2)/\Delta z\}] \tag{4-9}$$

Where FT and IFT denote the Fourier transform and its inverse, respectively; f_x and f_y are the spatial frequencies in the x- and y-directions, respectively, and $\Delta z = z_1 - z_2$. The moment vector field $\mathbf{M}$ is then calculated by applying the MATLAB gradient function to U and dividing the result by $(I_1 + I_2)/2$:

$$\mathbf{M} = \frac{2}{I_1 + I_2}\nabla_\perp U \tag{4-10}$$

In cases where the defocus distance Δz between images is not accessible (for example with an SLR camera), we take an arbitrary value for Δz and then normalize $\mathbf{M}$ by its maximum magnitude value. In these cases, we extract normalized ray light field moments, but not their absolute values. This has no effect on the 3D visualizations shown in this work.

We construct an approximation to the light field of the scene at z_1 by assuming that the angular distribution of rays is Gaussian with mean $[s(x,y), t(x,y)]$:

$$L(x,y,u,v) = I_1(x,y)\exp\{-[u - s(x,y)]^2/\sigma^2 - [u - t(x,y)]^2/\sigma^2\} \qquad \text{4-11}$$

Where we empirically set $\sigma = \mathrm{NA}^2$ and we have dropped z_1 for convenience. We have found that this σ value gives a good perspective shifting effect. Further investigation is needed to understand and improve on this Gaussian assumption. This could be the subject of future research. The Gaussian assumption enables the reconstruction of a scene as viewed at different perspectives by choosing 2D slices of the light field in Equation 4-11 at a given (u,v) coordinate [153].

4.2 Light Field Moment Photography

As a first example of this technique, we photograph a bent sheet of paper with a grayscale digital camera (Basler acA2000-340km) equipped with a single lens reflex lens (50 mm focal length, f/1.4). A pair of images is recorded while slightly adjusting the plane of focus between photographs. Using the difference between these images to approximate the left hand side of Equation 4-5, we solve the Poisson equation and construct as in Equation 4-9. Finally, we extract perspective views of the sheet at different positions along the horizontal axis, as shown in Figure 4-1b. Parallax manifests itself apparent movement of features when the viewpoint is changed.

This can be seen in the inset to Figure 4-1b, where text in the image is translated when viewed from viewpoints that are displaced horizontally. When viewed as an animation where the viewpoint travels horizontally in Movie 4-1, our brain efficiently processes the temporal sequence and can easily recognize depth within the image [158]. The sheet is slanted such that the top the paper is farther away from the camera than the bottom. One can also use the light field created with Equation 4-11 to calculate a depth map. Depth maps based on disparity assign a depth value to each pixel based on the amount displacement of a feature between images taken from different viewpoints [119], [149]. We use a plenoptic depth-mapping algorithm to produce the depth map depicted in Figure 4-1c [119]. As is expected, the depth map indicates that the bottom of the sheet is closer to the camera than the top. Areas of the image without features – such as blank areas of the page – do not return proper depth values. This is typical of depth mapping algorithms that rely on disparity [119].

4.3 Light Field Moment Microscopy

Viewpoint synthesis can also be performed with images acquired using a microscope. Optical microscopes are particularly well suited to recording focal stacks because they are equipped with a stage that translates along the optical axis. We image a tissue micro array section (US Biomax BLSC 1501) using an optical microscope operated in transmission mode, with a $10\times$, 0.3NA objective and fitted with a color digital camera; a micrograph of the tissue sample is shown in Figure 4-2a. We proceed with the same image-processing scheme as outlined above, for each color channel separately. The tissue section has been folded upon itself such that it has an appreciable 3D structure. We used two input images focused at planes separated by $\Delta z = 6\ \mu m$ in object space. An animation of the tissue section as seen from a viewpoint travelling along the vertical axis is shown in Movie 4-2. To further showcase the ability of LMI to create perspective shifted images of complex translucent samples, we imaged the head of a wood tick (Dermacentor variabilis, Carolina Biological Supply) at two planes separated by $\Delta z = 5\ \mu m$. We use the sample microscope and objective as above. A micrograph of the tick head and an animation showing the reconstructed perspective views are shown as Figure 4-2b and Movie 4-3, respectively. Reconstruction of perspective views using a depth map would be impossible in this partially transparent sample because a single depth value cannot be assigned to a given position in the image [154].

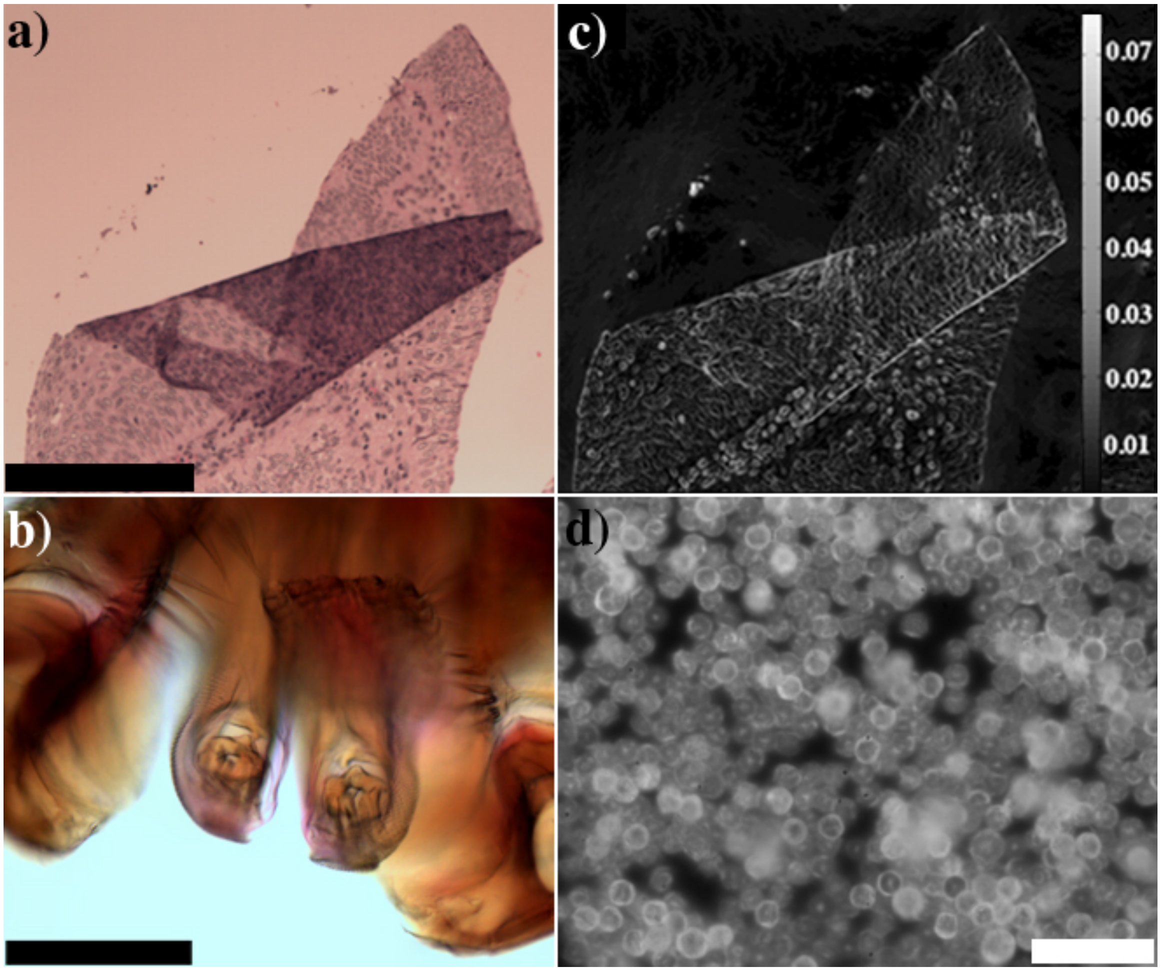

Figure 4-2 a) Micrograph of a folded tissue slice. Scale bar is 200 μm. A perspective-shifting animation of the tissue slice is shown in Movie 4-2. b) Micrograph of the head of a wood tick. Scale bar is 200 μm. A perspective-shifting animation of the wood tick head is shown in Movie 4-3. c) Grayscale plot of the magnitude of the moment vector field M for the tissue sample in a). The grayscale bar shows the unitless value of |M|. d) Micrograph of a pile of 5 μm fluorescent beads. Scale bar is 25 μm. A perspective-shifting animation of this sample is shown in Movie 4-4.

In addition to perspective shifting, one can construct an image similar to a dark field micrograph by plotting the magnitude of $\mathbf{M}$, as shown in Figure 4-2c. Because the microscope uses Kohler illumination, which is symmetric about the optical axis, we expect that $|\mathbf{M}| = 0$ in the absence of scatterers. Indeed, this is observed away from the tissue section. However, small features such as cells tend to scatter strongly and anisotropically. Therefore these localized scattering features give rise to large $|\mathbf{M}|$ values and appear bright in Figure 4-2c. The maximum $|\mathbf{M}|$ value is limited by the NA of the microscope objective. In Figure 4-2c, $|\mathbf{M}| < 0.08$, which is consistent with our expectation that $|\mathbf{M}| < \tan\,[\sin^{-1} 0.3]$=0.31.

LMI can also be used in fluorescence microscopy. To demonstrate this, we image a pile of 5 μm fluorescent beads (Invitrogen) with a $50\times$, 0.55 NA microscope objective. A 532 nm laser is used to excite the fluorescence and a long pass filter is placed in front of the Basler camera so that the image sensor only collects the fluorescent emission from the beads. A micrograph of the sample along with a perspective shifting animation is shown as Figure 4-2d (Movie 4-4). Again, parallax is apparent in the animation.

Noise amplification at low spatial frequencies occurs due to the Fourier filter (Equations 4-7 and 4-8) that is used to solve the Poisson Equation. If the two images used are too closely spaced, this noise can dominate the solution to the Poisson Equation [159]. This problem has been studied extensively in the phase imaging literature [157], [159]–[161]. This problem could be mitigated in a number of ways, for example by capturing more images to cut down on noise [157], or by blending together perspective images constructed using pairs of images of different axial separations [159]. In Movies 4-2 and 4-3, noise manifests itself as coloration in the perspective images. This is because of noisy low spatial frequency modes in the perspective images that vary between color channels. The result is the emergence of patches of false colors, which are especially prominent in areas dominated by low spatial frequency features.

4.4 Conclusions

We have shown how a continuity equation for light fields can be exploited to calculate the first angular moments of a light using a pair of input images. With these moments, we can reconstruct perspective-shifted views of the original scene under the empirical assumption that the angular distribution of the light field is Gaussian. Depth maps and dark-field-like microscope images can also be extracted with LMI. Our approach is versatile, as we have demonstrated it on three different imaging systems ranging from photographic cameras to microscopes. LMI enables convenient three-dimensional perspective imaging in systems where light field sensors might be impractical such as high-resolution microscopes and mobile phone and infrared cameras. In microscopy, LMI could prove useful as a low dose alternative to confocal fluorescence microscopy. In cinematography, LMI might be an efficient way to capture next generation three-dimensional media for light field displays [162]. We expect that this technique will be applicable to more exotic focused imaging systems that obey the ray approximation, such as transmission electron microscopes.

5 Conclusions and Future Work

A significant knowledge base in the areas of micro optics, microfluidics, fluorescence imaging and light field imaging has been developed while undertaking the work presented in this thesis. Three main research directions were investigated within the broad scope of optical imaging. First, a spatially resolved and integrated micro optical pressure sensor was developed for use in microfluidic devices. These pressure sensors were used to visualize pressure distributions throughout microfluidic chips. Next, a novel microscope architecture for HCS was designed and realized in three successive iterations. In its current form, this microscope yields up to 3 times the throughput of commercial automated fluorescence microscopes, and is capable of imaging multiple fluorescent channels either sequentially or in parallel. This system has captured the attention of Thermo Scientific, with whom we are now in collaboration to develop the system further. Together with Thermo Scientific, we plan to perform a feasibility study for HCS using our microlens array microscope. Lastly, a novel imaging technique called light field moment imaging (LMI) was realized. The redistribution of light rays between the two images is related to the average (first moment) ray angle at each spatial position. With this connection in mind, we extract the average ray angle at each spatial position of various photographs and micrographs. We showed that this data can be processed to extract estimations of the scene as viewed from different perspectives. With the help of the Harvard SEAS Communications Office, this work garnered significant press coverage, including a YouTube video with over 31,000 views as of March 2014 [163]. Future directions in this area are single shot capture of the two required images for LMI. This would push the technique to video rate for applications in cinematography.

6 Research Highlights

6.1 Micro Optical Pressure Sensing

- Developed the first 2D pressure measurement scheme for microfluidics.

6.2 High Throughput Microlens Microscopy

- Demonstrated a novel fluorescence microscope architecture that significantly outpaces the current state-of-the-art commercial automated microscopes.
- First report of a point scanning light field imaging configuration.
- Attracted a development grant from one of the world's largest lab equipment companies (Thermo Scientific) to investigate commercializing the microlens microscope.

6.3 Light Field Moment Imaging

- Introduced a light field continuity equation that has not (to the author's knowledge) been published before by the 3D imaging community.
- First demonstration of viewpoint manipulation using off-the-shelf single aperture imaging systems.
- Significant dissemination:
    - Reported on by over 20 online and print outlets in 8 countries.
    - Over 31,000 YouTube views of press release video.
    - Most downloaded Optics Letters manuscript for 3 months in a row (August to October 2013); 2nd most downloaded in November 2013 and 4th most downloaded in December 2013.

7 Publication List

7.1 Journal Publications

1. “Multiplexed pressure sensing with elastomer membranes,” **Antony Orth**, Ethan Schonbrun and Kenneth B. Crozier, Lab Chip vol.11, pp.3810-3815 (2011).

2. "Microscopy with microlens arrays: high throughput, high resolution and light-field imaging," **Antony Orth** and Kenneth B. Crozier, Optics Express vol. 20, pp.13522-13531 (2012).

3. “Measuring the pressures across microfluidic droplets with an optical tweezer,” Yuhang Jin, **Antony Orth**, Ethan Schonbrun and Kenneth B. Crozier, Optics Express vol. 20, pp.24450-24464 (2012).

4. "Gigapixel fluorescence microscopy with a water immersion microlens array," **Antony Orth** and Kenneth B. Crozier, Optics Express vol. 21, pp.2361-2368 (2013) .

5. “Light field moment imaging,” **Antony Orth** and Kenneth B. Crozier, Optics Letters vol. 38, pp.2666-2668 (2013).

6. “High throughput multichannel fluorescence microscopy with microlens arrays,” **Antony Orth** and Kenneth B. Crozier, *in preparation.*

7.2 Conference Proceedings

1. “Self-Assembled Diffraction Grating for Microfluidic Velocimetry,” **Antony Orth**, Ethan Schonbrun, Kenneth B. Crozier, Frontiers in Optics, FTuH3 (2009).

2. “Elastomer membrane pressure sensors for microfluidics,” **Antony Orth**, Ethan Schonbrun, Kenneth B. Crozier, microTAS. Groningen, Netherlands, 1994-1996 (2010).

3. “Scanning Confocal Microscopy With A Microlens Array,” **Antony Orth**, Kenneth B. Crozier, Frontiers in Optics, FWS7 (2011).

4. “High Throughput Microscopy With a Microlens Array,” **Antony Orth**, Kenneth B. Crozier, CLEO: Science and Innovations, CTu3J. 2 (2012).

5. “Light Field Moment Imaging,” **Antony Orth** and Kenneth B. Crozier, Computational Optical Sensing and Imaging, CM4C.5 (2013).

8 References

[1] A. Orth, E. F. Schonbrun, and K. B. Crozier, “Elastomer membrane pressure sensors for microfluidics,” *microTAS. Groningen, Netherlands*, pp. 1994–1996, 2010.

[2] A. Orth, E. Schonbrun, and K. B. Crozier, “Multiplexed pressure sensing with elastomer membranes,” *Lab on a Chip*, vol. 11, no. 22, pp. 3810–3815, 2011.

[3] E. Schonbrun, A. R. Abate, P. E. Steinvurzel, D. A. Weitz, and K. B. Crozier, “High-throughput fluorescence detection using an integrated zone-plate array,” *Lab on a Chip*, vol. 10, no. 7, pp. 852–856, 2010.

[4] A. Orth and K. B. Crozier, “Scanning Confocal Microscopy With A Microlens Array,” in *Frontiers in Optics*, 2011.

[5] A. Orth and K. Crozier, “Microscopy with microlens arrays: high throughput, high resolution and light-field imaging,” *Opt. Express 20 (12)*, pp. 13522–13531, 2012.

[6] A. Orth and K. Crozier, “Gigapixel fluorescence microscopy with a water immersion microlens array,” *Optics express*, vol. 21, no. 2, pp. 2361–2368, 2013.

[7] A. G. Orth and K. B. Crozier, “Light Field Moment Imaging,” in *Computational Optical Sensing and Imaging (COSI)*, *Arlington, VA*, CM4C.5, 2013.

[8] A. Orth and K. B. Crozier, “Light field moment imaging,” *Opt. Lett.*, vol. 38, no. 15, pp. 2666–2668, Aug. 2013.

[9] A. Orth and K. Crozier, “High throughput microscopy with a microlens array,” in *Lasers and Electro-Optics (CLEO), 2012 Conference on*, 2012, pp. 1–2.

[10] “Fluorescence Microscope Wikipedia Page: http://en.wikipedia.org/wiki/Fluorescence_microscope.” .

[11] J. W. Lichtman and J.-A. Conchello, “Fluorescence microscopy,” *Nat Meth*, vol. 2, no. 12, pp. 910–919, Dec. 2005.

[12] J. Pawley, *Handbook of biological confocal microscopy*. Springer, 2006.

[13] J.-A. Conchello and J. W. Lichtman, “Optical sectioning microscopy,” *Nature methods*, vol. 2, no. 12, pp. 920–931, 2005.

[14] M. Gu, *Principles of Three Dimensional Imaging in Confocal Microscopes*. World Scientific, 1996.

[15] E. Wang, C. M. Babbey, and K. W. Dunn, “Performance comparison between the high-speed Yokogawa spinning disc confocal system and single-point scanning confocal systems,” *Journal of microscopy*, vol. 218, no. 2, pp. 148–159, 2005.

[16] S. A. Haney, *High Content Screening: Science, Techniques and Applications*. John Wiley & Sons, 2008.

[17] M. Bickle, "The beautiful cell: high-content screening in drug discovery," *Analytical and bioanalytical chemistry*, vol. 398, no. 1, pp. 219–226, 2010.

[18] John Ringeling, "Personal Communication. John RIngeling, Millenium Pharmaceuticals. 1 March 2013."

[19] Molecular Devices, "Complete Imaging Solution Brochure, http://www.moleculardevices.com/Products/Instruments/High-Content-Screening/ImageXpress-Micro.html." .

[20] P. Gribbon and A. Sewing, "Fluorescence readouts in HTS: no gain without pain?," *Drug discovery today*, vol. 8, no. 22, pp. 1035–1043, 2003.

[21] S. Michael, D. Auld, C. Klumpp, A. Jadhav, W. Zheng, N. Thorne, C. P. Austin, J. Inglese, and A. Simeonov, "A robotic platform for quantitative high-throughput screening," *Assay and drug development technologies*, vol. 6, no. 5, pp. 637–657, 2008.

[22] K. Korn and E. Krausz, "Cell-based high-content screening of small-molecule libraries," *Current opinion in chemical biology*, vol. 11, no. 5, pp. 503–510, 2007.

[23] Olympus, "Scan^R High-content screening station for life sciences website, http://www.olympus-europa.com/microscopy/en/microscopy/components/component_details/component_detail_21320.jsp." .

[24] A. E. Carpenter, T. R. Jones, M. R. Lamprecht, C. Clarke, I. H. Kang, O. Friman, D. A. Guertin, J. H. Chang, R. A. Lindquist, and J. Moffat, "CellProfiler: image analysis software for identifying and quantifying cell phenotypes," *Genome biology*, vol. 7, no. 10, p. R100, 2006.

[25] F. Zanella, J. B. Lorens, and W. Link, "High content screening: seeing is believing," *Trends in biotechnology*, vol. 28, no. 5, pp. 237–245, 2010.

[26] Ibidi, "96-well microplate instructions, http://ibidi.com/fileadmin/products/labware/plates/P_8962X_Plate_96well/IN_8962X_96well.pdf?x9c41f=2b898339f12837478177c69eb3d6c009." .

[27] "Hammatsu Cameras Website, http://www.hamamatsu.com/us/en/product/category/5000/5005/index.html." .

[28] "Andor Cameras Website, http://www.andor.com/scientific-cameras." .

[29] G. Zheng, X. Ou, and C. Yang, "0.5 gigapixel microscopy using a flatbed scanner," *Biomed. Opt. Express*, vol. 5, no. 1, pp. 1–8, Jan. 2014.

[30] A. W. Lohmann, R. G. Dorsch, D. Mendlovic, Z. Zalevsky, and C. Ferreira, “Space-bandwidth product of optical signals and systems,” *J. Opt. Soc. Am. A*, vol. 13, no. 3, pp. 470–473, Mar. 1996.

[31] A. W. Lohmann, “Scaling laws for lens systems,” *Applied optics*, vol. 28, no. 23, pp. 4996–4998, 1989.

[32] S. Yazdanfar, K. B. Kenny, K. Tasimi, A. D. Corwin, E. L. Dixon, and R. J. Filkins, “Simple and robust image-based autofocusing for digital microscopy,” *Optics express*, vol. 16, no. 12, pp. 8670–8677, 2008.

[33] M. C. Montalto, R. R. McKay, and R. J. Filkins, “Autofocus methods of whole slide imaging systems and the introduction of a second-generation independent dual sensor scanning method,” *J Pathol Inform*, vol. 2, Oct. 2011.

[34] Thorlabs, “MLS203-1 Fast XY Scanning Stage User Guide, http://www.thorlabs.com/thorcat/20900/MLS203-1-Manual.pdf.” .

[35] Molecular Devices, “ImageXpress Micro XL Brochure, http://info.moleculardevices.com/acton/formfd/2560/0052:d-00a4.” .

[36] M. E. Bravo-Zanoguera, C. A. Laris, L. K. Nguyen, M. Oliva, and J. H. Price, “Dynamic autofocus for continuous-scanning time-delay-and-integration image acquisition in automated microscopy,” *J. Biomed. Opt*, vol. 12, no. 3, pp. 034011–034011–16, 2007.

[37] P. B. Catrysse and B. A. Wandell, “Roadmap for CMOS image sensors: Moore meets Planck and Sommerfeld,” 2005, vol. 5678, pp. 1–13.

[38] I. Abramovich, “Color image sensor with embedded microlens array,” 6,362,498Mar-2002.

[39] B.-K. Lee, D. S. Kim, and T. H. Kwon, “Replication of microlens arrays by injection molding,” *Microsystem Technologies*, vol. 10, no. 6–7, pp. 531–535, 2004.

[40] Q. Peng, Y. Guo, S. Liu, and Z. Cui, “Real-time gray-scale photolithography for fabrication of continuous microstructure,” *Optics letters*, vol. 27, no. 19, pp. 1720–1722, 2002.

[41] M. R. Wang and H. Su, “Laser direct-write gray-level mask and one-step etching for diffractive microlens fabrication,” *Applied optics*, vol. 37, no. 32, pp. 7568–7576, 1998.

[42] D. Daly, *Microlens Arrays*. CRC Press, 2000.

[43] C.-F. Chen, S.-D. Tzeng, H.-Y. Chen, and S. Gwo, “Silicon microlens structures fabricated by scanning-probe gray-scale oxidation,” *Optics letters*, vol. 30, no. 6, pp. 652–654, 2005.

[44] A. Braun, K. Zimmer, B. Hösselbarth, J. Meinhardt, F. Bigl, and R. Mehnert, “Excimer laser micromachining and replication of 3D optical surfaces,” *Applied surface science*, vol. 127, pp. 911–914, 1998.

[45] J.-W. Pan, C.-M. Wang, H.-C. Lan, W.-S. Sun, and J.-Y. Chang, “Homogenized LED-illumination using microlens arrays for a pocket-sized projector,” *Opt. Express*, vol. 15, no. 17, pp. 10483–10491, 2007.

[46] J.-H. Lee, Y.-H. Ho, K.-Y. Chen, H.-Y. Lin, J.-H. Fang, S.-C. Hsu, J.-R. Lin, and M.-K. Wei, “Efficiency improvement and image quality of organic light-emitting display by attaching cylindrical microlens arrays,” *Opt. Express*, vol. 16, no. 26, pp. 21184–21190, Dec. 2008.

[47] J.-S. Jang and B. Javidi, “Improved viewing resolution of three-dimensional integral imaging by use of nonstationary micro-optics,” *Opt. Lett.*, vol. 27, no. 5, pp. 324–326, Mar. 2002.

[48] X.-H. Lee, I. Moreno, and C.-C. Sun, “High-performance LED street lighting using microlens arrays,” *Opt. Express*, vol. 21, no. 9, pp. 10612–10621, May 2013.

[49] A. El Gamal, “Trends in CMOS image sensor technology and design,” in *Electron Devices Meeting, 2002. IEDM’02. International*, 2002, pp. 805–808.

[50] A. El Gamal and H. Eltoukhy, “CMOS image sensors,” *Circuits and Devices Magazine, IEEE*, vol. 21, no. 3, pp. 6–20, 2005.

[51] K. Tvingstedt, S. Dal Zilio, O. Inganńs, and M. Tormen, “Trapping light with micro lenses in thin film organic photovoltaic cells,” *Optics Express*, vol. 16, no. 26, pp. 21608–21615, 2008.

[52] T. Tanaami, S. Otsuki, N. Tomosada, Y. Kosugi, M. Shimizu, and H. Ishida, “High-speed 1-frame/ms scanning confocal microscope with a microlens and Nipkow disks,” *Applied Optics*, vol. 41, no. 22, pp. 4704–4708, 2002.

[53] J. Bewersdorf, R. Pick, and S. W. Hell, “Multifocal multiphoton microscopy,” *Optics letters*, vol. 23, no. 9, pp. 655–657, 1998.

[54] K. Stollberg, A. Brückner, J. Duparré, P. Dannberg, A. Bräuer, and A. Tünnermann, “The Gabor superlens as an alternative wafer-level camera approach inspired by superposition compound eyes of nocturnal insects,” *Optics express*, vol. 17, no. 18, pp. 15747–15759, 2009.

[55] J. Duparre, P. Schreiber, and R. Volkel, “Theoretical analysis of an artificial superposition compound eye for application in ultra flat digital image acquisition devices,” in *Optical Systems Design*, 2004, pp. 408–418.

[56] M. Levoy, Z. Zhang, and I. McDowall, “Recording and controlling the 4D light field in a microscope using microlens arrays,” *Journal of Microscopy*, vol. 235, no. 2, pp. 144–162, 2009.

[57] H. Arimoto and B. Javidi, “Integral three-dimensional imaging with digital reconstruction,” *Optics letters*, vol. 26, no. 3, pp. 157–159, 2001.

[58] R. Ng, M. Levoy, M. Brédif, G. Duval, M. Horowitz, and P. Hanrahan, “Light field photography with a hand-held plenoptic camera,” *Computer Science Technical Report CSTR*, vol. 2, no. 11, 2005.

[59] M. Harris, “Focusing on everything,” *Spectrum, IEEE*, vol. 49, no. 5, pp. 44–50, 2012.

[60] M. Ares, S. Royo, and J. Caum, “Shack-Hartmann sensor based on a cylindrical microlens array,” *Optics letters*, vol. 32, no. 7, pp. 769–771, 2007.

[61] G. E. Artzner, “Microlens arrays for Shack-Hartmann wavefront sensors,” *Optical Engineering*, vol. 31, no. 6, pp. 1311–1322, 1992.

[62] J. Primot, “Theoretical description of Shack–Hartmann wave-front sensor,” *Optics Communications*, vol. 222, no. 1, pp. 81–92, 2003.

[63] E. Schonbrun, P. E. Steinvurzel, and K. B. Crozier, “A microfluidic fluorescence measurement system using an astigmatic diffractive microlens array,” *Opt. Express*, vol. 19, no. 2, pp. 1385–1394, 2011.

[64] A. Schilling, R. Merz, C. Ossmann, and H. P. Herzig, “Surface profiles of reflow microlenses under the influence of surface tension and gravity,” *Optical Engineering*, vol. 39, no. 8, pp. 2171–2176, 2000.

[65] N. Chronis, G. L. Liu, K.-H. Jeong, and L. P. Lee, “Tunable liquid-filled microlens array integrated with microfluidic network,” *Opt. Express*, vol. 11, no. 19, pp. 2370–2378, 2003.

[66] L. Miccio, A. Finizio, S. Grilli, V. Vespini, M. Paturzo, S. De Nicola, and P. Ferraro, “Tunable liquid microlens arrays in electrode-less configuration and their accurate characterization by interference microscopy,” *Opt. Express*, vol. 17, no. 4, pp. 2487–2499, Feb. 2009.

[67] K. Campbell, Y. Fainman, and A. Groisman, “Pneumatically actuated adaptive lenses with millisecond response time,” *Applied Physics Letters*, vol. 91, no. 17, p. 171111, Oct. 2007.

[68] A. Werber and H. Zappe, “Tunable pneumatic microoptics,” *Microelectromechanical Systems, Journal of*, vol. 17, no. 5, pp. 1218–1227, 2008.

[69] H. Yang, C.-K. Chao, M.-K. Wei, and C.-P. Lin, “High fill-factor microlens array mold insert fabrication using a thermal reflow process,” *Journal of micromechanics and microengineering*, vol. 14, no. 8, p. 1197, 2004.

[70] P. Nussbaum, R. Voelkel, H. P. Herzig, M. Eisner, and S. Haselbeck, “Design, fabrication and testing of microlens arrays for sensors and microsystems,” *Pure and Applied Optics: Journal of the European Optical Society Part A*, vol. 6, no. 6, p. 617, 1997.

[71] R. Guo, S. Xiao, X. Zhai, J. Li, A. Xia, and W. Huang, “Micro lens fabrication by means of femtosecond two photon photopolymerization,” *Optics Express*, vol. 14, no. 2, pp. 810–816, 2006.

[72] M. Malinauskas, H. Gilbergs, A. \vZukauskas, V. Purlys, D. Paipulas, and R. Gadonas, “A femtosecond laser-induced two-photon photopolymerization technique for structuring microlenses,” *Journal of optics*, vol. 12, no. 3, p. 035204, 2010.

[73] K. Naessens, H. Ottevaere, R. Baets, P. Van Daele, and H. Thienpont, “Direct writing of microlenses in polycarbonate with excimer laser ablation,” *Applied optics*, vol. 42, no. 31, pp. 6349–6359, 2003.

[74] H. Liu, F. Chen, X. Wang, Q. Yang, D. Zhang, J. Si, and X. Hou, “Photoetching of spherical microlenses on glasses using a femtosecond laser,” *Optics Communications*, vol. 282, no. 20, pp. 4119–4123, 2009.

[75] T. R. Jay and M. B. Stern, “Preshaping photoresist for refractive microlens fabrication,” *Optical Engineering*, vol. 33, no. 11, pp. 3552–3555, 1994.

[76] H. Wu, T. W. Odom, and G. M. Whitesides, “Reduction photolithography using microlens arrays: applications in gray scale photolithography,” *Analytical chemistry*, vol. 74, no. 14, pp. 3267–3273, 2002.

[77] K. Totsu, K. Fujishiro, S. Tanaka, and M. Esashi, “Fabrication of three-dimensional microstructure using maskless gray-scale lithography,” *Sensors and Actuators A: Physical*, vol. 130, pp. 387–392, 2006.

[78] M.-H. Wu, C. Park, and G. M. Whitesides, “Fabrication of arrays of microlenses with controlled profiles using gray-scale microlens projection photolithography,” *Langmuir*, vol. 18, no. 24, pp. 9312–9318, 2002.

[79] M. V. Kunnavakkam, F. M. Houlihan, M. Schlax, J. A. Liddle, P. Kolodner, O. Nalamasu, and J. A. Rogers, “Low-cost, low-loss microlens arrays fabricated by soft-lithography replication process,” *Applied physics letters*, vol. 82, no. 8, pp. 1152–1154, 2003.

[80] T.-K. Shin, J.-R. Ho, and J.-W. Cheng, “A new approach to polymeric microlens array fabrication using soft replica molding,” *Photonics Technology Letters, IEEE*, vol. 16, no. 9, pp. 2078–2080, 2004.

[81] Y. Xia, E. Kim, X.-M. Zhao, J. A. Rogers, M. Prentiss, and G. M. Whitesides, “Complex optical surfaces formed by replica molding against elastomeric masters,” *Science*, vol. 273, no. 5273, pp. 347–349, 1996.

[82] L.-T. Jiang, T.-C. Huang, C.-R. Chiu, C.-Y. Chang, and S.-Y. Yang, “Fabrication of plastic microlens arrays using hybrid extrusion rolling embossing with a metallic cylinder mold fabricated using dry film resist,” *Optics Express*, vol. 15, no. 19, pp. 12088–12094, 2007.

[83] C. Y. Chang, S. Y. Yang, and J. L. Sheh, “A roller embossing process for rapid fabrication of microlens arrays on glass substrates,” *Microsystem technologies*, vol. 12, no. 8, pp. 754–759, 2006.

[84] P.-H. Huang, T.-C. Huang, Y.-T. Sun, and S.-Y. Yang, “Fabrication of large area resin microlens arrays using gas-assisted ultraviolet embossing,” *Opt. Express*, vol. 16, no. 5, pp. 3041–3048, Mar. 2008.

[85] T. Thorsen, S. J. Maerkl, and S. R. Quake, “Microfluidic large-scale integration,” *Science*, vol. 298, no. 5593, pp. 580–584, 2002.

[86] S. R. Quake and A. Scherer, “From Micro- to Nanofabrication with Soft Materials,” *Science*, vol. 290, no. 5496, pp. 1536–1540, Nov. 2000.

[87] D. C. Duffy, J. C. McDonald, O. J. Schueller, and G. M. Whitesides, “Rapid prototyping of microfluidic systems in poly (dimethylsiloxane),” *Analytical chemistry*, vol. 70, no. 23, pp. 4974–4984, 1998.

[88] M. A. Unger, H.-P. Chou, T. Thorsen, A. Scherer, and S. R. Quake, “Monolithic microfabricated valves and pumps by multilayer soft lithography,” *Science*, vol. 288, no. 5463, pp. 113–116, 2000.

[89] L. Wang, M. Zhang, M. Yang, W. Zhu, J. Wu, X. Gong, and W. Wen, “Polydimethylsiloxane-integratable micropressure sensor for microfluidic chips,” *Biomicrofluidics*, vol. 3, p. 034105, 2009.

[90] K. Chung, H. Lee, and H. Lu, “Multiplex pressure measurement in microsystems using volume displacement of particle suspensions,” *Lab on a Chip*, vol. 9, no. 23, pp. 3345–3353, 2009.

[91] M. J. Kohl, S. I. Abdel-Khalik, S. M. Jeter, and D. L. Sadowski, “A microfluidic experimental platform with internal pressure measurements,” *Sensors and Actuators A: Physical*, vol. 118, no. 2, pp. 212–221, 2005.

[92] N. Srivastava and M. A. Burns, “Microfluidic pressure sensing using trapped air compression,” *Lab on a Chip*, vol. 7, no. 5, pp. 633–637, 2007.

[93] M. Abkarian, M. Faivre, and H. A. Stone, “High-speed microfluidic differential manometer for cellular-scale hydrodynamics,” *Proceedings of the National Academy of Sciences of the United States of America*, vol. 103, no. 3, pp. 538–542, 2006.

[94] K. Hosokawa, K. Hanada, and R. Maeda, “A polydimethylsiloxane (PDMS) deformable diffraction grating for monitoring of local pressure in microfluidic devices,” *Journal of Micromechanics and Microengineering*, vol. 12, no. 1, p. 1, 2002.

[95] W. Song and D. Psaltis, “Optofluidic pressure sensor based on interferometric imaging,” *Optics letters*, vol. 35, no. 21, pp. 3604–3606, 2010.

[96] W. Song and D. Psaltis, “Imaging based optofluidic air flow meter with polymer interferometers defined by soft lithography,” *Opt. Express*, vol. 18, no. 16, pp. 16561–16566, 2010.

[97] B. K. Wunderlich, U. A. Kleßinger, and A. R. Bausch, “Diffusive spreading of time-dependent pressures in elastic microfluidic devices,” *Lab on a Chip*, vol. 10, no. 8, pp. 1025–1029, 2010.

[98] B. A. Grzybowski, S. T. Brittain, and G. M. Whitesides, “Thermally actuated interferometric sensors based on the thermal expansion of transparent elastomeric media,” *Review of scientific instruments*, vol. 70, no. 4, pp. 2031–2037, 1999.

[99] D. J. Beebe, J. S. Moore, J. M. Bauer, Q. Yu, R. H. Liu, C. Devadoss, and B.-H. Jo, “Functional hydrogel structures for autonomous flow control inside microfluidic channels,” *Nature*, vol. 404, no. 6778, pp. 588–590, 2000.

[100] S. Calixto, F. J. Sanchez-Marin, and M. Rosete-Aguilar, “Pressure sensor with optofluidic configuration,” *Applied Optics*, vol. 47, no. 35, pp. 6580–6585, 2008.

[101] S. Timoshenko, S. Woinowsky-Krieger, and S. Woinowsky, *Theory of plates and shells*, vol. 2. McGraw-hill New York, 1959.

[102] J. P. Landers, *Handbook of capillary and microchip electrophoresis and associated microtechniques*. CRC press, 2007.

[103] B. Kirby, *Micro-and nanoscale fluid mechanics*, vol. 32. Cambridge University Press New York, 2010.

[104] G. Lippmann, “Epreuves réversibles. Photographies intégrales.,” *Comptes Rendus De l’Académie Des Sciences De Paris*, vol. 146, pp. 446–451, 1908.

[105] H. E. Ives, “Panoramagrams Made With a Large Diameter Lens,” *J. Opt. Soc. Am.*, vol. 20, no. 6, pp. 332–340, Jun. 1930.

[106] M. Levoy and P. Hanrahan, “Light field rendering,” in *Proceedings of the 23rd annual conference on Computer graphics and interactive techniques*, 1996, pp. 31–42.

[107] R. Ramamoorthi and P. Hanrahan, “On the relationship between radiance and irradiance: determining the illumination from images of a convex Lambertian object,” *JOSA A*, vol. 18, no. 10, pp. 2448–2459, 2001.

[108] A. Gershun, P. H. Moon, and G. Timoshenko, *The light field*. Massachusetts Institute of Technology, 1939.

[109] J. Arvo, “The irradiance Jacobian for partially occluded polyhedral sources,” in *Proceedings of the 21st annual conference on Computer graphics and interactive techniques*, 1994, pp. 343–350.

[110] M. Levoy, “Light fields and computational imaging,” *IEEE Computer*, vol. 39, no. 8, pp. 46–55, 2006.

[111] M. Levoy, R. Ng, A. Adams, M. Footer, and M. Horowitz, “Light field microscopy,” in *ACM Transactions on Graphics (TOG)*, 2006, vol. 25, pp. 924–934.

[112] R. Ng, “Digital light field photography,” Stanford University, 2006.

[113] D. Lanman, G. Wetzstein, M. Hirsch, W. Heidrich, and R. Raskar, “Polarization fields: dynamic light field display using multi-layer LCDs,” in *ACM Transactions on Graphics (TOG)*, 2011, vol. 30, p. 186.

[114] G. Wetzstein, D. Lanman, M. Hirsch, and R. Raskar, “Tensor displays: compressive light field synthesis using multilayer displays with directional backlighting,” *ACM Transactions on Graphics (TOG)*, vol. 31, no. 4, p. 80, 2012.

[115] G. Wetzstein, D. Lanman, W. Heidrich, and R. Raskar, “Layered 3D: tomographic image synthesis for attenuation-based light field and high dynamic range displays,” in *ACM Transactions on Graphics (TOG)*, 2011, vol. 30, p. 95.

[116] R. Ng and P. Hanrahan, “Digital correction of lens aberrations in light field photography,” in *Contract Proceedings 2006*, 2007, p. 63421E–63421E.

[117] M. Born and E. Wolf, *Principles of optics: electromagnetic theory of propagation, interference and diffraction of light*. CUP Archive, 1999.

[118] J. E. Greivenkamp, *Field guide to geometrical optics*, vol. 1. SPIE Press Bellingham, Washington, 2004.

[119] E. H. Adelson and J. Y. Wang, “Single lens stereo with a plenoptic camera,” *IEEE transactions on pattern analysis and machine intelligence*, vol. 14, no. 2, pp. 99–106, 1992.

[120] Lytro, INC., “Lytro website. https://www.lytro.com/. Accessed 13 February 2014.” .

[121] Raytrix GmbH, “Raytrix website, http://www.raytrix.de/. Accessed 13 February 2014.” .

[122] T. Georgiev and A. Lumsdaine, “Superresolution with plenoptic camera 2.0,” *Adobe Systems Incorporated, Tech. Rep*, 2009.

[123] T. Georgiev and C. Intwala, “Light field camera design for integral view photography,” *Adobe System, Inc., Technical Report*, 2006.

[124] Pelican Imaging, “Pelican Imaging website. http://www.pelicanimaging.com/. Accessed February 13 2014.” .

[125] A. Veeraraghavan, R. Raskar, A. Agrawal, A. Mohan, and J. Tumblin, “Dappled photography: Mask enhanced cameras for heterodyned light fields and coded aperture refocusing,” *ACM Transactions on Graphics*, vol. 26, no. 3, p. 69, 2007.

[126] K. Marwah, G. Wetzstein, Y. Bando, and R. Raskar, “Compressive light field photography using overcomplete dictionaries and optimized projections,” *ACM Transactions on Graphics (TOG)*, vol. 32, no. 4, p. 46, 2013.

[127] A. Wang, P. Gill, and A. Molnar, “Light field image sensors based on the Talbot effect,” *Applied optics*, vol. 48, no. 31, pp. 5897–5905, 2009.

[128] L. H. Ting, S. Feghhi, S. J. Han, M. L. Rodriguez, and N. J. Sniadecki, “Effect of Silanization Film Thickness in Soft Lithography of Nanoscale Features,” *Journal of Nanotechnology in Engineering and Medicine*, vol. 2, no. 4, p. 041006, 2011.

[129] Y. Gao and M. L. Kilfoil, “Accurate detection and complete tracking of large populations of features in three dimensions,” *Opt Express*, vol. 17, no. 6, pp. 4685–4704, 2009.

[130] J.-D. Chen and D. Wilkinson, “Pore-scale viscous fingering in porous media,” *Physical review letters*, vol. 55, no. 18, p. 1892, 1985.

[131] G. M. Homsy, “Viscous fingering in porous media,” *Annual Review of Fluid Mechanics*, vol. 19, no. 1, pp. 271–311, 1987.

[132] R. Pepperkok and J. Ellenberg, “High-throughput fluorescence microscopy for systems biology,” *Nature Reviews Molecular Cell Biology*, vol. 7, no. 9, pp. 690–696, 2006.

[133] P. Lang, K. Yeow, A. Nichols, and A. Scheer, “Cellular imaging in drug discovery,” *Nature Reviews Drug Discovery*, vol. 5, no. 4, pp. 343–356, 2006.

[134] Ibidi, “384-well microplate instructions, http://ibidi.com/fileadmin/products/labware/plates/P_8840X_Plate_384well/IN_884XX_384.pdf.” .

[135] D. J. Brady, M. E. Gehm, R. A. Stack, D. L. Marks, D. S. Kittle, D. R. Golish, E. M. Vera, and S. D. Feller, “Multiscale gigapixel photography,” *Nature*, vol. 486, no. 7403, pp. 386–389, 2012.

[136] O. S. Cossairt, D. Miau, and S. K. Nayar, “Gigapixel computational imaging,” in *Computational Photography (ICCP), 2011 IEEE International Conference on*, 2011, pp. 1–8.

[137] G. Zheng, X. Ou, and C. Yang, “Towards giga-pixel microscopy,” in *CLEO: Science and Innovations*, 2012.

[138] S. O. Isikman, A. Greenbaum, W. Luo, A. F. Coskun, and A. Ozcan, “Giga-pixel lensfree holographic microscopy and tomography using color image sensors,” *PloS one*, vol. 7, no. 9, p. e45044, 2012.

[139] E. Schonbrun, W. N. Ye, and K. B. Crozier, “Scanning microscopy using a short-focal-length Fresnel zone plate,” *Optics letters*, vol. 34, no. 14, pp. 2228–2230, 2009.

[140] H. J. Tiziani, R. Achi, R. N. Krämer, and L. Wiegers, “Theoretical analysis of confocal microscopy with microlenses,” *Applied optics*, vol. 35, no. 1, pp. 120–125, 1996.

[141] C. Vonesch and M. Unser, “A fast thresholded Landweber algorithm for wavelet-regularized multidimensional deconvolution,” *Image Processing, IEEE Transactions on*, vol. 17, no. 4, pp. 539–549, 2008.

[142] F. T. O’Neill and J. T. Sheridan, “Photoresist reflow method of microlens production Part II: Analytic models,” *Optik-International Journal for Light and Electron Optics*, vol. 113, no. 9, pp. 405–420, 2002.

[143] H. J. Tiziani and H.-M. Uhde, “Three-dimensional analysis by a microlens-array confocal arrangement,” *Applied Optics*, vol. 33, no. 4, pp. 567–572, 1994.

[144] T. Wilson and A. R. Carlini, “Size of the detector in confocal imaging systems,” *Optics letters*, vol. 12, no. 4, pp. 227–229, 1987.

[145] S. Preibisch, S. Saalfeld, and P. Tomancak, “Globally optimal stitching of tiled 3D microscopic image acquisitions,” *Bioinformatics*, vol. 25, no. 11, pp. 1463–1465, 2009.

[146] J. W. Lichtman, J. Livet, and J. R. Sanes, “A technicolour approach to the connectome,” *Nature Reviews Neuroscience*, vol. 9, no. 6, pp. 417–422, 2008.

[147] D. Cai, K. B. Cohen, T. Luo, J. W. Lichtman, and J. R. Sanes, “Improved tools for the Brainbow toolbox,” *Nature methods*, 2013.

[148] J. W. Goodman, *Introduction to Fourier optics*. Roberts and Company Publishers, 2005.

[149] N. Lazaros, G. C. Sirakoulis, and A. Gasteratos, “Review of stereo vision algorithms: from software to hardware,” *International Journal of Optomechatronics*, vol. 2, no. 4, pp. 435–462, 2008.

[150] S. K. Nayar and Y. Nakagawa, “Shape from focus: An effective approach for rough surfaces,” in *Robotics and Automation, 1990. Proceedings., 1990 IEEE International Conference on*, 1990, pp. 218–225.

[151] S. K. Nayar, “Shape from focus system,” in *Computer Vision and Pattern Recognition, 1992. Proceedings CVPR’92., 1992 IEEE Computer Society Conference on*, 1992, pp. 302–308.

[152] S. K. Nayar and Y. Nakagawa, “Shape from focus,” *Pattern analysis and machine intelligence, IEEE Transactions on*, vol. 16, no. 8, pp. 824–831, 1994.

[153] R. Ng, “Fourier slice photography,” in *ACM Transactions on Graphics (TOG)*, 2005, vol. 24, pp. 735–744.

[154] M. Noguchi and S. K. Nayar, “Microscopic shape from focus using active illumination,” in *Pattern Recognition, 1994. Vol. 1-Conference A: Computer Vision & Image Processing., Proceedings of the 12th IAPR International Conference on*, 1994, vol. 1, pp. 147–152.

[155] D. Scharstein and R. Szeliski, “High-accuracy stereo depth maps using structured light,” in *Computer Vision and Pattern Recognition, 2003. Proceedings. 2003 IEEE Computer Society Conference on*, 2003, vol. 1, pp. I–195.

[156] F. A. Jenkins and H. E. White, “Fundamentals of optics,” *New York: McGraw-Hill, 1957, 3rd ed.*, vol. 1, 1957.

[157] L. Waller, L. Tian, and G. Barbastathis, “Transport of Intensity phase-amplitude imaging with higher order intensity derivatives,” *Optics express*, vol. 18, no. 12, pp. 12552–12561, 2010.

[158] J. W. Nadler, D. E. Angelaki, and G. C. DeAngelis, “A neural representation of depth from motion parallax in macaque visual cortex,” *Nature*, vol. 452, no. 7187, pp. 642–645, Apr. 2008.

[159] D. Paganin, A. Barty, P. J. McMahon, and K. A. Nugent, “Quantitative phase-amplitude microscopy. III. The effects of noise,” *Journal of microscopy*, vol. 214, no. 1, pp. 51–61, 2004.

[160] L. Waller, S. S. Kou, C. J. Sheppard, and G. Barbastathis, “Phase from chromatic aberrations,” *Optics express*, vol. 18, no. 22, pp. 22817–22825, 2010.

[161] C. Zuo, Q. Chen, Y. Yu, and A. Asundi, “Transport-of-intensity phase imaging using Savitzky-Golay differentiation filter-theory and applications,” *Optics express*, vol. 21, no. 5, pp. 5346–5362, 2013.

[162] D. Fattal, Z. Peng, T. Tran, S. Vo, M. Fiorentino, J. Brug, and R. G. Beausoleil, “A multi-directional backlight for a wide-angle, glasses-free three-dimensional display,” *Nature*, vol. 495, no. 7441, pp. 348–351, 2013.

[163] *Seeing depth through a single lens | Harvard School of Engineering and Applied Sciences. URL: http://www.youtube.com/watch?v=Zn4ov_W4_l0&feature=youtube_gdata_player.* 2013.

Appendix A. List of Movies

Table A: List of movies included in this dissertation.

Filename	Movie ID	Movie Caption	Associated Figure
Movie2_1.MOV	Movie 2-1	Movie of the pressure dynamics in a dual-phase (air/water) flow inside a microfluidic Hele-Shaw cell. Left side shows the raw microscope movie. Right side shows extracted pressure map. Color bar relates pressure to color in the pressure map. Units are PSI.	Figure 2-6
Movie3_1.MOV	Movie 3-1	Perspective views of a pile of fluorescent beads (2 μm and 5 μm nominal diameter). The viewpoint is rotating at 12° from the optical axis.	Figure 3-7c
Movie3_2.MOV	Movie 3-2	Movie showing a zoom-in from the full-field view to the full resolution of an image of a mouse kidney slice.	Figure 3-19
Movie4_1.MPG	Movie 4-1	Two input LMI images followed by a perspective shifting animation of a bent piece of paper along the horizontal direction. Imaged with an f/1.4 SLR lens.	Figure 4-1b
Movie4_2.MPG	Movie 4-2	Two input LMI images followed by a perspective shifting animation of a curled tissue microarray core. Imaged with a 10×, 0.3NA objective on an Olympus brightfield microscope in transmission mode.	Figure 4-2a
Movie4_3.MPG	Movie 4-3	Two input LMI images followed by a perspective shifting animation of the head of a wood tick. Imaged with a 10×, 0.3NA objective on an Olympus brightfield microscope in transmission mode. Significant complex translucent structure is apparent.	Figure 4-2b
Movie4_4.MPG	Movie 4-4	Two input LMI images followed by a perspective shifting animation of a pile of 5 μm fluorescent beads. Imaged with a 50×, 0.55NA microscope objective.	Figure 4-2d

Appendix B. List of Abbreviations

Table B: List of common abbreviations in this disseration.

Abbreviation	Meaning
H&E	Hematoxylin & Eosin
FOV(s)	Field(s)-of-view
fps	Frames per second
Gpx	Gigapixel
HCS	High content screening
LED	Light emitting diode
LMI	Light field moment imaging
Mpx	Megapixel
MTF	Modulation transfer function
ms	milliseconds
NA	Numerical aperture
NOA 61	Norland optical adhesive 61
PDMS	Polydimethylsiloxane
PSF	Point spread function
PSI	Pounds per square inch
px	Pixel
RBC	Red blood cell
SNR	Signal-to-noise ratio
UV	Ultraviolet